Fracture Mode Analysis, Geomechanics, Petrophysics and Fracture Characterization

An Experimental Investigation on Whitby Shales and Various Other Rock Types

Master's Thesis, 18 August 2015

Mutia Ifada Wahyu Primarini

<<Page left blank intentionally>>

Fracture Mode Analysis, Geomechanics, Petrophysics, and Fracture Characterization: An Experimental Investigation on Whitby Shales and Various Other Rock Types

THESIS

Submitted in the partial fulfillment of
The requirements for the degree of

MASTER OF SCIENCE

in

PETROLEUM ENGINEERING AND GEOSCIENCES

by

Mutia Ifada Wahyu Primarini
Born in Jogjakarta, Indonesia

Supervisor:	Dr. A. Barnhoorn,	Applied Geophysics & Petrophysics, TU Delft
Thesis Committee:	Prof. Dr. P.L.J. Zitha,	Petroleum Engineering, TU Delft
	Prof. Dr. G. Bertotti,	Applied Geology, TU Delft

An electronic version of this thesis is available at http://repository.tudelft.nl

Track Petroleum Engineering
Department of Petroleum Engineering and Geosciences
Faculty Civil Engineering and Geosciences, Delft University of Technology
Delft, the Netherlands

© 2015 Mutia Ifada Wahyu Primarini

Fracture Mode Analysis, Geomechanics, Petrophysics, and Fracture Characterization: An Experimental Investigation on Whitby Shales and Various Other Rock Types

Author: Mutia Ifada Wahyu Primarini
Student ID: 4318250
Email: MutiaIfadaWahyuPrimarini@student.tudelft.nl

Abstract

The rapidly decreasing reserves of conventional gas has forced oil and gas industries to conduct more exploration on unconventional resources, like shale gas. To produce gas from shales in economically viable manner, stimulation techniques like hydraulic fracturing are required. One important factor for a successful hydraulic fracturing is knowing the fracture characteristics such as the fracture mode occurrence. Unfortunately, the factors controlling the fracture mode occurrence are not known yet. This study tries to find out the factors controlling the fracture mode occurrence by investigating the relation between fracture angle, confining pressure, and several rock properties. The fracture mode analysis being developed in this study suggests that for low strength rock like Bad Bentheim sandstone (46.65 MPa) and Indiana limestone (36.5 MPa), fracture modes are not dependent to the confining pressure. Fractures are already at mode II at zero confining pressure, while stronger rocks like Belgium limestone and Granite (125 and 128 MPa respectively) show fracture mode I at zero confining pressure. The experiments convey that the strength of the rock, which is related to its porosity, is the dominant factor controlling the occurrence of fracture mode I and mode II. This study also evaluates the prospectivity of the Whitby mudstone formation in the United Kingdom, which is a depositionally- and time-equivalent shale to the Posidonia Shale Formation (PSF). The PSF is one of the potential resource rocks for shale gas exploration in the Netherlands. Brittleness indices and fraccability indices of WMF from various methods are also determined and analyzed in this study. The results of WMF characterization show that WMF has high heterogeneity, which could imply that it is less favorable for hydraulic fracturing. Comparing the results of WMF to other producing gas shale shows that the WMF has a low range in: porosity, Young's modulus, and quartz content, and high range in: laminations, and clay contents, suggesting that WMF is less potential for the shale gas resource. However, based on its characteristics, if WMF is divided into four zones, our experiments show that several zones (top and bottom part of WMF) can be considered as the most favorable ones for hydraulic fracturing in the WMF formation.

Keywords: Whitby Mudstone Formation, Fraccability index, Brittlenes index, Hydraulic fracturing, Fracture mode, Fracture Angle

Supervisor:	Dr. A. Barnhoorn,	Applied Geophysics & Petrophysics, TU Delft
Thesis Committee:	Prof. Dr. P.L.J. Zitha,	Petroleum Engineering, TU Delft
	Prof. Dr. G. Bertotti,	Applied Geology, TU Delft

Acknowledgements

First of all, I would like to thank the Indonesia Endowment Fund for Education (LPDP) who support my study at TU Delft University. Then, I really want to take this chance to give a sincere thanks to my supervisor Dr. Auke Barnhoorn whom I think is very helpful, patience, and supportive when giving a guidance and suggestions to my work. I would like to thank Prof. Giovanni Bertotti for the discussion and the direction of the topic of my thesis, and to Prof. Dr. P.L.J. Zitha, the Chair Assessments Committee, for his support. I would also like to express my gratitude for all the assistances provided by the Geoscience and Engineering lab technicians: Wim Verwaal, Arno Mulder, Dirk Delforterie, Joost van Meel, Guus Lohlefink. The support from Dr. K.H.A.A. Wolf during the utilizing the Mincomp BASICA Software is very appreciated. I am thankful to my fellow Msc. Student Jeroen Verheij, who works under the same supervisor, for the support and discussion about our works.

Furthermore I would also like to thank all of my friends and family, especially my parents and my husband. I could not have finish my study without your love and support.

All Praise and Thanks to the Almighty and All Caring for His Guidance.

Table of Contents

List of Figures

List of Tables

1. Introduction

1.1 Background/Motivation

The needs of energy, especially oil and gas, increase while the supplies are decreasing. In the Netherlands, where 85% of the gas fields are produced with the conventional technology (Energie Beheer Nederland B.V, 2014), EBN's data in 2014 showed that with its current production rate, the country could only be self-sufficient until 2025 (Figure 1). This makes increasing the recovery factor from the unconventional gas reservoir like shale[1], very important.

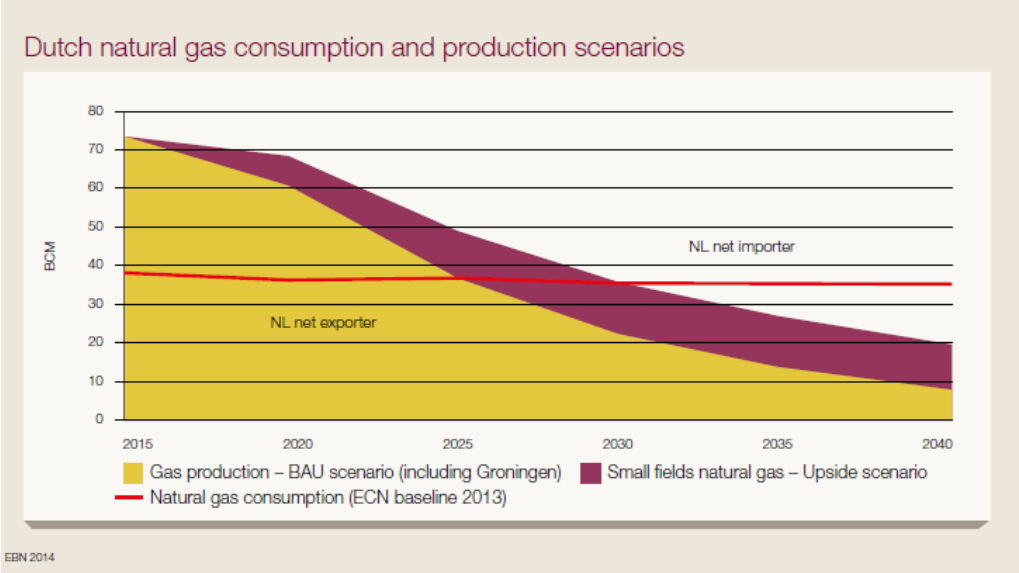

Figure 1 Natural gas consumption and production in Netherland (EBN, 2014)

To increase the well production and improve the recovery factor in unconventional (tight) gas reservoir, a stimulation technique, like hydraulic fracturing is required (E.King, 2010; Ren, et al., 2014). To design a hydraulic fracturing job, it is important to understand the reservoir properties (Pyrak-Nolte, 1987). Those include the geomechanical properties such as Young's modulus and Poisson's ratio, and their relations with the fracture characteristic, as they will dictate the requirements of the horsepower and the material to be pumped downhole. Anisotropy also plays an important role in the fracture network and geometry. (Zhubayev & Barnhoorn, 2013) stated that models which neglect the shale anisotropy may fail to predict the behavior of hydraulic fracturing.

The discussion about shale gas is very active in the Netherlands, but little is actually known about the occurrence of shale gas / shale oil in the Dutch subsurface (Lie-A-Fat, 2014). Most of the studies have

[1] Shale is used to describe a wide variety of rocks that are composed of much fined grained-material (< 4 µm diameter), but may also contains variable amounts of silt-size particles (up to 62.5 µm diameter) (Passey, et al., 2010).

been performed in North America, with abundant data of Barnett-, Eagleford-, and Heynesville-shale[2], but less data could be found about shale in the Netherlands (Schavemaker, 2013). In the Netherlands, there are two intervals that have been considered as potential formations for shale gas exploration; the Lower Jurassic PSF (Posidonia Shale Formation) which is the shallowest horizon, and the deeper Upper Carbonifereous (Namurian) Greverik Formation. Figure 2 shows the map of the PSF occurrence and its associated depth.

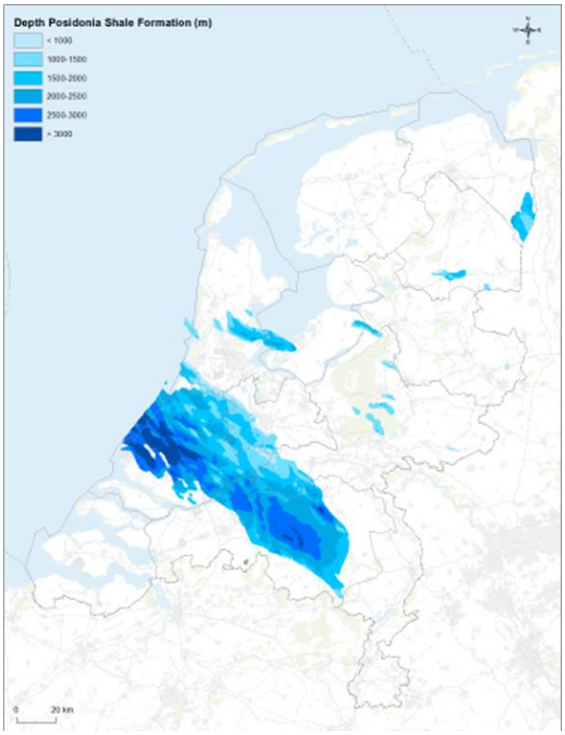

Figure 2. The PSF in the Netherlands with its associated depth (Zijp, et al., 2013)

PSF is known as the main source rock for oil in the Netherlands, with 30-50 thickness, and also acts as oil source rock in Germany (Wong, 2007). Research on the PSF showed that a number of areas are expected to have reached gas maturity and those area appear to be a potential for shale oil as well (Schavemaker, 2013). Unfortunately the studies conducted on the PSF are still rare. The Posidonia shale is not outcropping yet (Lie-A-Fat, 2014), while the cores available are very rare. In total, nine wells core the PSF but only 5 are usable (Zijp, et al., 2013), and those cores are not available for this research.

Due to the scarcity of the PSF cores/sample, Whitby Mudstone Formation (WMF) shales, an environmentally and depositional analog of PSF is chosen for this study to characterize and analyze its prospectively and point out the possible behavior of hydraulic fracturing or future gas exploration in the Netherlands.

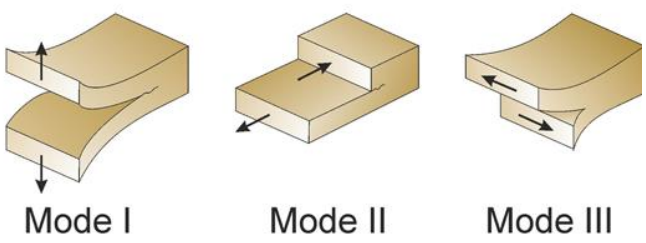

Due to its low porosity and low permeability, in unconventional gas reservoir, the presence of fractures either natural or hydraulically induced always becomes a prerequisites for a sufficient

hydrocarbon flow. The fractures will create additional permeability and networks to free the gas for collection. Two basic types of brittle fractures are commonly observed in rocks: mode I[3] (opening fractures) and mode II[4] (shear fractures) (Ramsey & Checter, 2004) as illustrates in Figure 3.

In hydraulic fracturing, fracture mode I is preferable for conductivity (as long as the stress is in the right direction). In a horizontal well, it is desirable to drill the well perpendicular to the direction of the original compression to keep the fracture opens (please see Figure 4 for the illustration). This shows the importance of understanding the fracture mode occurrence in the reservoir.

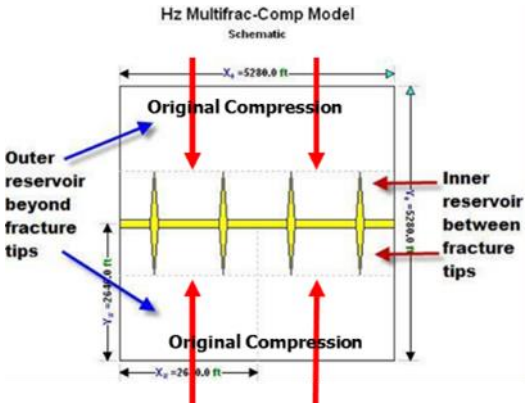

Figure 4 Illustration of horizontal well with its fracture opening and the direction of original compression, (http://www.fekete.com)

(Bertotti, et al., 2015, under review) stated that fracture mode I and mode II; (1) would be formed in different orientations with respect to the principal stresses; (2) form networks with different topology and intersections; (3) have different aperture distributions; (4) display different apertures response to changes in states of stress occurring during the history of the rocks. Thus, understanding and being able to predict the occurrence of a fracture mode are important, will give a hint of fracture-related permeability and how these fracture-related permeability change when stress conditions are modified.

Presumably some fractures are in the transition mode between mode I and mode II as described by (Hancock, 1985). However, the factors that are controlling the occurrence of the fracture and the transition stage between them are not known yet. In general, the continuous transition between mode I and mode II fractures is predicted based on the empirical Mohr-Coulomb (MC) envelope. The MC envelope (even when it is integrated with Griffith theory) states that mode I fractures could only occur when σ_3 is negative (tensional). The same condition is applicable for stress condition marking the transition between mode I and mode II.

[3] Mode I/ extension fracture is a separation of a body across a surface normal to the direction of least principal stress (Grigs & Handin, 1960)

[4] Mode II/ shear fracture is refer to a fracture with a plane of 20°- 40° angle to the maximum principal stress direction. (Engelder, 1999)

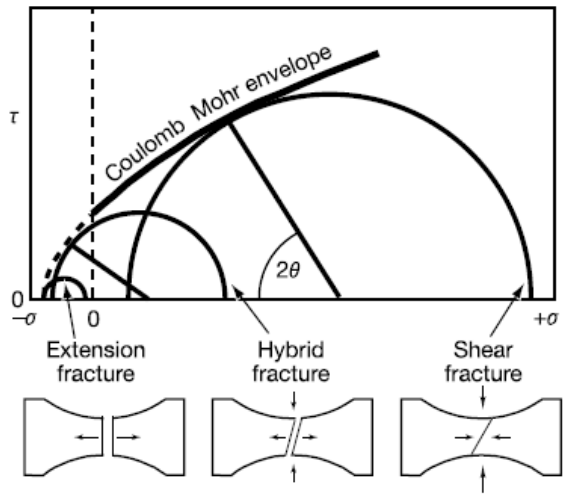

Figure 5. Different type of fracturing are related to confining pressure (Ramsey & Checter, 2004).

Figure 5 shows that mode I fracture (extension), and transition (hybrid) fracture between mode I and II are occurred when σ_3 is negative. The problems arise because the tension is practically non-existent in the earth (Bertotti, 2014). (Secor, 1965) argued that a negative σ_3 could be obtained by having a higher-than-normal fluid pressure. However experiments done by (Handin & Hager, 1957; Grigs & Handin, 1960; Jorand, et al., 2012; Handin, et al., 1963) and some other experiments suggests that the results did not correspond with the MC criterion.

Until the end of the last century, documentations about mode I – mode II transition, and the correlated conditions admitting the occurrence of hybrid fracture were lacking (Bertotti, et al., 2015, under review). Researchers have done a lot of work to constrain the strength of rocks, the "brittle – ductile" transition, et cetera (Handing & John, 1960; Handin & Hager, 1957; Handin & Hager, 1958; Handing & John, 1960; Rao, et al., 2003). But very little attention has been dedicated to changes in the angle of fractures with respect to the σ_1.

It is clear that fracture mode occurrence is very important for the success of hydraulic fracturing, but the factors controlling the occurrence are not known yet. The investigations of the fracture transition mode related to changes of fracture angle are limited, while the information is important to better understand the factors directing the occurrence of fracture mode I and II.

Based on the explanations before, this research is carried out to investigate the characteristics of WMF shale, to determine its prospectively, and to analyze which horizons will be the most promising zone for hydraulic fracturing and further development for future gas exploration in the Netherlands. Related to the fracture mode, this research will examine the factors controlling the fracture's mode, in correspondence with the changes of fracture angle, related to the rock properties and the confining pressure.

1.2 Theoretical Background

This section will talk about the theory and previous research related to the topic of this thesis. It will be divided into two subsections: (i) Research on the MWF and shales in general, and (ii) Fracture mode analysis.

1.2.1 Research on the WMF and Shales in General

This part is about related works or previous researches related to the fracture and characterization of the WMF shale. It will be divided into two parts: (i) Research on the MWF, explaining the previous works related to the WMF, and (ii) Research on the shale geomechanics and fracture analysis in general, describing the previous works in correspondence with the Brittleness index and Fraccability index.

Research on the WMF

As previously mentioned in 1.1, PSF has been considered as the potential new resource for oil and gas in the Netherlands. According to TNO, 30 wells have been logged in PSF, but only 5 cores are usable (Zijp, et al., 2013). Because of the scarcity and the widely spaced subsurface data (Zijp, et al., 2014), researchers started to use the WMF to learn more about PSF. Research about WMF can be categorized into its: (i) characteristics, (ii) anisotropy, and (iii) the insight of the productivity and fraccability of the shale. (Zijp, et al., 2014) did a research which included a mineralogy analysis, fracture analysis (identification, and the density), and spectral Gamma Ray analysis. The aim was to elaborate the fraccability and productivity of the shale. The experiments were done by running a Gamma Ray (GR) log through a WMF outcrop and compare them with logs from the Dutch subsurface. The fracture characterization was done by taking some pictures on the outcrop and analyzing the fracture in the subsurface, and the fraccability analysis was done by looking at the mineralogy from GR and fracture characterization. But these experiments did not include the geomechanical analysis. No elastic modulus was taken into account in the analysis. Their result was a zonation in term of the geochemical behavior, which relates the preferable zone (high density of fracture) with the mineral content of the zone. (Ravenstein, 2014) did experiments in the Whitby Mudstone Formation (WMF), which incorporated the geomechanical properties and the fracture characteristics by taking 5 samples points in the formation. He integrated the use of micro CT-scanner to analyze the fractures. The aim of his thesis was to define the fraccability of WMF. In his thesis, the Fraccability Index (FI) was obtained from the Brittleness Index (BI) and Toughness. (Zhubayev & Barnhoorn, 2013) conducted research on geomechanical and petrophysical properties, such as porosity, Young's modulus, and Poisson's ratio. They also measured the anisotropy, focused on the quantification of elastic anisotropy and seismic attenuation anisotropy. (Lie-A-Fat, 2014) did some experiments on the WMF shales focusing in the anisotropy. She also documented microstructural and petrophysical data of the WMF, such as density, porosity, and the mineralogy analysis.

From above descriptions, we can say that there are pretty much information about the WMF shale, but only one research made the use of micro CT-scanner to characterize the fracture. Furthermore, all those researches used different samples for different experiments, which made it difficult to correlate one result to another in drawing an elaborate conclusion.

Research on the Shale Geomechanics and Fracture Analysis in General

According to (Altamar & Marfurt, 2014), rock is classified into ductile and brittle based on its behavior when subjected to increasing stress. Three successive stages of deformation (elastic, ductile, and fracture) are encountered, and the rock is considered to be brittle when it has a larger region of elastic behavior but only smaller region of ductile behavior. In contrast, if a material has a smaller region of plastic behavior and larger region of ductile behavior, absorbing much energy before failure, it is considered as ductile (Holt, et al., 2011). Brittleness has been widely considered as a key parameter to evaluate the potential of hydraulic fracturing initiation and propagation in low permeability rock, like shale (Yang, et al., 2013; Holt, et al., 2011). This thesis will use some methods to calculate BI as defined by (Yang, et al., 2013). Some BI that are widely used to characterize shale are the Brittleness Index from the Mineralogy content (Jarvie, et al., 2007; Wang & Gale, 2009), BI with the approach from the Elastic Modulus E and v (Rickman, et al., 2008; Waters, et al., 2011), and BI from the elastic and total strain (Coates & Parsons, 1966).

(Jin, et al., 2014) did an evaluation of the fraccability Index (FI) in shale reservoirs. In his study, he integrated the petrophysical and geomechanical approaches to come out with several options of defining FI. His approach related the fracture toughness, Young's modulus, and strain energy release (G_C) with Brittleness Index.

There are areas that can be developed from the previous experiments in the WMF to obtain a better conclusion. For example, (1) adding more data points to get a wider coverage and better overview/ conclusion of the WMF characteristic, (2) using the same sample from the same section throughout different experiments to reduce the uncertainty and to get the more representative data from each section height, and (3) integrate one result with another to get some more insights on the correlation between each result.

In this thesis, a series of fracturing experiments has been e done on shale and other types of rocks to understand the correlation between the geomechanical and fracture characteristics. To get a better visualization of the fracture networks and its connectivity, the use of a micro CT-scanner for 3-D imaging will be applied.

By using micro CT-scanner, the interior of the rock sample including the fracture, can be visualized in a great detail up to 0.5 µm in resolution. Other advantages is, that the scanner will not destruct the sample, leaving the sample completely intact. However, due to the beam hardening phenomenon, the scan can display relics, eg. The longer X-ray paths become darker and the shorter X-ray paths become brighter (Ketcham & Hanna, 2014). This phenomenon can be corrected by cutting the edge of the sample. Another weakness is selecting the threshold process with a certain value, which can be tricky, because it has to be done for each slice and tedious (Nakashima, et al., 2010).

1.2.2 Fracture Mode Analysis

As described before there is inconsistency between two lines of investigations (MC criterion and the experimental results) about the fracture transition mode. There is limited documentation about the conditions allowing the formation of fracture mode I – mode II, and the transition between them. Most of the work done is related to rock strength and "brittle – ductile" transition, and very few related to the fracture angle (Bertotti, 2014). Currently, the understanding of transitional – tensile fracture propagation is based on the empirical Mohr – Coulomb (MC) envelope (Engelder, 1999). (Fossen, 2010) stated in his book that each rock has its own Mohr- envelope, and it does not always obey the MC criterion.

The experiments conducted by (Brace, 1964), showed that the parabolic MC failure envelope failed to predict the fracture angle for a sample that failed under compression. Since then, a lot of researchers have been questioning the validity of MC criterion and have been doing some investigation to confirm it, such as (Ziony, 1966) who observed Permian sandstone beds over Comb Ridge, and (Muller & Pollard, 1977) who observed the fractures in Colorado rocks. Both of them found out that many "conjugate" joint sets (hybrid fracture) have cross cut at a bigger angle than predicted by MC-criterion.

(Handin & Hager, 1957) did experiments in various sedimentary rocks under confining pressure, and the result showed that the strength of the rock is increasing with increasing the confining pressure. There was a remark that most of the fractures were shear fractures (fracture mode II), but there was no documentation on the fracture angle, which made it difficult to distinguish exactly the occurrence between fracture mode I and mode II. (Grigs & Handin, 1960) also did experiments in dolomite, quartz, and limestone with confining pressure, and his results showed that fracture mode I (extension) occurs when: (i) σ_3 is negative (tensional); (ii) $\sigma_3 = 0$ (zero); (iii) σ_3 = slightly positive. This results did not align with the MC criterion even when it is combined with the Griffith and Von Misses criterion. More recently, (Myrvang, 2001) did experiments in coal, and found out that the envelope of his data result is diverging from the linear trend defined by the MC criterion.

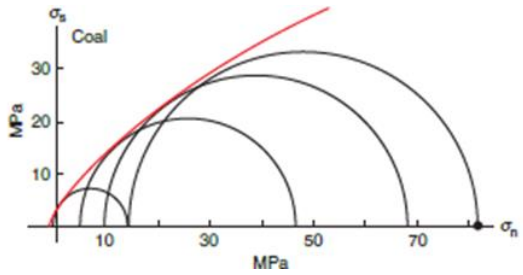

Figure 6 The Mohr envelope for coal, based on triaxial test. When the confining pressure is increased, the strength of the rock is increases, and new circle can be drawn in the figure. Note that the envelope diverges from the linear trend defined by the Coulomb Criterion (Myrvang, 2001).

Figure 6 depicts that start from 0 confining pressure, the fracture is already in mode 2, not obeying the coulomb criterion. It is aligned with the statement from (Secor, 1965) that the MC criterion is unable to predict correctly the occurrence of extensional fractures (fracture mode 1) oriented parallel to the maximum compressional stress, as it requires tension which is extremely rare in the Earth.

(Jorand, et al., 2012) did a test in some samples made of synthetic granular, cohesive, frictional and dilatant rock analogue material (GRAM2). He applied confining pressure in his test, and his results showed that fracture mode I could form at negative σ_3 and even at slightly compressive σ_3. He also mentioned that when the confining pressure exceeds a certain value the fracture becomes oblique with respect to σ_1, and this obliquity increases with confining pressure. (Ramsey & Checter, 2004) experimented with the Lorano Bianco Carrara Italian marble and made a good documentation for the fracture angle changing with the increasing confining pressure. He found out that the fracture continuously transforms from mode I and mode II, with transition mode in between, as the confining pressure increases. But his results deviated from the MC-Griffith criterion.

Except for the (Ramsey & Checter, 2004), we have not found any experiments done before carried out a good documentation of the fracture angle, nor relate the fracture angle to the rock properties itself (geomechanical and petrophysical properties). From (Revenstein, 2014) data, it could be seen that fracture mode I mostly occurred in the unconfined pressure test, and that the higher the young's modulus, the fracture orientation seemed to be more vertical. Engelder (1999) did a comprehensive analysis on the transitional – tensile fracture propagation and concluded that the score card on validating transitional tensile fracture propagation in an isotropic, homogeneous rock is discouraging. Thus, there are still unanswered questions on what are the factors controlling the occurrence of fracture mode I or II.

1.3 Research Questions

Based on the background and information described before, the scientific questions for this thesis will be as follow:

1. Could the factors that control the occurrence of fracture mode I and mode 2 be determined based on the geomechanical, petrophysical, and fracture analysis? And if so, what are the dominant factors?
2. What are the characteristics of the WMF that can be obtained from the geomechanical, and acoustic experiments, microstructural, petrophysical, and micro-CT fracture analysis?
3. Could the empirically determined characteristics of WMF be used to evaluate the potential for future gas exploration in PSF, and what are the most potential horizons within the WMF?

1.4 Scope of the Thesis

This section describes the scope and limit of this thesis. Including the samples' origin and the summary of the process and analysis that will be conducted, completed with the assumption and limitation.

Fracture and Characterization of WMF Shale

Different from the rest of the rock samples where the height of the origin are not known, the WMF samples are collected from the Whitby outcrop, UK, with the sample number correspondence to the height as per stratigraphy in Figure 7.

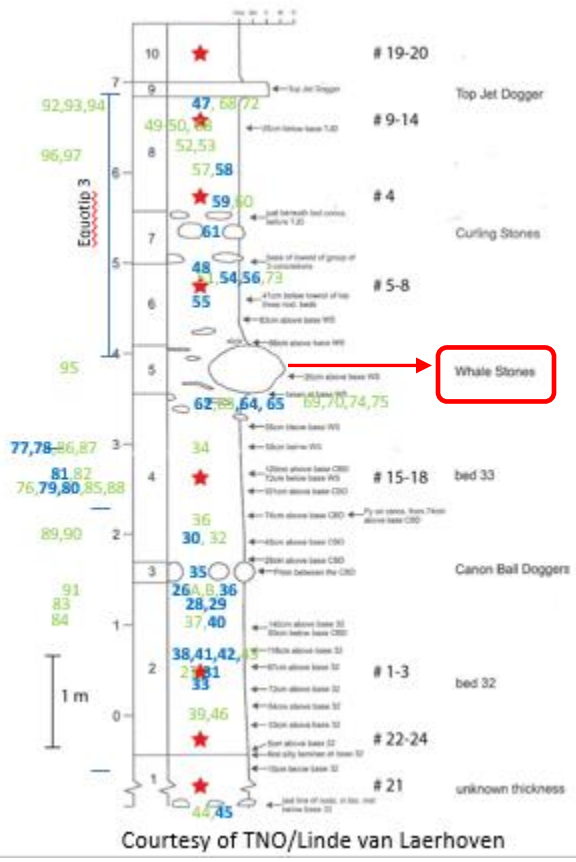

Figure 7 WMF shale samples position in Stratigraphy. (modified from Sjoukje de Vries (2014)

Figure 7 depicts the stratigraphy of WMF section with sample number related to the section height. These samples were collected last year from Whitby outcrop in UK, as part of Tough Gas Project[5]. The Whale Stones (oval shape just below 4 m height) will be used as a reference in this thesis to characterize the WMF shales.

Apart from petrophysical, and geomechanical analysis as described before, the WMF shale samples will also be subjected to microstructural analysis and acoustic measurements. Microstructural analysis will be done by conducting XRF analysis to determine the mineralogy, and its variation within the WMF section. From the mineralogy composition, a brittleness index will also be calculated based on the theory from (Jarvie, et al., 2007). Acoustic measurements will be conducted to calculate the compression (P-wave) and shear (S-wave) velocity. These measurements will be done in two directions (normal and parallel to the sample/normal and parallel to the bedding plane) to determine the anisotropy measurements, which are calculated based on (Johnston & Christensen, 1995). Based on the velocities and density results, the dynamic static moduli (Young's modulus, E, and Poisson's ratio, v) will be generated.

To determine the most promising horizons within WMF, a series of Fraccability Index (FI) will be obtained based on the paper by (Jin, et al., 2014), with combination of Brittleness Index as defined by (Jarvie, et al., 2007; Coates & Parsons, 1966; Jin, et al., 2014), Fracture toughness (K_{IC}) of the WMF section will be calculated using rearrange formula from (Olson, 2003). This value of K_{IC} is required to calculate the FI.

This thesis will use the same sample number, which corresponds to specific height of the Whitby section, to be carried out from one experiments to another. This way, the results will be more consistent to represent specific height section to be able to characterize the WMF correctly and to cover wider area than the previous research.

Fracture Mode Analysis

Eight different lithologies with different characteristics, namely Bad Bentheim Sandstone, Indiana Limestone, Granite, Belgium limestone, CAV, DEV, FAM, and WMF shale would be used in this

[5] WMF samples were collected by Auke Barnhoorn, T. Ravenstein, J.Lie-A-Fat in 2014.

experiment. CAV, DEC, FAM are also limestone from Belgium which comes from different origin. The research will include petrophysical, geomechanical, and fracture analysis.

The petrophysical analysis consists of porosity and matrix density measurements and the geomechanical analysis consists of unconfined (UCP) and confined (CP) pressure tests. Confined pressure test will be conducted to Bad Bentheimer sandstone and Indiana limestone, while the UCP will be conducted to all 8 lithologies. From the experiment results, static geomechanical properties, i.e. Young's modulus, Poisson's ratio, and ultimate strength will be determined. Based on the results from UCP experiments, the Brittleness Index will be determined according to (Coates & Parsons, 1966). For fracture analysis, the fracture created after the deformation test will be observed and the fracture angle will be recorded. In all cases we address situations where pore pressures are zero or less than hydrostatic (Bertotti, et al., 2015, under review). All the results from these experiments will be analyzed to investigate the factors that control the occurrence of fracture mode I and II.

2 Methodological Approach

To investigate the stress condition that create mode 1, mode 2, and transition fracture between them, and also the effect of rock properties to the fracture angle, some experiments and analysis are conducted to several rocks (granite, Indiana limestone, Belgium limestone, Bad Bentheim sandstone, WMF shale). Furthermore, to elaborate its geomechanics, petrophysics, and fracture characteristics, the WMF shale samples are exposed to more experiments and analyses compared to the other rock types. This chapter will explain further about the sample preparation, measurements and analysis conducted in this thesis. The order and its correlation with the purpose of this research can be seen at Table 1.

Steps/Methodology	Fracture mode Analysis in General	WMF Shale Characterization
Sample Preparation	√	√
Matrix density and porosity measurements	√	√
Unconfined Pressure experiments and Static Elastic Moduli calculation	√	√
Confined Pressure experiments	√	N/A
Fracture Characterization	√	√
Velocity, seismic anisotropy measurement, and Dynamic elastic moduli calculation	N/A	√
XRF analysis	N/A	√
Fraccability - Britteness Index determination	√	√

Table 1 The order and relation of the experiments with thesis research.

2.1. Sample Preparation

Sample preparation is very crucial for the measurements and analysis followed because it will dictates whether the experiments can be done correctly or not. A coring technique was used to prepare the limestone, granite, and sandstone, while for shale sawing and polishing techniques were done manually because the WMF shale are so fragile and behave like clay. To mimic the subsurface conditions in the nature, all samples are prepared with the bedding horizontal (normal to the cylindrical axis of the sample). The geometry recommendation from (Hawkes & Mellor, 1970) that is about 2.5 (the ratio between length and diameter) were meant to be used for the deformation experiments, however due to the apparatus limitation, all samples but shale have geometries of 4 cm diameter and 8 cm height (see the example in Figure 8).

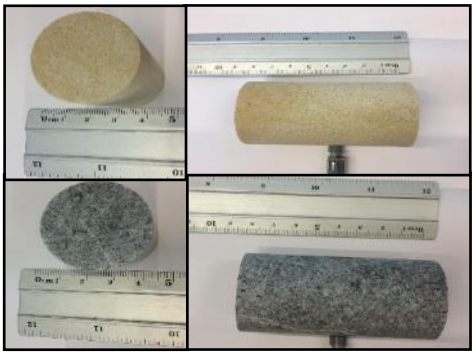

Figure 8. Example of Bed bentheim sample (top), and Granite (bottom)

Obstacle during sample preparation

Preparing the shale sample was very tedious and time consuming job (Lie-A-Fat, 2014; Ravenstein, 2014). There were few times when the sample was about to be ready but then break in the finishing process, or even in the cutting process. It were mostly due to the natural fractures occurrence and its fragile behavior. (Zhubayev, et al., 2014) mentioned about the fragility and water phobic nature of the shale in their paper. At the end, the geometry of the shale sample varied in height and diameter. Height = 23.0 – 56.7 mm and diameter = 25.7 – 42.0 mm.

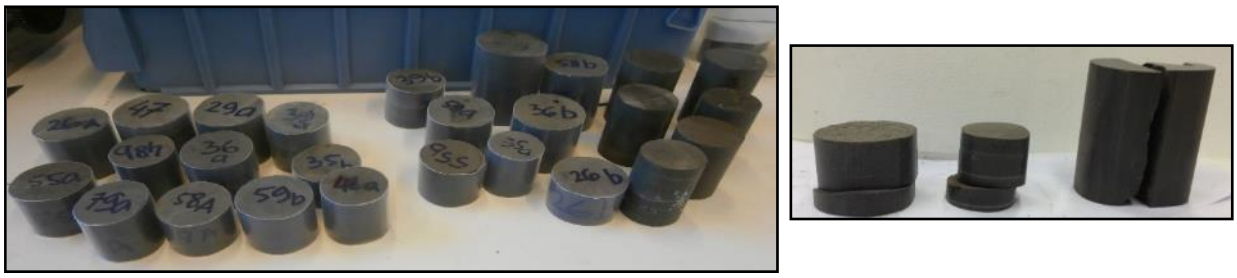

Figure 9. Shale samples ready for measurements (left), and example of broken samples (right)

2.2. Matrix density and Porosity Measurements

Dry porosity is deducted from the measurements of matrix volume using pycnometer[6]. The gas expansion Ultrapycnometer 1000 version 2.12, as illustrated in Figure 10, was used for this experiment. The sample was placed inside the cell, and helium gas was used in this experiments. Helium gas was used since the atomic dimension assure penetration into crevices and pores approaching one Angstrom (10^{-10} m) (Manual Pycnometer version 2014), thus it would increase the porosity measurements. By knowing the matrix Volume (V_m) and the mass of matrix (M_m), the matrix density (ρ_m) can be calculated using Equation 1.

$$\rho_m = \frac{Mm}{Vm} \qquad (1)$$

[6] Apparatus used to measure the matrix density and matrix volume of cylinder and powdered sample

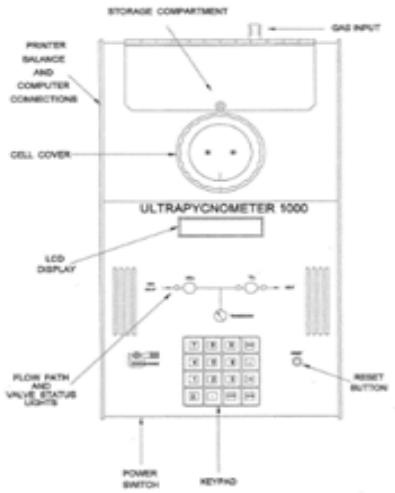

Figure 10. Ultrapicnometer used in this experiments

The output from pycnometer apparatus are matrix density and matrix volume. By knowing the matrix volume, we can calculate the porosity (Ø) using Equation 2, provided the diameter and the height of the sample in order to calculate the bulk Volume (V_b).

$$Ø = \frac{Vb - Vm}{Vb} \qquad (2)$$

The measurements of height and diameter were done 10 times for each sample to increase the accuracy. Samples prepared using drilling technique have higher accuracy in sphericity, compared to the shale samples which polished manually to shape it as a cylinder. Thus the bulk volume calculated assuming that the shale sample is a perfect cylinder might be slightly deviated from the "true" total volume of the sample.

(Lie-A-Fat, 2014) and (Ravenstein, 2014), used micro CT-scanner to obtain the bulk volume, and find s deviation of ±1% from the bulk volume calculated manually, however due to beam hardening this process turned out not to be totally accurate, therefore this process was not applied in this thesis. The measurements for the granite, limestone, and sandstone were done using different samples with the one that would undergo the deformation test, but still came from the same block. This is due to the limitation of sample size that is different between the pressure bench and the pycnometer, while for the shale samples this process was done on the same set of samples.

2.3. Unconfined Pressure Experiments and Static Elastic Moduli

The unconfined pressure experiments were done to get the static elastic properties of the rocks samples. It is done by placing the sample in a pressure bench and expose it to axial forces. A displacement control was applied to the pressure bench and it worked by pumping hot oil under the bottom plate and lifting it upwards, while applying some forces to the sample. To measure the vertical displacement, two Linear Variable Differential Transformers (LVDT) were attached along the direction of the sample, and to measure the changing in horizontal direction, a chain (extensometer) was tied around the sample. It will record the changes in diameter (see Figure 12 for the experiments' set-up).

All samples were deformed until they reached the ultimate strength or failure, which was marked by a decrease in the stress (see Figure 11 for example of stress – strain plot). To calculate the vertical strain the following equation is used:

$$\varepsilon_{vertical} = \frac{\Delta L}{L} \quad (3)$$

Where ΔL is the change of the sample's height, and L is the height of the sample before deformation.

Horizontal strain:

$$\varepsilon_{horizontal} = \frac{\Delta d}{d} \quad (4)$$

Where Δd represents the change in diameter of the sample, and d is the diameter before deformation.

While to calculate the E and v the equation below are used:

$$E = \sigma/\varepsilon_{vertical} \quad (5)$$

Poisson's ratio:

$$V = -\varepsilon_{horizontal}/\varepsilon_{vertical} \quad (6)$$

To calculate E and v, we need to examine the stress – strain graph thoroughly to make sure that the value for calculation is only taken from the elastic regime. To increase the accuracy, all manual calculations and measurements were done at least 3 times.

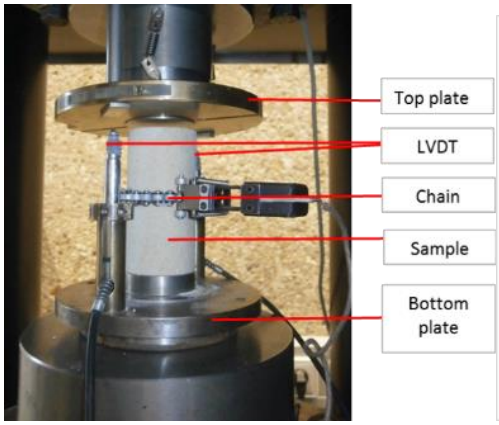

Figure 12.Picture of UCP experiments set-up

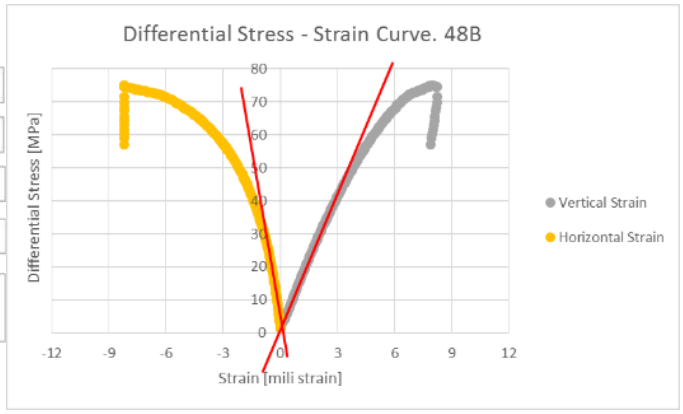

Figure 11. Example of Stress - Strain Plot

For shale experiments, to comply with the height requirement of the apparatus, some aluminum samples were inserted between the shale sample and the pressure bench. Thus the vertical strain recorded by the software used in this experiments was the total strain of both aluminum and shale. To attain the shale strain, the total strain measured need to be subtracted with the aluminum strain. Please refer to the Appendix B.2 to get more detail on the strain calculation of shale $\varepsilon_{vertical}$ and E. For the

Poisson's ratio, as the chain is attached directly to the sample, the method of calculation used is the same with the other rock type.

The comparison between static and dynamic elastic moduli from the samples in this thesis will be presented and discussed in Section 3.2.1, and to get more elaborate perspective on the WMF shale, it will be discussed and compared with other shale in the discussion chapter.

2.4. Confined Pressure Experiments

To obtain the relation between stress condition, rock properties, and the fracture angle, transition stage between fracture mode I and II, several rock samples from different rock types are subjected to confined pressure experiments with different confining pressures. This test was done using a simple triaxial cell, that can accommodate up to 14 MPa confining pressure.

The sample was put in the load cell inside the chamber, with the iron placed on top of the sample. A piston on top of the chamber would transfer the compression force from the pressure bench to the sample. There was only one LVDT in this cell connected from the top plate to the upper part of the chamber which measured the vertical displacement of the system (the sample + iron +piston). Using this apparatus, there was no option to attach a chain to measure the horizontal shortening, thus we could not measure the Poisson's ratio (v). (see Figure 13 for the experiments set-up using the simple triaxial cell).

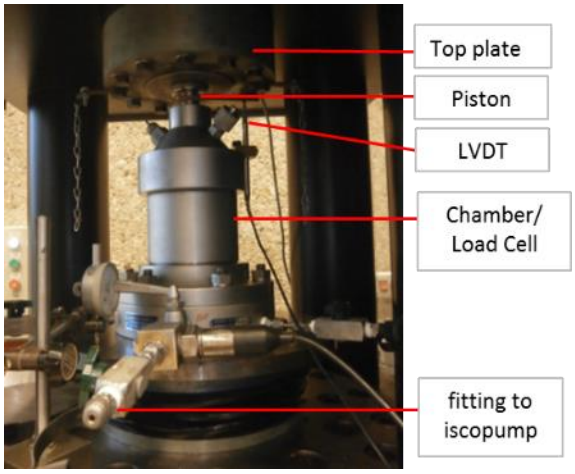

Figure 13. Confined Pressure Experiments set-up - Simple Triaxial Cell

The experiments started by water pressurizing the chamber until the desired confining pressure is reached by using ISCO pump. The pressure acted in all direction. After that, the deformation test was done by applying the compression force to the piston. This force initially would act against the confining pressure, and looked for the right contact with the sample, this is called deviator stress. Thus, the measured stress and strain given by the hoek 3 cell (data acquisition program) were not the sample properties, instead they were the whole system set-up properties. Calibration needed to be done for the Triaxial Test chamber, to get the correction factor that could be applied in order to get the true sample properties. Please refer to Appendix B.1 for the calibration process. To calculate the value of v and E, the Equation 5 and 6 were used.

2.5. Velocity, Seismic anisotropy Measurements, and Dynamic Elastic Moduli

To determine the shale's acoustic properties, all of the samples undergo compressional (P-wave) and shear (S-wave) velocities measurements (Figure 14, on the left). These processes was done under an ambience conditions (without exposing the sample to axial or confining pressure). The velocities would be measured in perpendicular and parallel position to the bedding to identify the anisotropy of the shale.

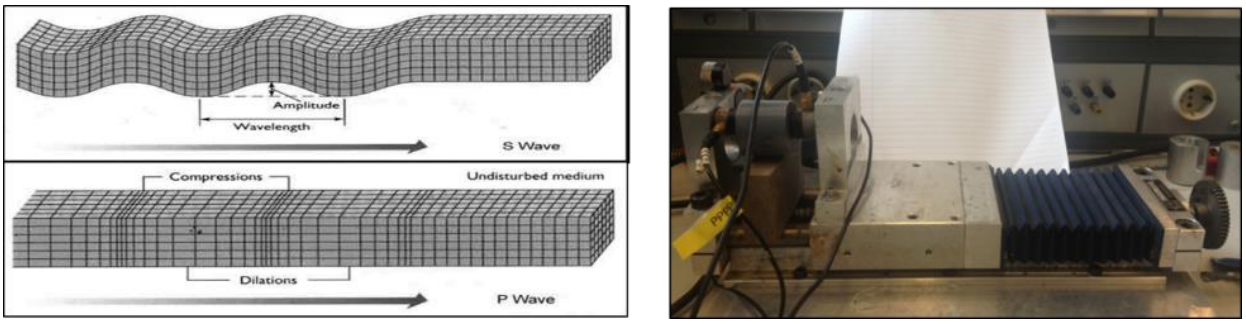

Figure 14. S-wave and P-wave Propagation [7](left), and Velocity measurement set-up (right)

2.5.1. Velocity Measurements

The velocity measurement was done by placing the sample between metal plates which connected to transducer (see Figure 14, right side, for the set-up). The transducer was used with 1 MHz central frequency. From the measurements, a time arrival of the first P-wave (T_p) and the S-wave (T_s) can be acquired (Figure 15 illustrates the arrival time of the wave), and by knowing the distance between transducers (the height or the diameter of the sample), the velocity can be calculated using the formula of Velocity (V) = Distance/Time.

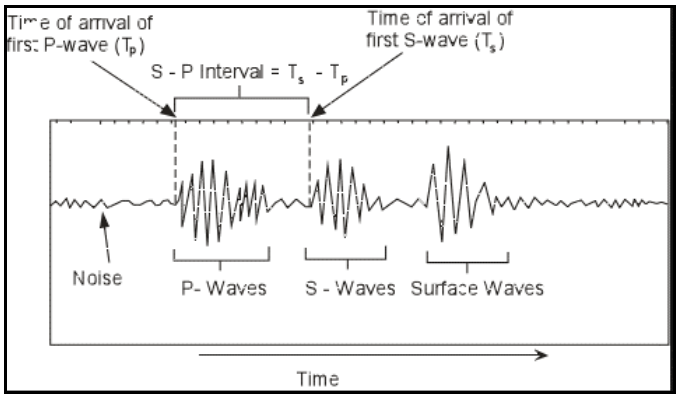

Figure 15. Illustration of P and S-wave arrival time[8]

2.5.2. Seismic Anisotropy Computation

Seismic anisotropy is defined in terms of symmetry direction velocity measurements (Johnston & Christensen, 1995). It is determined as a percentage and calculated using the following formula:

[7] Source: http://www.tulane.edu/~sanelson/Natural_Disasters/eqcauses.htm
[8] Source: http://www.lamit.ro/earthquake-early-warning-system.htm

$\frac{Vmax-Vmin}{Vmax}$ (7)

Where V_{max} is typically the velocity parallel to the bedding and V_{min} is the velocity travelling perpendicular to the bedding. As a result of the high density layered of WMF shale, the velocity travelling parallel to the bedding always goes faster than the velocity travelling perpendicular to the bedding.

2.5.3. Dynamic Elastic Moduli

As the propagation speed V_p (velocity of P-wave), V_s (velocity of s-wave), and matrix density (ρ_m)have been determined, the Bulk (K) and shear modulus (μ) can be attained using the following formula[9]:

$\mu = V_s^2 \rho_m$, (8), and

$K = (V_p^2 - \frac{4}{3} Vs2)\rho m$, (9)

Many shales are considered to be transversely isotropic (TI) with an axis of rotational symmetry aligned perpendicular to the bedding (x-s axis) (Sayers, 1999). It means that the shale samples show change in

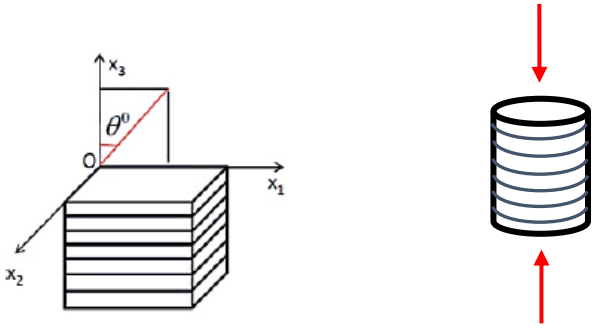

Figure 16. Schematic diagram to illustrate the axis of shale (left), and the orientation of shale during experiments. Red arrows show the experiments (stress) direction (right).

the vertical direction, with respect to the horizontal direction, but have more or less constant velocities in any horizontal direction. However, to compare between static and dynamic moduli, the dynamic elastic moduli determinations are done with the assumption that the shale samples are isotropic. This is based on the fact that both the velocity measurements (acoustic data) and the pressure bench experiments (rock mechanic data) are done in the same direction of the sample. Please see Figure 16 for illustration of axis direction of the shale and sample orientation during experiments.

After the value of μ and K are acquired, the E (Young's modulus) and v (Poisson's ratio) for the dynamic moduli are calculated based on (Mavko, 2003), as follow:

$E = \frac{9K\mu}{3K+\mu}$ (10)

$v = \frac{3K-2\mu}{2(3K+\mu)}$ (11)

[9] Source: Hands out of Fundamentals Borehole Logging, 7th meeting, 2014

2.6. XRF Analysis

To investigate the microstructural/ mineralogy of the WMF sample, 12 samples from different section height were sent to X-Ray facilities department of Material Science and Engineering (3ME), Delft University of Technology. Before being sent to 3ME, the specimens were powdered using the mortal and disc mill manually, but after a while the grinding machine in Steven Lab[10] were used, as it would make the process faster and easier. The apparatus needed to be cleaned after being used for each sample, so that there would be no debris mix between the next sample and the previous sample. The powder samples then were oven dried at low temperature (70 °C) for at least 24 hours, until all the moisture from the mixtures was evaporated.

The XRF analysis measurements were performed using a Panalytical Axios Max WD-XRF spectrometer and the data evaluation was done with the Super Q5.0i/Omnian software. All the powdered specimens was pressed into tablet without binder and measured in vacuum[11].

Due to the fact the ICDD PDF-4 database (advanced database from the International Center for Diffraction Data designed for both phase identification and quantitative analysis) used by the X-Ray department of 3ME did not contain a scorecard for some clay minerals, the quantification and identification of the mineral were done using the Basica[12].

By using Basica, the mineral present in the rock associated with the weight percentages could be determined. The software determined the mineral composition by regressive calculation from the XRF elemental analysis. Hence the result was consistent with the XRF analysis.

2.7. Fracture Characterization

This section explain about the fracture analysis done in this thesis. There are two methods used in this thesis, the one which utilize the micro CT-scan image analysis and the one without (qualitative and quantitative interpretation by inspecting the sample from outside). Sample of Bentheim Sandstone, Granite, Belgium Limestone, Indiana Limestone were not put into the micro CT-scanner because after the deformation test, the crack or fracture was visible from the sample's surface, and with the help of GIMP software[13], the fracture angle could be obtained. The first 5 samples of sandstone were put under the micro CT-scan, but the result did not worth the effort, as it showed approximately the same fracture as what could be seen from outside. So it was decided to skip the process if the fracture was visible with bare eyes. For shale, all samples were put under the micro CT-scanner to attain more detailed characteristics of the WMF shale formation because the fracture was hardly visible from the outside.

2.7.1. Qualitative Interpretation

The qualitative interpretation identified all the fractures in each sample before processing them in quantitative manner. It will gives the qualitative data, like shape, orientation, and help to identify each fracture characteristic before processing it further in quantitative manner.

[10] The lab belong to CITG where grinding machine is kept
[11] Refer to Axios (XRF) report of WMF sample Mutia by Ruud Hendrikx
[12] Basica software is provided by Dr. Karl-Heinz Wolf
[13] GIMP Software is free software available online can be used to measure angle in an image.

Without micro CT-Scan Image

Mode I or extension fracture is recognized from its displacement that is perpendicular to the minimum stress σ3 (parallel to the maximum stress σ1), while mode II or shear fracture develop oblique to σ3 by an angle that depends on rock properties and state of stress, typically develop at 20-30° to σ1 (Fossen, 2010). (Grigs & Handin, 1960) mentioned that shear fracturing may occur along a plane inclined at from few degrees to 45° to the direction of maximal principal stress.

After being exposed to compression, photographs were taken to capture the fractures in each side of the sample (see Figure 17, right side). Labelling was done to all the fractures that was visible with the naked eye, but only the biggest 3-4 fractures would be processed further for the angle measurement.

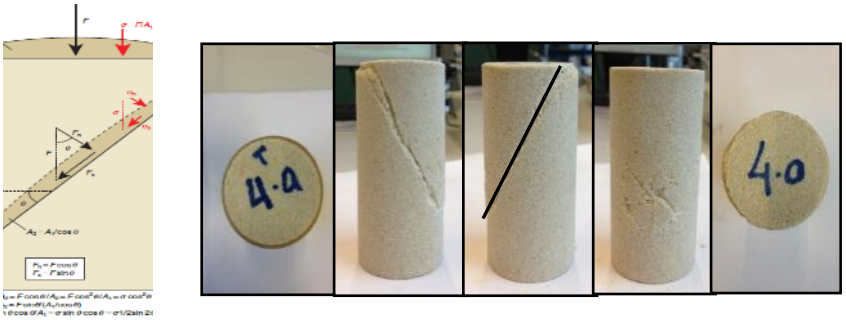

Figure 17. Illustration of fracture mode 2 with 45degree angle to the max principal stress (left)[14], and the picture of fractures in sandstone sample after experiencing deformation test (right).

Using Micro-CT Scanner

Samples were scanned in the X-Ray micro computed tomography (µCT) scanner that measured the density of the samples. Utilizing the VGStudio MAX[15], threshold was applied to eliminate the data that did not contribute to the scanned sample. The output from the µCT-scanner was a set of data consisted of voxels (3D pixels). To further process the data, 3D analysis software Avizo® Fire[16] was utilized with the workflow as described in Appendix E.1.

Qualitative interpretation was done to identify and label each fracture in each sample, such as: fracture orientation, area, shape, et cetera. Based on this identification, elimination was done to the fractures that went beyond the edge of the sample, the suspected existing fracture before deformation, (see Figure 18), and the ones that are very small or hardly visible in a rendering process.

From 12 scanned samples, there are 57 fractures in total. From those number, 17 samples were identified as very tiny and edge-bounded fractures, leaving 40 fractures for further interpretation.

[14] Picture taken from Fossen (2010)
[15] Volume Graphics GmbH (www.volumegraphics.com/en/)
[16] FEI Visualization Science Group (www.vsg3d.com/avizo/fire)

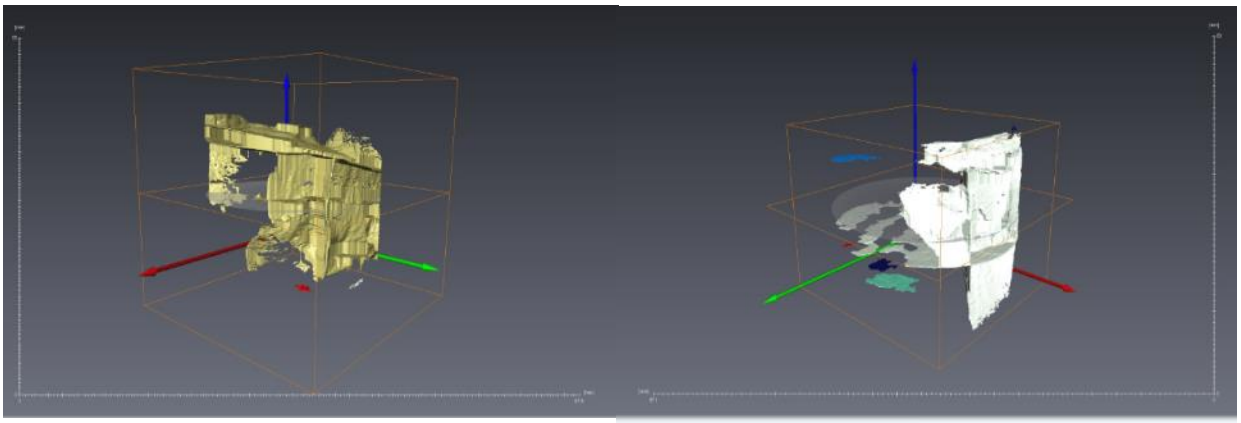

Figure 18. Sample of fractures that goes beyond the edge of the sample (Sample 56, right side), and fractures that is connected to the existing (natural) fracture (sample 59B, left side).

2.7.2. Quantitative Interpretation

Quantitative interpretation aims to get a value for some specific properties of the fractures in all samples.

For the samples that did not undergo the µCT-scanner, the orientation of the fracture was analyzed and GIMP software then was used to measure the fractures angle in a quantitative manner. The result of the fracture angle and its relation with other rock properties will be presented in Section 3.1.3 and discussed further in Section 4.1.1.

For the Shales' sample, micro CT-scanner was used to analyze the fracture characteristic, and with the help of Avizo® Fire these properties of each sample and fractures were quantified as per Table 2 below:

Measurements				**Derivation**	
Each Samples		**Each Fracture**		**Fracture Characteristic**	
Area	[mm2]	Length	[mm]	Tot. Frac Length	[mm]
Volume	[mm3]	Width	[mm]	Tot. Frac Area	[mm2]
		Area	[mm2]	Tot. Frac Vol	[mm3]
		Volume	[mm3]	Number of Frac	[]
		Aperture	[mm]	Avg. Frac Length	[mm]
				Avg. Frac Area	[mm2]
				Avg. Frac Vol	[mm3]
				Avg. Frac Width	[mm]
				Avg. Frac Aperture	[mm]
				Fracture Porosity	[]

Table 2. Fracture characteristics than can be obtained from quantitative analysis

Fracture porosity is calculated using Eq.12 below

Øf = fracture volume / sample volume. (12)

Avizo® Fire software measured the fracture length as the longest axis in the fracture that could be drawn, the width as the longest axis that was perpendicular to the length, and the aperture was derived from calculation and the histogram of fracture thickness. Figure 19 illustrates the length, width, and aperture of a fracture (left) and the histogram of fracture thickness (right).

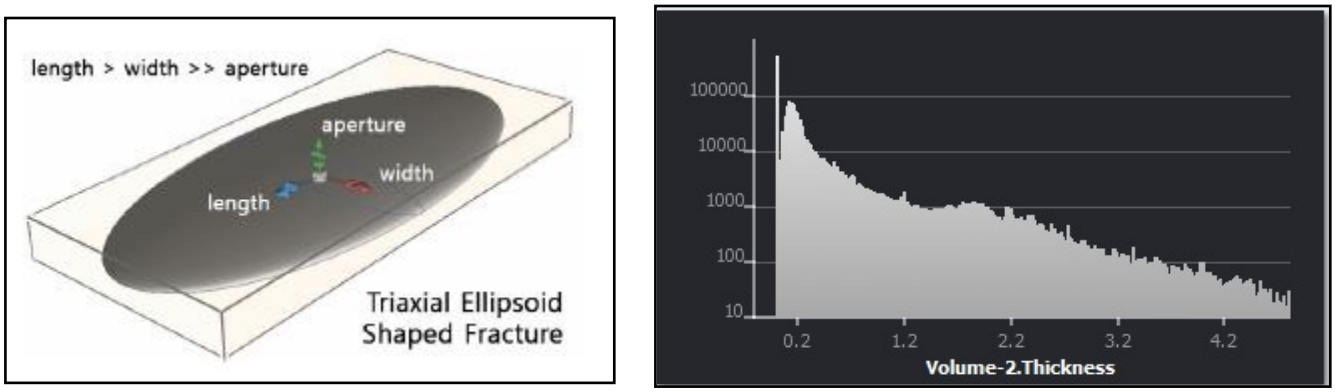

Figure 19. Triaxial ellipsoid shaped fracture (left)[17], and histogram of aperture from sample 26B (right).

(Singhal & Gupta, 2010) mentioned about three types of fracture density:

1. Linear Fracture density: d_1 = number of fractures/sample height (13)
2. Areal fracture density: d_2 = total fracture lenght/sample area (14)
3. Volume fracture density: d_3 = total fracture area/sample volume (15)

A plot of fracture porosity and the fracture densities were made to assess which one of the fracture density type that best matches the WMF shale characteristic.

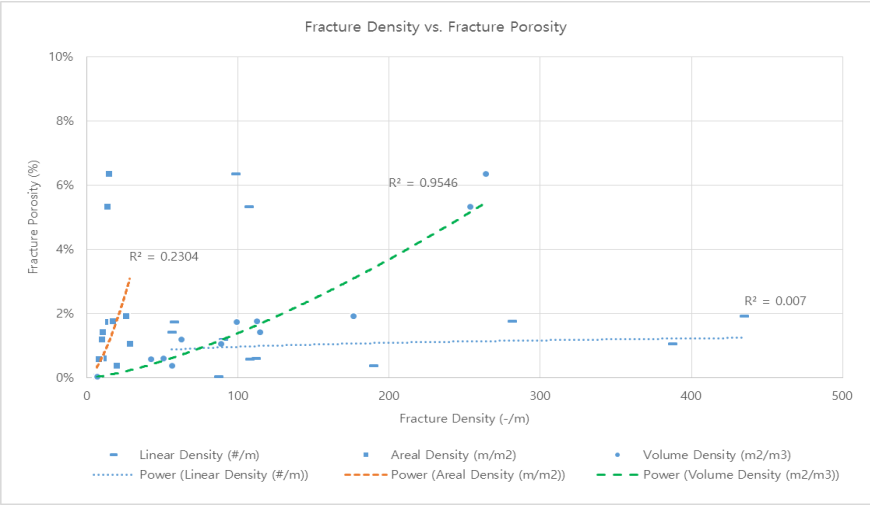

Figure 20. Plot of fracture porosity vs linear -, areal-, and volume fracture densities

Figure 20 shows that the volume fracture density fits the data most accurate, with the highest R^2 of 0.95. Hence d_3 was chosen to characterize the WMF shale.

[17] Source of picture: Fossen (2010)

2.8. Fraccability Determination

This section elaborates on the fraccability index determination with various mathematical model, in terms of brittleness index, fracture toughness, and Young's modulus. Section 2.8.1 explains how the three brittleness indices used in this thesis are obtained, continued by the fracture toughness explanation in section 2.8.2, whereupon section 2.8.3 elaborates on the fraccability index.

2.8.1 Brittleness Indices

Brittleness index (BI) is considered as a key parameter for hydraulic fracturing initiation and propagation in a low permeability rock, like shale formation (Holt, et al., 2011; Yang, et al., 2013). There are three BI used in this thesis:

1. BI average (BI_1) by (Jin, et al., 2014) is a method to define BI in terms of the geomechanical properties of Young's modulus (E) and Poisson's ratio (v)

$$BI_1 = \left[\frac{\frac{100(E-E_{min})}{(E_{max}-E_{min})} + \frac{100(v-v_{max})}{(v_{min}-v_{max})}}{2}\right] \qquad (16)$$

   Where E_{max} and E_{min} are the maximum and minimum E in the formation of interest, and v_{max} and v_{min} are the maximum and minimum Poisson's ratio in the formation of interest.

2. (Holt, et al., 2011; Yang, et al., 2013; Coates & Parsons, 1966) relate brittleness to elastic strain ($\mathcal{E}_{el}$) normalized by total strain at failure ($\mathcal{E}_{tot} = \mathcal{E}_{el} + \mathcal{E}_{pl}$), where $\mathcal{E}_{pl}$ is strain at plastic condition at failure (see Figure 21 for the illustration).

$$BI_2 = \mathcal{E}_{el}/\mathcal{E}_{tot} \qquad (17)$$

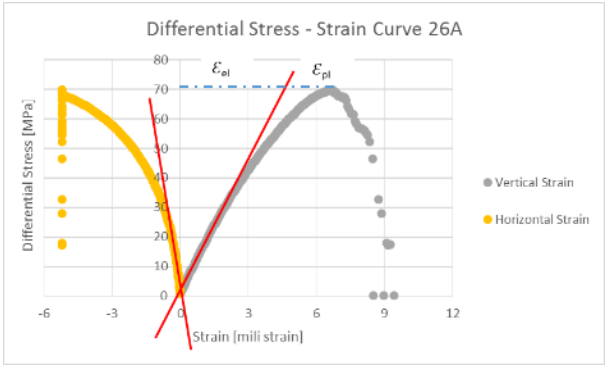

Figure 21. Stress - strain curve from Shale sample 26A to demonstrate how BI_2 can be estimated.

3. The last BI used in this thesis is suggested by (Jarvie, et al., 2007) that relates BI to mineralogy, based on the observations in the best producing well within Barnett Shale.

$$BI_3 = \frac{Q}{Q+C+Cl} \qquad (18)$$

Where Q, C, and Cl represents quartz, carbonate, and clay weight percentage of the rock, respectively.

2.8.2 Fracture Toughness

(Olson, 2003) argued that for fractures with different length and aperture exist in a population of fractures in a sample. Then, assuming critical crack propagation, all propagating fractures should have

the same stress intensity factor (Olson, 2003), which can be related to the fracture toughness (K_{IC}). The fracture aperture can be calculated using the fracture toughness using a formula from (Olson, 2003):

$$d_{max} = \frac{K_{IC}\,(1-v2)\sqrt{L}}{E\sqrt{\pi/8}} \qquad (19)$$

This formula can then be rearranged to:

$$K_{IC} = \frac{d_{max}\,E\sqrt{\pi}}{(1-v^2)\sqrt{L8}} \qquad (20)$$

For each sample, K_{IC} value can be calculated by inserting: d_{max} = average fracture aperture; E = Young's modulus; v = Poisson's ratio; L = average fracture length. The value of E and v are determined from the geomechanical experiments and calculated by using Equation 5 and Equation 6, while d_{max} and L are obtained from the fracture quantitative analysis with the help of micro CT-scanner and Avizo® software.

2.8.3 Fraccability Index Model

Fraccability Index (FI) is widely used to investigate the prospect of hydraulic fracturing in a formation, with a range from 0 to 1.0. Formation with FI = 0 is the worst fracture candidate, and those with FI = 1.0 are the best fracture candidate. Two mathematical models used in this thesis are defined by (Jin, et al., 2014):

1. $FI_1 = \frac{B_n + K_{IC\_n}}{2}$ (21)

FI_1 model the fraccability index in terms of brittleness and fracture toughness, where B_n and K_{IC_n} are normalized brittleness and normalized fracture toughness, and are defined as:

$$B_n = \frac{B - B_{min}}{B_{max} - B_{min}} \qquad (22) \qquad K_{IC\_n} = \frac{K_{IC\_max} - K_{IC}}{K_{IC\_max} - K_{IC\_min}} \qquad (23)$$

Where B_{min} and B_{max} are the minimum and maximum brittleness, and K_{IC_max} and K_{IC_min} are the maximum and minimum fracture toughness for the investigated formation.

2. $FI_2 = \frac{B_n + E_n}{2}$ (24)

FI_2 defined the fraccability index in terms of brittleness and Young's modulus, where Bn and En are normalized brittleness index (Eq. 24) and normalized Young's modulus defined below:

$$E_n = \frac{E_{max} - E}{E_{max} - E_{min}} \qquad (25)$$

Given three different ways and two different ways to define BI and FI, respectively, we can determine six different value of FI in this thesis, namely $FI_{1.1}$, $FI_{1.2}$, $FI_{1.3}$, $FI_{2.1}$, $FI_{2.2}$, and $FI_{2.3}$. Where the first and the second subscript refer to the number of the FI model and BI model. For example $FI_{1.3}$ is the FI which is defined by using FI_1 (eq.21), and using BI_3 (eq.18) to express the B_n (eq.22).

Both mathematical model are being used to obtain the FI by utilized normalized E, BI, and KI_C that requires the use of the same limits in multiple dataset for their minimum and maximum. This limit will be described in Section 3.3.

3 Results

In this chapter, the experimental results are presented and interpreted. The results are grouped based on their relations with the objective of this thesis, which is to answer the research questions.

3.1. Fracture Mode Analysis

In this section, the results of petrophysics, porosity and density, measurements are presented (Section 3.1.1). The results of the geomechanics experiments with unconfined and confined pressure test, and the static elastic moduli are presented in Section 3.1.2. The last part of this section elaborates all of the rock properties obtained from eight different lithologies to investigate their correlations with the fracture angle, which distinguish the fracture mode.

3.1.1. Petrophysics - Porosity and matrix density measurements

The porosities and matrix densities values from the helium pycnometer are shown in this part, and clustered between the WMF shale and other rocks. As for the MWF shales, the height of sample's origin is known, while the other rock samples is unknown.

Table 3. Density and Porosity of Rocks sample

Rock Sample	Matrix Density - mean (gram/cc)	Porosity - mean (%)
Bad Bentheim SS	2.65	23.6
Indiana LS	2.69	17.8
Granite	2.66	2.0
Belgium LS	2.69	0.8
CAV LS	2.77	4.0
DEV LS	2.79	3.2
FAM LS	2.88	8.8
WMF Shales	2.34	3.21

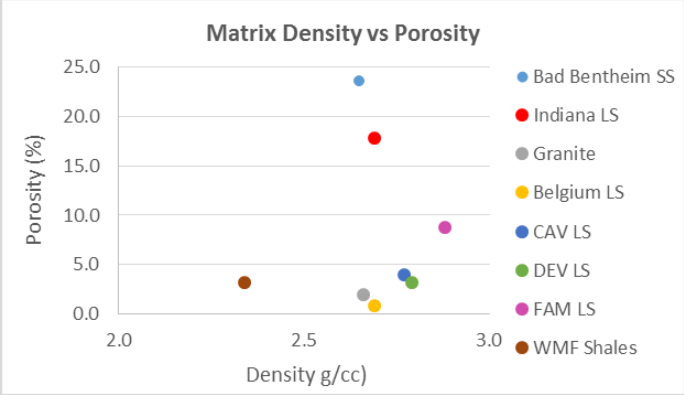

Figure 22. . ρ_m vs. ϕ for different rock types

Table 3 depicts the matrix densities and porosities for different rock types, varies between 2.34 g/cc and 2.88 g/cc and 0.8% and 23.6% respectively. Figure 22 shows that for different rock types the porosities are independent to the matrix densities. Rocks with the same density can have different porosity. For each rock, the measurements are conducted from at least 2 different samples (CAV, DEV, FAM limestone) to 15 different samples (WMF shales).

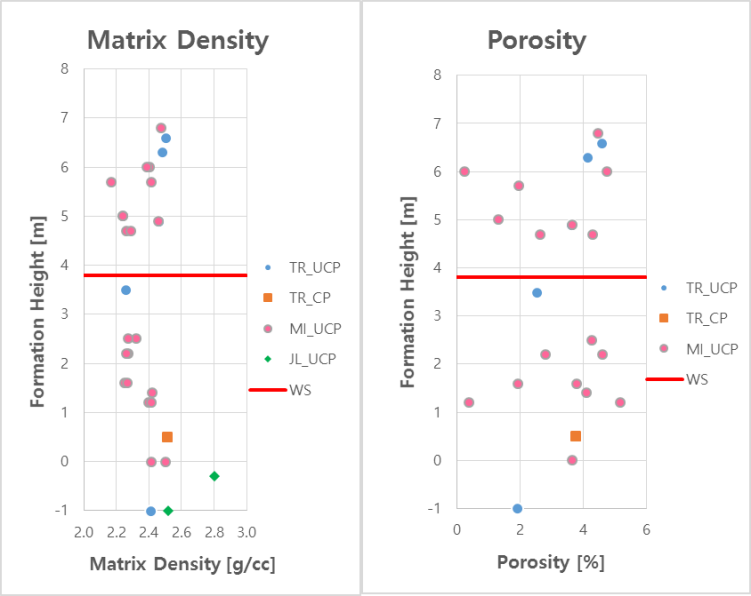

Figure 23. ρ_m and ϕ vs. height of the WMF, with the redline is the WS (left side), and ρ_m vs. ϕ (right)[18]

Figure 23 depicts porosities and matrix densities for WMF varying between 0.26% and 5.19%, and between 2.17 g/cc and 2.8 g/cc respectively. The results show that there is no clear relation between the porosity, matrix density, and the height of the section, even though two samples from the same height have different porosity and matrix densities. It suggests that there is a variation in porosity and density on small scale (cm). To analyze the variation within the WMF, the height is divided into 2 parts, with the Whale Stones (WS) in between.

The graph on the right side in Figure 23 shows that the porosities are scattered with no clear correlation between the upper and lower sections. For the densities, the results show that the matrix density is decreasing towards the WS. This finding corresponds with results of (Lie-A-Fat, 2014) which showed that the matrix density in the upper section is more clustered, and the trend is decreasing towards the WS.

These results will be compared to other literature in other shales in Section 4.2.1.1. The relation between the petrophysics data of the various rocks and fracture mode investigation will be presented on the last part of this section.

3.1.2. Geomechanics

Unconfined Pressure Experiments

The unconfined pressure test (UCP) is done to eight different lithologies, Bad Bentheimer Sandstone, a coarse granite, a highly porous limestone (Indiana LS), a shale (MWF shale), a slightly metamorphic LS (Belgium LS), and 3 different low porosity LS also from Belgium (DEV, CAV, FAM LS), all with horizontal layering to mimic the real layers in the subsurface. The test is done until the first fracture is occurred, audible nearby the apparatus. Figure 24 shows the stress – strain curves for different rock types.

[18] The data points included the results of measurement by J.Fat (JL_UCP), Ravenstein (TR_UCP and TR CP), and myself (MI_UCP)

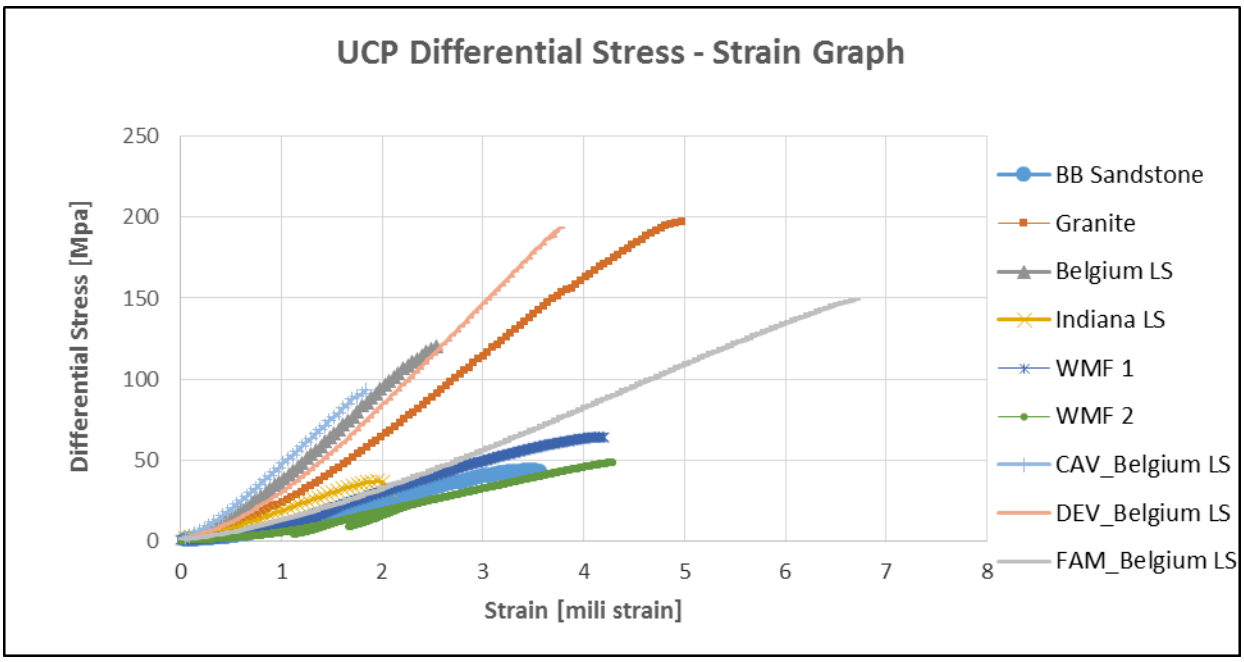

Figure 24. Differential Stress – Strain curves for eight different lithologies.

The curve for each lithology is taken from one of the experiments that had been done in several samples, considering that the experiments were mostly done in more than three samples for each lithology to check the consistency of the result. The peak of each curve in Figure 24 shows the ultimate strength of each rock before first fracture is occurred. The range is about 36 MPa for Indiana LS, and 190 to 200 MPa for DEV LS and granite respectively. The difference of the maximum stress and strain is suspected due to the differences in the petrophysics and other geomechanics properties.

For the WMF shale, the result of the elastic moduli properties are divided into two parts, static and dynamic, as a result from the rock mechanic and acoustic experiments respectively. The result of static moduli will be described here, while for the dynamic will be depicted in Section 3.2.1

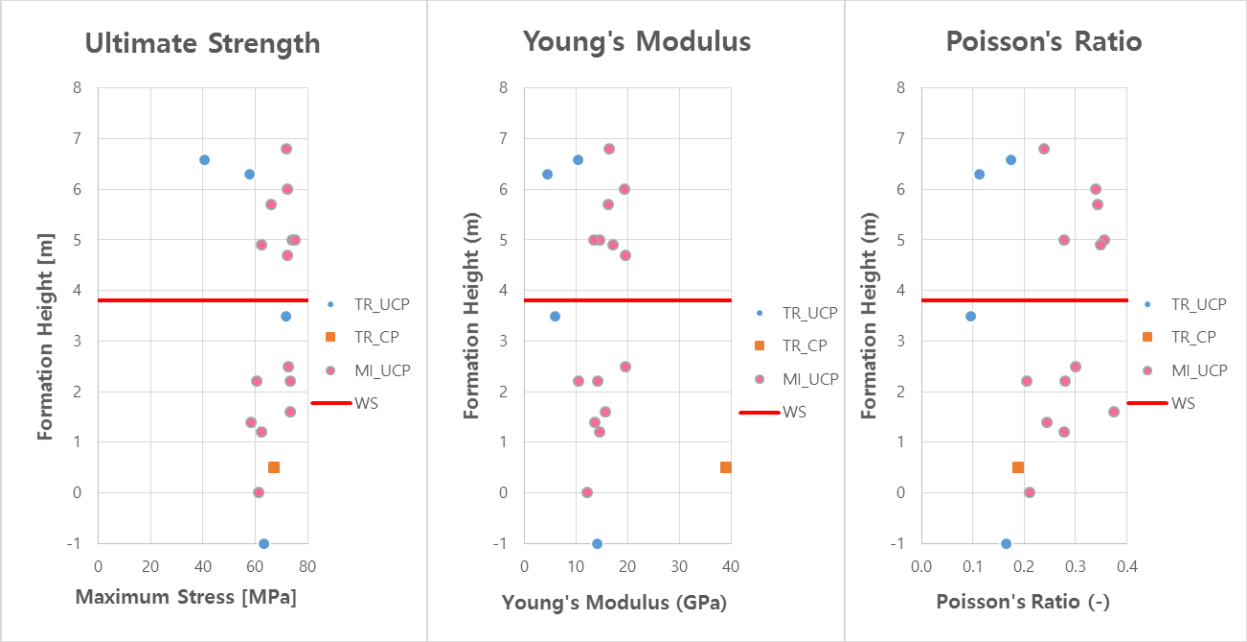

Figure 25. Max Stress, E, and v vs. height of the WMF, with the red line is the WS.[19]

Figure 25 depicts interesting things that from the same lithology (WMF shale) there are variations within the height of the section. The elastic moduli results are different even though they come from the same height, as represent by sample 36A and 36B from the height of 2.2 m. It shows that the heterogeneity in elastic modulus is within cm scale. The same results are acquired from the Bad Bentheimer SS and Indiana LS, which have Young's modulus around 43 to 50 MPa and 17 to 22 MPa respectively, even though their origin are from the same block of sample.

The Poisson's ratio seems to increase slightly towards the WS, but this trend is not clear in the Young's modulus and the maximum stress. The maximum stress below the WS seems to be more clustered than above the WS, while the Young's modulus are scattered within the WMF section, both below and above the WS.

The tabulated results of rock properties under UCP experiments are depicted in Table 4.

[19] The data points included the results of measurement by Ravenstein (blue and orange colors).

Table 4. Rock Properties results under the UCP Experiments. The value is for minimum, maximum, and mean

Properties of the Rock Sample	Sandstone Range	Belgium Limestone Range	Granite Range	Indiana LS Range	WMF Shale Range	Belgium LS_CAV Range	Belgium LS_DEV Range	Belgium LS_FAM Range
Matrix Density (gram/cc)	2.65	2.69	2.66	2.69	2.34	2.77	2.79	2.88
Porosity (%)	23.6	0.8	2	17.8	3.21	4	3.2	8.8
Young's Modulus - Unconfined (Gpa)	16.19 - 18.68 (17.44)	56.16 - 64.94 (61.24)	48.72 - 60.65 (55.14)	17.58 - 22.28 (19.93)	10.58 - 19.66 (15.44)	53.9	59.46	25.48
Poisson's Ratio (-)	0.21 - 0.27 (0.24)	0.13 - 0.21 (0.17)	0.13 - 0.23 (0.15)	0.12 - 0.26 (0.19)	0.20 - 0.40 (0.30)	0.07	0.31	0.18
Maximum Stress (Mpa)	39.66 - 50.68 (45.65)	111.85 - 132.17 (125.18)	116.23 - 224 (188.01)	36.39 - 36.62 (36.50)	58.29 - 75.07 (68.43)	93.2	193.52	148.7
Angle to σ1 (°)	14.76 - 30.91 (22.93)	1.9 - 15.23 (6.03)	2.84 - 19.46 (6.74)	10.03 - 28.04 (19.61)	1.2 - 33.8 (15.7)	19.07 - 24.21 (21.64)	7.95 - 18.13 (12.48)	15.41 - 21.80 (18.29)
Shear Stress	11.01 - 20.70 (16.11)	4.07 - 57.60 (25.92)	6.56 - 69.27 (21.70)	6.44 - 15.19 (11.16)	1.22 - 34.70 (17.96)	28.78 - 34.86 (31.82)	26.51 - 57.23 (40.36)	38.09 - 51.27 (44.13)

Confined Pressure Experiments

Confined pressure (CP) experiments was done to the Bad Bad Bentheimer sandstone (BB SS) and Indiana LS. In total, 10 BB SS and 6 Indiana LS were put inside the simple triaxial test chamber. The results of this test are depicted in Figure 26.

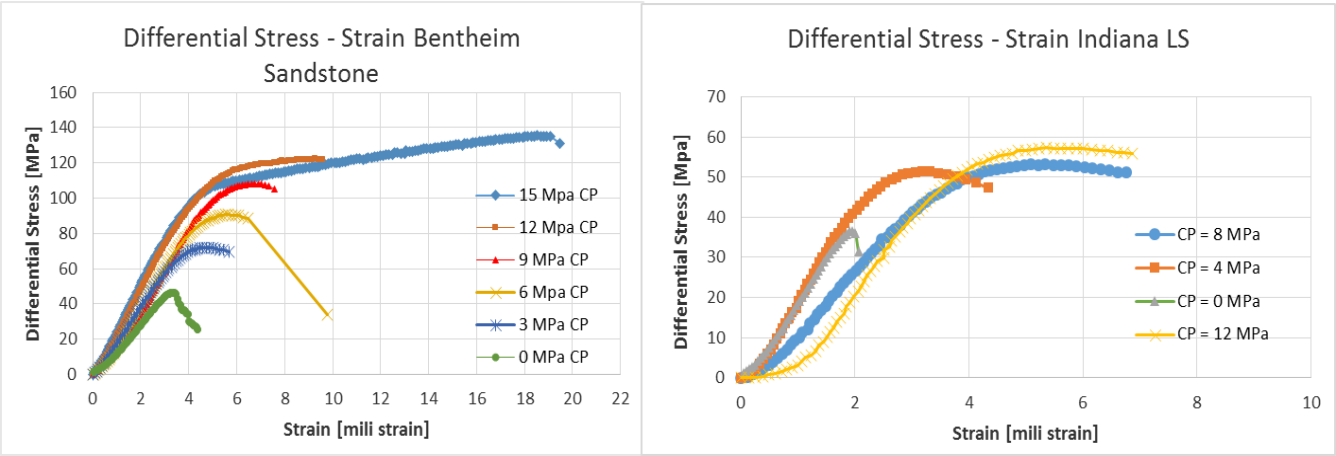

Figure 26. Differential Stress – Strain Plot of Bed bentheim SS (left) and Indiana LS (right)[20]

As mentioned before, the peak of each curve indicates the ultimate strength before first fracture or failure happens, and the slope of the curve indicates the Young's modulus of the rock. Figure 26 depicts

[20] Both of the tests are done using simple triaxial machine test

that for both Indiana LS and Bad Bentheim sandstone, the strength of the rock will be increased by enlarging the confining pressure.

According to (Fossen, 2010), the strength of the rock increases when the confining pressure is raised. This is due to the fact that the confining pressure acts as a support, which will compact the sample and add extra strength to the rock, so that it will be more difficult for the rock to fail, indicated by higher shear stress, and the Young's Modulus is expected to increase. Figure 27 on the right side confirms aforementioned statement, as the same results were obtained from the experiments using Bad Bentheimer sandstone. In addition, the Young's modulus is also closely dependent to the confining pressure. With the coefficient of determination (R^2) > 0.9, the linear relationship between these two parameters has a relatively good fit.

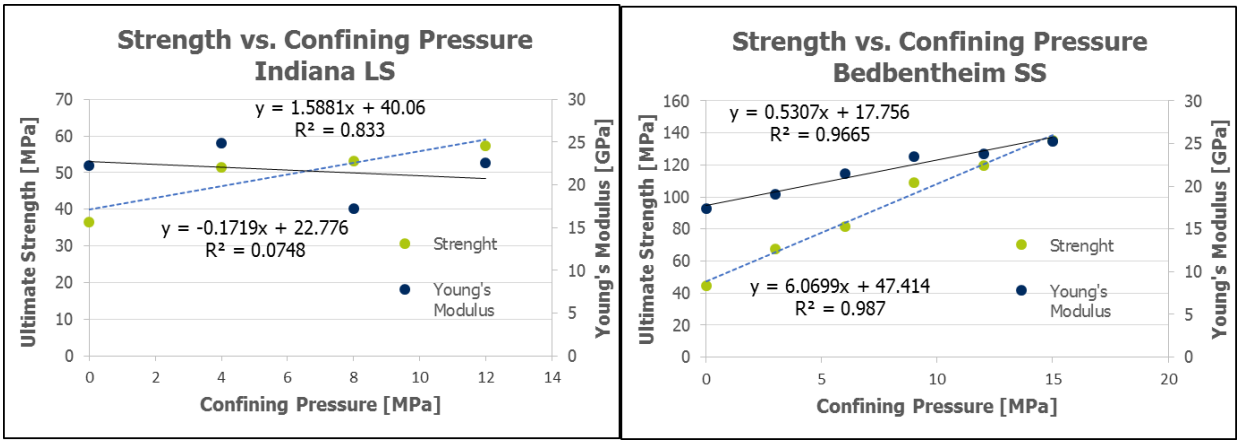

Figure 27. Confining pressure vs strength and Young modulus for Indiana LS (left), and Bad Bentheim Sandstone (right).

For Indiana LS, the positive relationship between the strength and confining pressure is also observed with (R^2 = 0.833), but in contrast with Bad Bentheim sandstone, the Young's modulus does not show positive correlation with the confining pressure. This might be related with the high porosity of Indiana LS, which makes the rock easier to deform, so that when the confining pressure is mounting, the strength increases as well. But at the same time, the vertical strain grows bigger, which makes the Young's modulus even lower.

3.1.3. Relation between Rock Properties and Fracture Mode

To distinguish between the fracture mode I and II, it is important to know the fracture angle (angle between the vertical σ_1 and the fracture plane), as it is one of the factors to distinguish between fracture mode I and II. In this section, Fracture angles obtained from the confined and unconfined pressure test in 8 different rock lithologies and their correlations with each different rock properties are presented. The tabulated result for each rock can be seen in Table 4.

Figure 28. Fracture angle at zero confining pressure. From left to right: BB Sandstone, Granite, Belgium LS, Indiana LS

As depicted in Figure 28, at zero confining pressure, the rocks behave differently. Low-strength rocks like BB sandstone (46.65 MPa) and Indiana LS (36.5 MPa) show a fractures angle at 10 - 35 º with respect to maximum principal stress, display fracture mode II. On the contrary, stronger rocks like Belgium LS and Granite (125 and 128 MPa respectively) have slightly vertical fracture's plane, 6º angle to the vertical σ_1, which display the characteristics of fracture mode I.

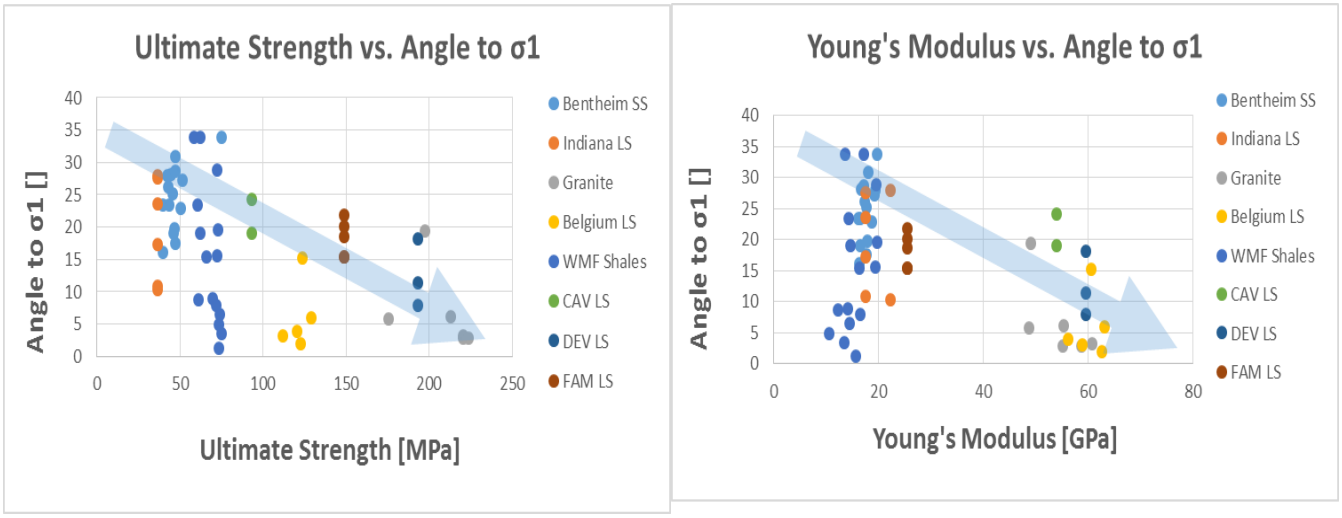

Figure 29. Scatter – plots showing Ultimate Strength and Young's modulus vs. fracture angle for various rock types.

Figure 29 shows the scatter plot between the strength and Young's modulus to the fracture angle for eight different rock types. There might a trend between the fracture angle and the ultimate strength and Young's modulus. As the strength decrease the fracture angle are decreasing, as well as the Young's modulus. Figure 30 depicts the trend also visible in the scatter plot between the porosity and fracture angle, the higher the porosity of one rock will lead to bigger fracture angle if the rock is subjected into stress. But looking those scatter plots, it seems that WMF shale and FAM limestone behave differently. In Figure 29 (left) WMF has high variation of fracture angles at relatively low strength, when it is expected to have high angle, while the FAM limestone in contrast have high fracture angle even though it is considered as high strength rock.

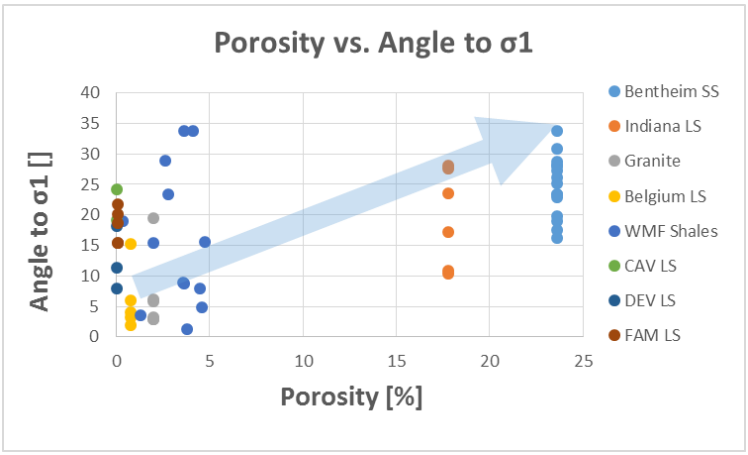

Figure 30. Cross-plot showing porosity vs. fracture angle for eight different rock types

To validate the transitional fracture mode predicted by the Mohr- Coulomb criterion, cross plots between the confining pressure and the fracture are generated for rocks that subjected to confined pressure test (Indiana LS and Bad Bentheim SS). The result are depicted in Figure 31.

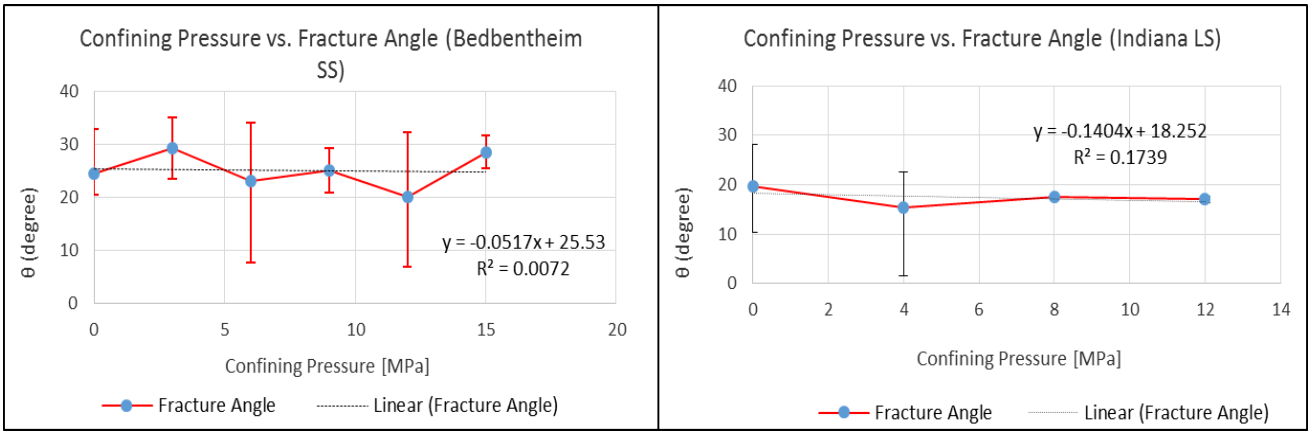

Figure 31. Cross-plot showing confining pressure vs. fracture angle

Surprisingly, the fracture angles do not differ much by increasing the confining pressure. As can be inspected in Figure 31, there is no clear relation between the confining pressure and the fracture angle. The data is scattered with very low R^2. This fact does not comply with the Mohr, Coulomb, or Griffith criterion, which suggests that different styles of fracturing are related to confining pressure (Fossen, 2010)

The result of this experiment will be discussed further and compared with other experiments in Section 4.1.1 to get a bigger picture about the effect of rock properties to fracture transition mode.

3.2. Acoustic Experiments, Mineralogy, and Fracture Characterization of MWF

The results of acoustic experiments, P-wave and S-wave velocity measurement in two different direction, will be presented in Section 3.2.1. With these velocities, the seismic anisotropy and the dynamic static moduli will be estimated. The mineralogy of WMF Shales obtained from the XRF analysis and the use of BASICA software will be presented in Section 3.2.2, while the fracture characterization result of the WMF will be elaborated in Section 3.2.3.

3.2.1. Velocity, Seismic Anisotropy, and Dynamic Elastic Moduli

Velocity and Seismic Anisotropy Measurements

P- and S-wave velocity measurements were conducted in two directions, perpendicular and parallel to the bedding. 22 WMF samples from different height of the WMF stratigraphy were subjected to measurements at ambience condition and no stress applied. To cover more extensive height section, the result presented in Figure 32 also includes the measurements conducted by (Lie-A-Fat, 2014) (the green colored point).

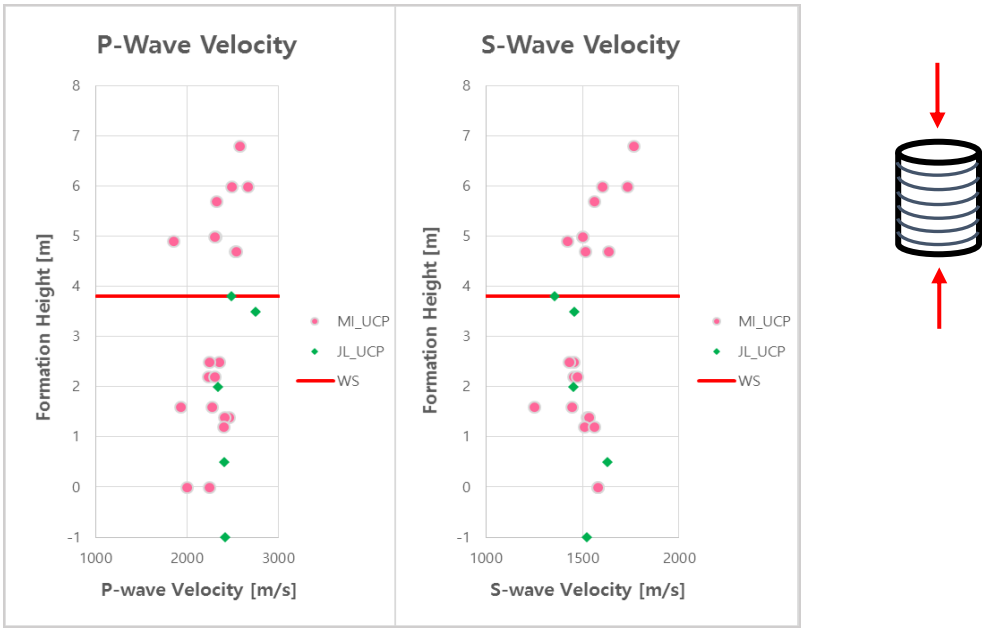

Figure 32. Velocities measured perpendicular to the bedding, with the red line is the WS (left), the sample orientation is shown for clarification (right)[21]

Figure 32 shows that the P-wave travels faster than the S-wave, please note that the horizontal axes have a different range. S-wave velocities seem to decrease slightly towards the WS, it has the same trend like the matrix densities as depicted in Figure 23. Further investigations about their relationship will be explained in section 4.2.1.1. For P-wave velocities the trend is not clear. P-wave velocities measured below the WS are more clustered than the ones above it. The same phenomenon was also depicted in the measurements conducted by (Lie-A-Fat, 2014). P-wave velocity could only be measured on 19 out of 22 prepared samples. This was due to the fact that there were initially fractures presents in the sample. The way P-wave propagates require a vacuum media to travel, the presence of fracture on the sample caused the P-wave could not propagate, and therefore no measurements could be done.

Based on calculated velocities measured in two different directions, the seismic anisotropy can be calculated using Eq. 7.

[21] The data points included the results of measurement by (Lie-A-Fat, 2014)(green points).

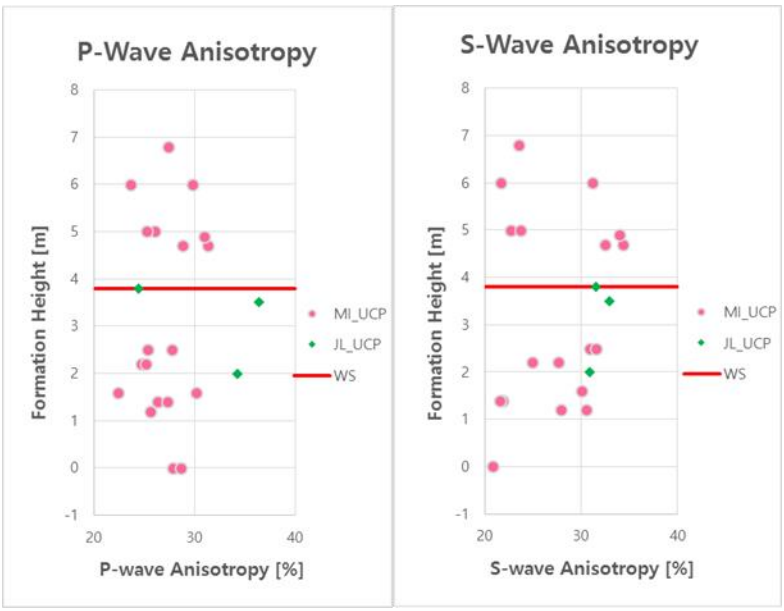

Figure 33. P-wave and S-wave anisotrophy of WMF shale[22]

Figure 33 suggests that the WMF shales are highly anisotropic with the range from around 18% to 36%. It also depicts that the S-wave anisotropy increases towards the WS, but this trend is not clear for the P-wave anisotropy.

Table 5. Comparison between this study and (Lie-A-Fat, 2014)

Literature	P-wave V, Vertical [m/s]	S-wave V, Vertical [m/s]	P-wave Anisotropy [%]	S-wave Anisotropy [%]
MI	**1850 - 2665**	**1250 - 1762**	**22.4 - 31.3**	**18.5 - 34.4**
JL	**2400 - 2800**	**1400 - 1700**	**24.4 - 36.5**	**18.4 - 36.1**

Compared to the results from (Lie-A-Fat, 2014), who did the same experiments on the WMF shale, the results of this study for P-wave velocity and anisotropy are on the lower range. For the S-wave velocity, this study has broader range of results, while the S-wave anisotropy has lower maximum limit. This difference shows that there is variation in velocity and anisotropy, even though some samples are taken from the same height. The sampling area can also be the reason for this, as this study covers broader range of height compared to previous study.

The complete result of the velocities and anisotropies measurement of the WMF samples are presented in Appendix C.

Dynamic Elastic Moduli

The elastic moduli (μ, K) can be determined from the density and acoustic properties (V_p and V_s), and using Equation 10 and 11, the Young's modulus and Poisson's ratio can be calculated. This elastic moduli acquired from the acoustic experiments is called the dynamic elastic moduli.

[22] The data points included the results of measurement by (Lie-A-Fat, 2014) (green points)

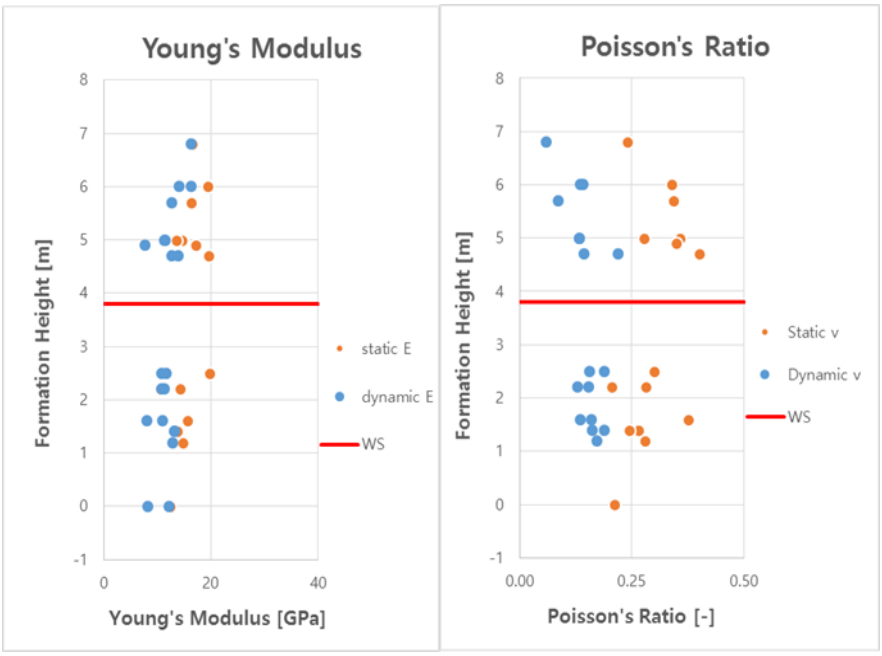

Figure 34. Dynamic and Static Elastic Moduli of WMF, red line is WS.

Figure 34 depicts the dynamic and static of E and v from this study. It shows that for both E and v, the dynamic is lower than static. The Poisson's ratio appears to increase slightly toward the WS for both elastic and dynamic, but this trend is not clear for the dynamic Poisson's ratio below the WS. For the dynamic Young's modulus above the WS, the trend is to decrease a little towards the WS, while for the points below WS, the Young's modulus are scattered without clear trend.

3.2.2. XRF Analysis

In this section the results from XRF analysis will be presented. Based on the XRF results, the mineralogy of 13 different samples from different height sections is determined with its associated weight percentage by using the BASICA software. However, because this study does not include XRD analysis, the validation of the mineralogy is done by referring to the XRF results and the previous XRD result from the same WMF sample (mostly different height), as previously researched by (Lie-A-Fat, 2014). Here we assume that the mineralogy will not differ much along the Whitby section.

The XRF results contain an average error of ±4%, and the values are normalized to 100%. The tabulated result of XRF and mineralogy analysis obtained using BASICA can be seen in Appendix D.

Figure 35 shows the estimated pyrite, quartz, calcite, and clay content with respect to the different height section. The results show that for the same height, there are different results from this study and (Lie-A-Fat, 2014), for example in: sample 47 (height 6.8 m); sample 59 (height 5.7 m); sample 29 (height 1.25 m). It reveals the high heterogeneity of the WMF. Some trends toward the WS are observed, and in general the results of this study correspond with the results of (Lie-A-Fat, 2014), this way both of the studies are complimentary to each other. Calcite content is higher above the WS compared to below WS. Pyrite content corresponds with calcite contents, both of them are increasing toward the WS. Clay content on the other hand is decreasing toward the WS, therefore it correlates negative with the pyrite and calcite content. Quartz content varies between 9% to 21%, and shows higher variation above the

WS. Clay content is very high with minimum value of 50%, indicates that the samples tend to be in the ductile behavior.

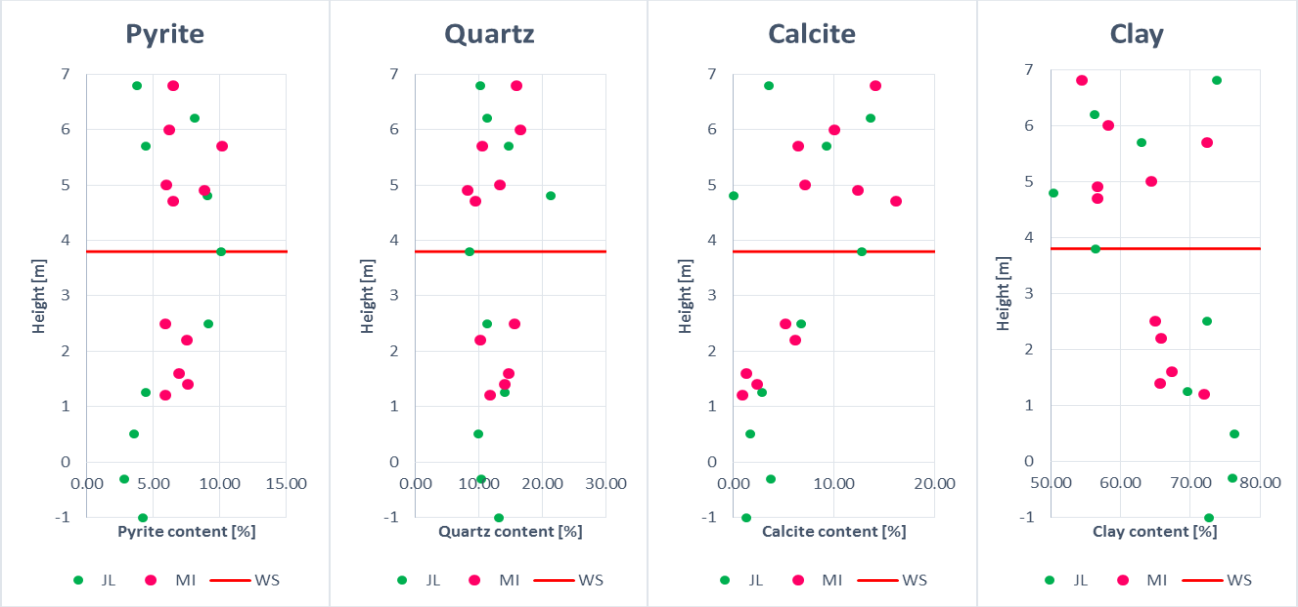

Figure 35. Pyrite, Quartz, Calcite, and Clay content of the WMF along with the height section[23]

Goethite is also assumed to be presence in the WMF shales with average of 8-9% weight. The complete list of calculated weight percentage per sample can be seen in Appendix D. In Section 4.5, the obtained results will be compared to other characteristics obtained in this study to investigate the correlation and explain this phenomenon. The clay, quartz, and calcite content will be compared to other proven shales in section 4.2.2 to see the WMF prospectively.

3.2.3. Fracture Characterization of WMF

This section will present the results of qualitative and quantitative interpretation in order to characterize the fractures of WMF shale. In total, 13 samples were put on the CT-scanner and analyzed further using Avizo® Fire software.

Qualitative Interpretation

Qualitative interpretation was done to identify each fracture in the sample, the shape, orientation, and area. This will help to eliminate fracture that is too small for further characterization, or too big that it goes beyond the samples' border, and the suspected existing fracture (already present before the deformation test).

Some existing fractures are present in sample 59B, 79A, 47, 36A. This might be from the natural fractures or as the effect of the weathering process during the storage or the preparation of the sample.

Figure 36 shows detailed insight of the fractures in four samples. Some fractures are identified as either edge bound fractures or existing fractures. For example, sample 59B depicts horizontal fracture (gold color, circle shape) that is present before the sample is subjected to pressure test. The same type of

[23] Include data from (Lie-A-Fat, 2014), green points

fracture was also present in sample 47 (note the oval, horizontal gold color). While for sample 79A and 36A, the presence of natural fracture is seen from the massive fracture (79A) that is also visible with bare eyes, and the white color fracture (36A) that goes beyond the edge of the sample.

Those kind of fractures hence were eliminated from further quantification process.

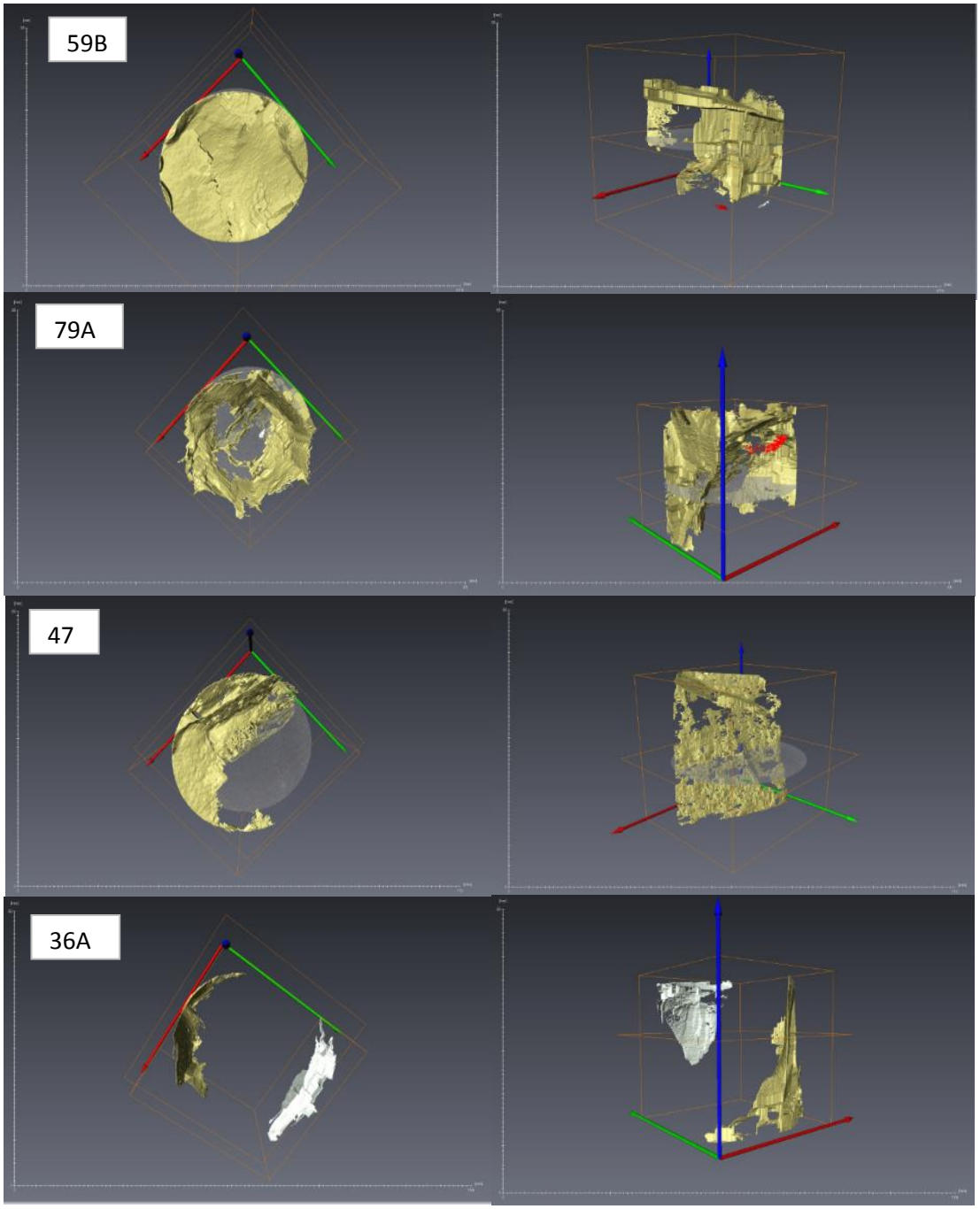

Figure 36. The result of Image analysis from CT-scan data from sample no 59 B, 79 A, 47, 36 A, shows the presence of natural fractures and fractures those go beyond the edge of the sample. Please note that a pair of pictures in one row are belong to the same sample, and the same color lead to the same fracture (in each sample).

Quantitative Interpretation

Some values of specific properties for each fracture in each sample can be obtained from the quantitative interpretation done in this study. The results of these properties per sample are depicted in Appendix E.

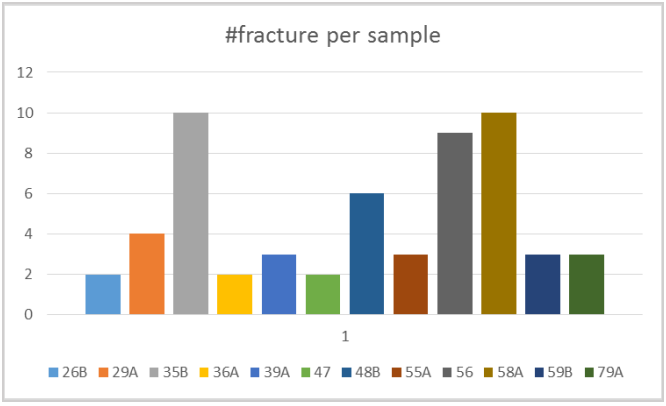

Figure 37. Amount of fractures in each sample

Figure 37 depicts the amount of fractures in each sample. The most fractures are present in sample 35B, 56, and 58A. Cross plots are made between the strength and toughness of the sample, and the amount of fractures, but the results show that there is no clear correlation (Appendix E.2). From the stratigraphy position, 35 is located between CBD (Canon Ball Dodger), while 56 and 58 are above WS. The only reasoning left is that those three samples show more brittle behavior[24] compared to the other samples, that is why they end up having more fractures. Other fracture characteristics obtained from this study are the fracture area, - volume, - length, - width, - aperture, and - porosity. The results of this quantification are shown in Table 6.

The result shows that each sample has different characteristics, and they vary greatly. For example, the porosity varies from 0.0% to 6.37%, while the average fracture volume range from 2 into 336 mm^3, even though they have been subjected to same treatment and test. This again confirms the heterogeneity of the WMF Shales.

[24] Brittle behavior here is refer to a condition in the differential stress – strain, which the rock specimen has less or almost no plastic regime compare to the other rock sample.

Table 6. The result of quantification process (the complete result is depicted in Appendix E.2)

Sample	Avg frac area	Avg frac vol	Avg frac length	Avg frac width	Avg frac aper	Fracture Porosity
#	mm2	mm3	mm	mm	mm	[-]
26b	57	2	11	1.31	0.28	0.03%
29a	331	39	13	4.24	0.21	0.60%
35b	232	25	8	3.58	0.17	1.91%
36a	1167	205	31	11.92	0.54	1.73%
39a	391	74	13	3.80	0.43	1.19%
47	1571	194	26	12.94	0.25	1.41%
48.b	163	11	12	1.85	0.21	0.37%
55a	214	29	11	3.58	0.28	0.57%
56	419	66	11	4.06	0.17	1.77%
58a	118	14	9	2.78	0.18	1.06%
59b	1281	270	15	7.83	0.39	5.35%
79a	1393	336	16	9.78	0.43	6.37%

To determine whether there is relationship between fracture length, - width, and - aperture, some cross-plots are made and the results show that fracture length has a positive, almost linear, correlation with the fracture width as depicted in Figure 38.

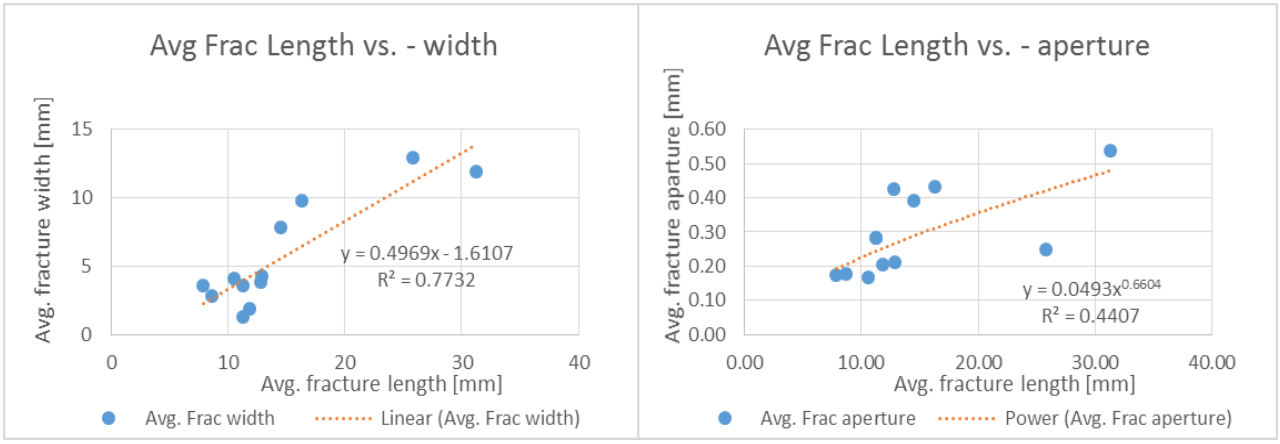

Figure 38. Cross-plots showing the relationship between Avg. frac length vs –width (left), and - aperture (right)

According to (Olson, 2003), the aperture will have a scale of power 0.5 to the length ($D_{max} = x.L^{0.5}$), while (Klimczak, et al., 2010) wrote that these power law exponents vary between 0.2191 and 0.6915. Figure 38 on the right side shows that this study has a result of power 0.66, which is against Olson theory. This phenomenon will be discussed later in Section 4.6.

To check whether there is correlation between frac area and frac vol, - width, - length and – aperture, some cross plots are made as in Figure 39.

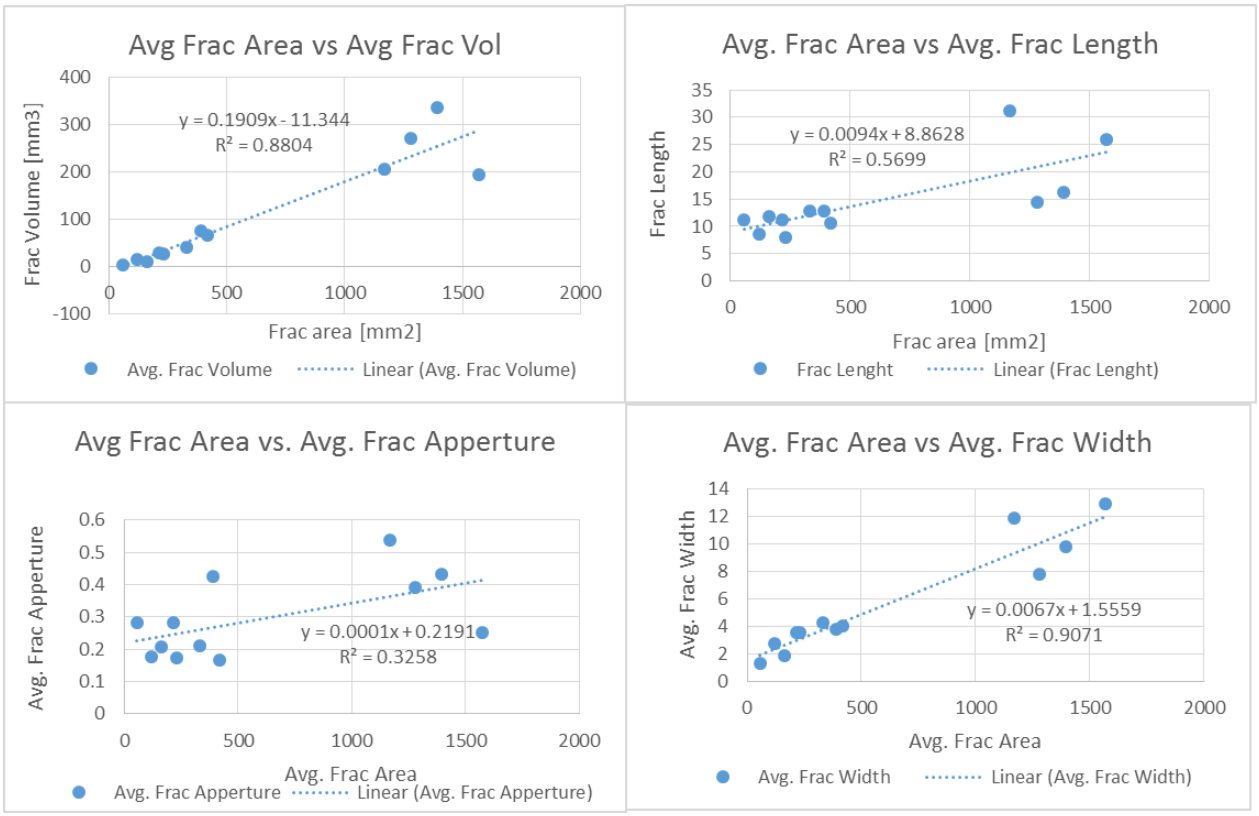

Figure 39. Cross –plot showing the correlation between Avg. Frac Area and Avg. Frac Vol, - length, - aperture, and width.

The results show that fracture area has a positive linear correlation with the other 4 measured properties as depicted in Figure 39. On the upper left corner, there is one outline that belongs to sample 47. The cause of its lower fracture volume, despite the fact that it has biggest fracture area, is suspected to be the aperture. This is supported by Figure 39 bottom left, which shows that this sample also has lower fracture aperture. The coefficient of determination fit best between average fracture area and avg. fracture width (R^2 = 0.9071). It indicates that one can predict the fracture width if the fracture area is known, or vice versa. But this will need to be validated further with more dataset.

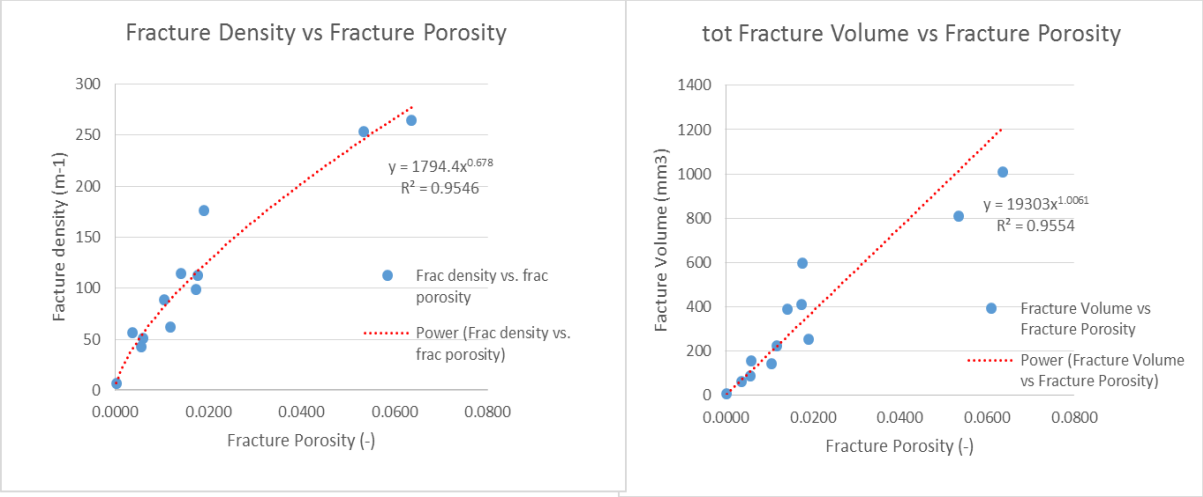

Figure 40. Cross - plot of Fracture density and - volume, to the fracture porosity

Figure 40 reveals that fracture porosity is highly dependent to fracture density (left), and fracture volume (right). The coefficient of determination (R^2) shows high value which means that this correlation has high confidence level, and it also means that one can estimate the fracture porosity by knowing the fracture density and or – volume.

To incorporate the geomechanic result into the quantification result, a cross plot is generated in Figure 41 to investigate the dependency of fracture length per sample to the Young's modulus and maximum stress applied.

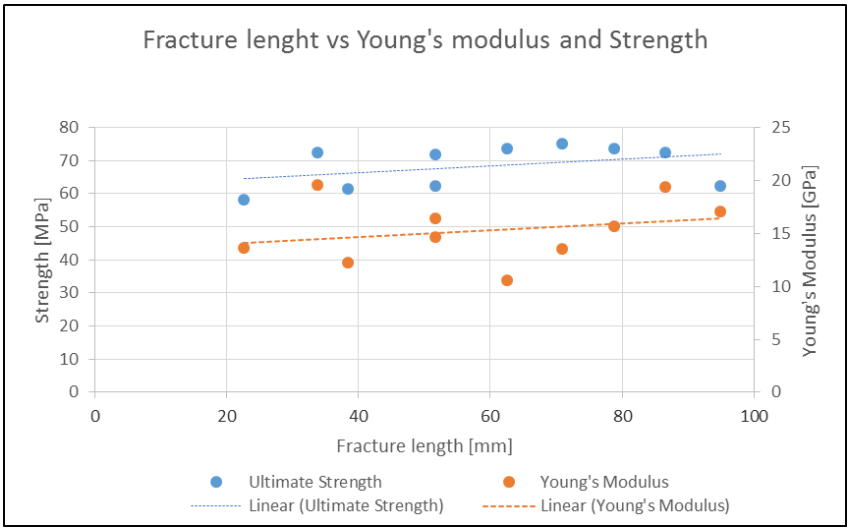

Figure 41. Cross plots showing the tot. frac length vs Young's modulus and ultimate strength

Figure 41 shows that both Young's modulus (E) and ultimate strength tends to have the same correlation with the fracture length. In general, it reveals that for WMF, the higher the ultimate strength and E, the longer the fracture length. Total fracture length is an accumulation of individual fractures length, and as previously mentioned the more brittle the shale, it is likely to form more fractures which also relate to the higher E and strength (steeper slope in the strain – stress diagram). It will be discussed further in Section 4.6.

3.2.4. Fracture Toughness

Fracture toughness can be obtained by combining the result of geomechanic experiments (Young's modulus (E) and Poisson's ratio (v)), and quantitative fracture characteristics (average frac length (L) and average aperture (d_{max})), using eq. 20 in Section 2.8.2, from Olson (2003). The results are depicted in Figure 42.

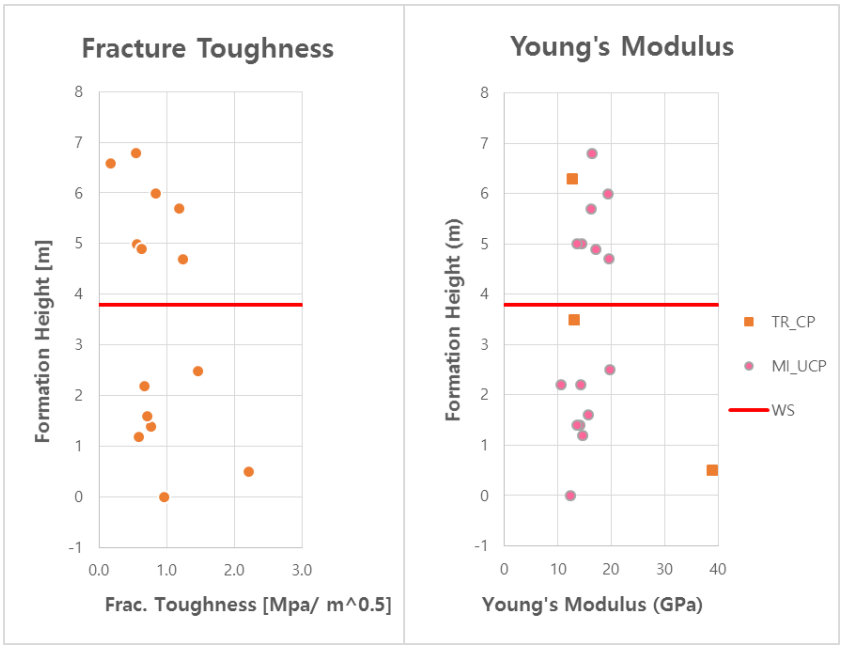

Figure 42. Fracture toughness within WMF section, red line is WS[25] (left), and the Young's modulus plot for clarification in the description (right).

The values of fracture toughness range from 0.17 - 2.2 MPa/$m^{0.5}$ within the WMF section, with slightly increasing trend toward the WS. It is noticeable from Figure 42 that the fracture toughness seems to have the same trend as the plot of Young's modulus. This implies that among the other factors controlling the fracture toughness, the Young's modulus is the most dominant factor. This correlation and other factors related to the fracture toughness will be discussed further in Section 4.7.

The point at the height 0.5 and 6.6 m are coming from sample TR 2A and 49 A from (Ravenstein, 2014). The writer uses the raw data from the experiments to get the value of toughness, to get more coverage of the WMF section.

[25] Experiments at the heights of 0.5 and 6.6 m are conducted by Ravenstein (2014)

3.3. Brittleness Indices and Fraccability Indices

In this section, we will elaborate some of the data from the afore results to obtain the Brittleness Index and Fraccability Index as described in Methodology Section 2.8 and relate it to the fracture mode analysis (fracture angle).

Brittleness Indices

Figure 43 depicts the results of Brittlenes Index; (1) calculated using average technique of Young's modulus (E) and Poisson's ratio (v): $BI_1 = \left[\frac{\frac{100(E-E_{min})}{(E_{max}-E_{min})}+\frac{100(v-v_{max})}{(v_{min}-v_{max})}}{2}\right]$ (Jin, et al., 2014); (2) calculated using the elastic strain and total strain: $BI_2 = \mathcal{E}_{el}/\mathcal{E}_{tot}$ (Holt, et al., 2011; Yang, et al., 2013; Coates & Parsons, 1966); and (3) calculated using the weight percentage of Clay, Quartz, and Carbonate contents: $BI_3 = \frac{Q}{Q+C+Cl}$ (Jarvie, et al., 2007)

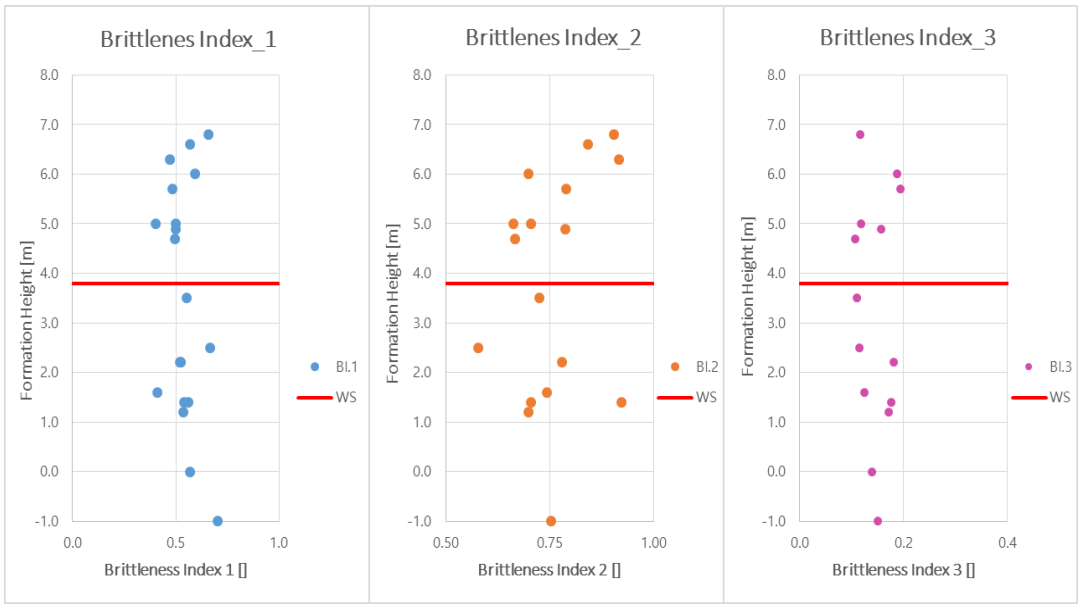

Figure 43. BI_1, BI_2, and BI_3 plot against the section height of WMF.

All three brittleness indices have almost the same trend. BI_1 and BI_3 are slightly decreasing toward the WS, while for BI_2 the data are more scattered and do not show clear trend below the WS. As BI_1 is calculated using the averaging value of E and v, the limit of E and v in this study is directing the value of BI_1. BI_1 for this study range from 0.21 – 0.85. It has been calculated with the limits of E_{min} and E_{max} of 4.31 and 19.66, and v_{min} and v_{max} of 0.09 and 0.40 from the WMF sample in the static data respectively. BI_2 in this study range from 0.58 to 0.92, and it depends on the strain of the sample it selves. It does not correlate with any limit of the data set. BI_3 varies from 0.11 to 0.19. It mainly depends on the mineralogy data of the sample, and the same as BI_2, it is independent from any limit of the data set. Table 7 below shows the limit for each BI calculated in this study.

Table 7. BI limit for this study

	BI1	BI2	BI3
min	0.21	0.58	0.11
max	0.85	0.92	0.19

These obtained brittleness indices will be analyzed further in Section 4.3. And in Section 4.2.4, BI_1 will be compared to other BI_1 from promising shale, to place the WMF in a bigger picture.

Fraccability Indices

As described in the methodology, Section 2.8.3, Fraccability index (FI) is calculated from the normalized data of Brittlenes index (BI) and fracture toughness (KIC), or Young's modulus (E). $FI_{.1.1}$, $FI_{.1.2}$, and $FI_{.1.3}$ are related to the Brittleness index and fracture toughness, while $FI_{.2.1}$, $FI_{.2.2}$, $FI_{.2.3}$ are related to the Brittleness index and Young's modulus.

$$FI_1 = \frac{B_n + K_{IC\_n}}{2} \quad ; FI_2 = \frac{B_n + E_n}{2} \quad \text{(Jin, et al., 2014)}$$

The B_n, K_{IC_n} and E_n are calculated using Equation 22, 23, and 25 respectively. The second subscript refers to the BI, for example FI_{11} means FI_1 and using the BI_1 to calculate the B_n.

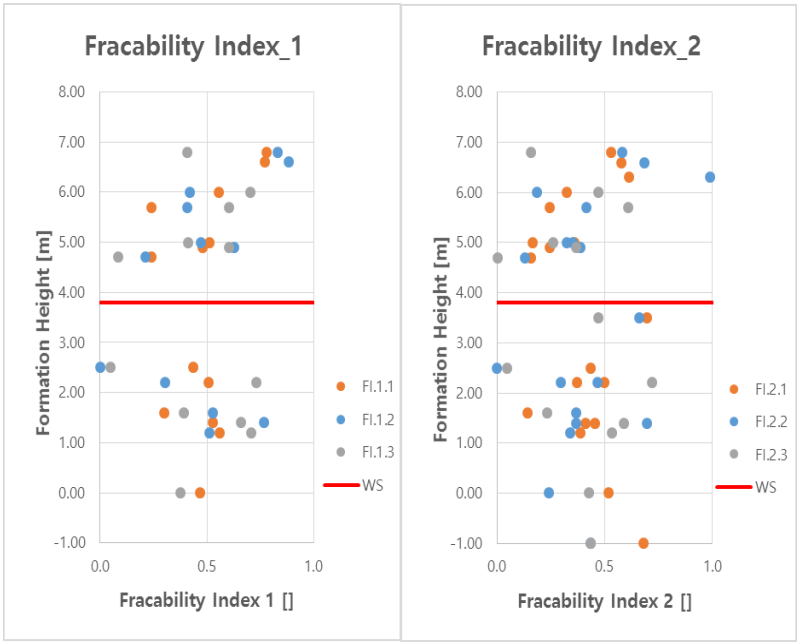

Figure 44. Fraccability Indices of WMF

Figure 44 shows the fraccability indices for this study. In general, the fraccability indices follow the same trend as the brittleness indices, as the value is calculated from the normalized BI and another factor, normalized fracture toughness (K_{IC}_n) or normalized Young's modulus (E_n). The fraccability indices are highest in the upper part of WMF section, suggesting the most potential space for hydraulic fracturing, and decreasing toward the WS, while in the lower part we could not see any clear pattern. The values in the left plot (Fraccability Index_1) are determined with the limits of fracture toughness, $K_{IC\ min}$ and $K_{IC\ max}$

of 0.17 and 1.45 MPa $m^{0.5}$, and the limit of different BI as depicted in Table 7. For Fraccability Index_2 on the right plot, the values of FI are calculated using the same limit of BI as in Table 7, and limit of E_{min} and E_{max} of 4.31 and 19.66.

The absence of data point in Fraccability Index_1 plot in between 3 to 4 m height is due to the unavailability of the fracture toughness data on that section, CT-scan data is not available. Table 8 below shows the limit of different WMF fraccability indices in this study.

Table 8. Fraccability indices of WMF obtained in this study

	FI 1.1	FI 1.2	FI 1.3	FI 2.1	FI 2.2	FI 2.3
min	**0.25**	**0.00**	**0.05**	**0.14**	**0.00**	**0.00**
max	**0.78**	**0.88**	**0.73**	**0.70**	**0.99**	**0.72**

To get a bigger picture of the fraccability of WMF compared to other shale formation, the FI from this study will be plotted together with other shale in Section 4.2.5. And to analyze the phenomenon, the obtained fraccability indices will be discussed further in Section 4.3.

Brittleness Index and Fracture Mode

Brittleness Index for 8 different lithologies investigated in this thesis are calculated, with the results that are depicted in Table 9.

Table 9. BI.2 results for 8 different lithologies

Lithology	Sample #	BI.2	E
WMF Shale	35b	0.742857	15.44
SS	1a	0.880597	17.44
Indiana LS	1a	0.907173	19.93
Belgium LS	3	0.930233	61.24
CAV	1	0.944444	53.9
FAM	1	0.955224	25.48
Granite	3	0.959596	55.14
DEV	1	0.973684	59.46

$BI._2$ is chosen to compare the BI from various rocks because of several factors. First, the availability of data sample. Second, it is believed to better represent the real Brittleness Index if we want to compare it to other rock samples, as it does not limit and relative to its own dataset.

FI cannot be generated because to calculate the FI either K_{IC}_n or E_n is required. To calculate K_{IC}_n or E_n we need a dataset of E and K_{IC} values from some certain interested sections (height). As the height of the sample in this thesis is unknown, we cannot compare the result within any sections, and neither K_{IC}_n nor E_n can be generated.

To investigate the dependency between BI and fracture angle, and BI and Young's modulus, these parameters are plotted against each other in Figure 45.

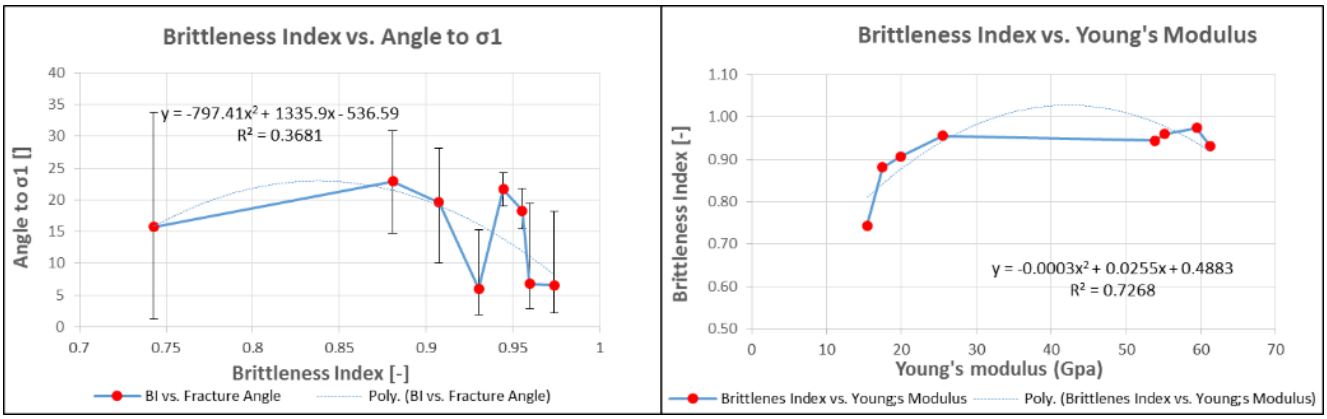

Figure 45. Cross-plot showing BI_2 vs. fracture angle and BI_2 vs. E for eight different lithology.

(Jin, et al., 2014) stated that there is a positive correlation between Brittleness index and Young's modulus. Figure 45 confirms that this statements hold for this experiment with 8 different lithologies. These plots depict that there is negative correlation between BI and fracture angle (left), and positive correlation between BI and Young's modulus with relatively good fit (right). Based on this relationship, a vague conclusion can be drawn that there will be a negative relationship between Young's modulus and fracture angle, which coincidentally fits with the fact in Figure 29.

4 Discussion

In this chapter, the results depicted in Chapter 3 will be discussed further. Some correlations will be calculated to investigate the relationship between one property to another property of the rock, and comparison will be made to compare the results of this research with results of other literatures. The aim is to investigate whether some characteristics of the rock have bigger influence to the occurrence of fracture mode 1 or 2, compared to the other characteristics, and if yes, what they are. And for the WMF characterization, the aim is to determine whether the WMF characteristic is potential for future gas exploration, by comparing the result of WMF characteristic with other shale's characteristic which is proven as a promising gas reservoir, ie. Barnett- and Haynessville shale.

4.1. Fracture Mode Analysis

4.1.1 Relation between Confining Pressure and Fracture Angle

In this section, the results of this research as depicted in Section 3.1.3 will be elaborated with other results from other literatures, to check the relevance and the consistency between the results.

(Ramsey & Checter, 2004) conducted some experiments using Lorano Bianco Carrara marble of Italy, which is relatively homogeneous and isotropic. The specimens were dog bone shapes, and the results showed that the transition from extension fracture (mode 1) to shear fracture (mode 2) is continuous, with the fracture angle increasing as the confining pressure increases.

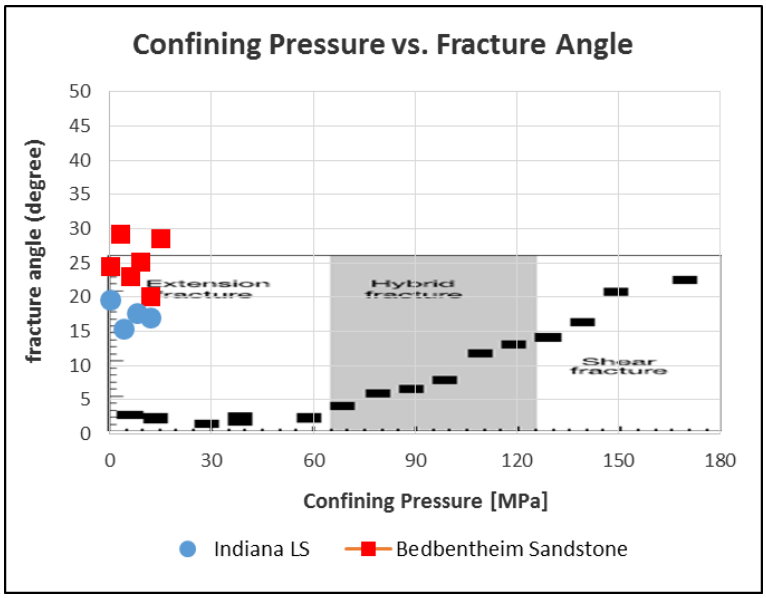

Figure 46. Comparison of this thesis results and results of (Ramsey & Checter, 2004) (black rectangle points).

The plot in Figure 46 depicts that for Indiana Limestone and Bad Bentheim sandstone (result of this thesis), fracture mode II is already developed at zero confining pressure, and the fracture angles are

independent to the confining pressure. Results of Ramsey and Chester, in the other hand, show different results. At zero confining pressure, the angle displays fracture mode I which transforms to fracture mode II gradually as the confining pressure increases.

Despite the fact that all those 3 samples are relatively homogeneous, and isotropic rock, the experiments were done at different confining pressures. This research was done with the confining pressure up to 15 MPa, while Ramsey and Chester carried the experiments up to 180 MPa. Assuming that the results of this experiments will not differ so much with the increasing confining pressure, recall Figure 31 both experiments show that fracture angle does not mainly depend on the confining pressure for isotropic homogeneous rock. These results also do not fully support a theory of continuous transition from extension to shear fracture based on the extrapolation of the Mohr – Coulomb Envelope into the tensile field.

The reasoning for this different behaviour could be because of the different rock strength, as Bad Bentheim SS and Indiana LS are considered to be a low strength rock (46.65 MPa and 36.5 MPa respectively), while the Lorano Bianco Carrara marble of Italy has higher strength of 62.3 MPa[26]. This is supported by the results of experiments conducted for the purpose of this thesis which shows that the fracture angle is mainly dependent to the rock strength, which probably related to the porosity as well (Figure 29 and Figure 30).

4.1.2 Relation between Confining Pressure, Rock Strength, and Young's Modulus

The increasing confining pressure makes the rock becomes stronger, which can be observed from the elastic regime (the curve becomes steeper, as the stress is increase with the same percentage of strain). This will make the Young's modulus higher. This kind of observation is presented for example by (Grigs & Handin, 1960) and (Handin & Hager, 1957).

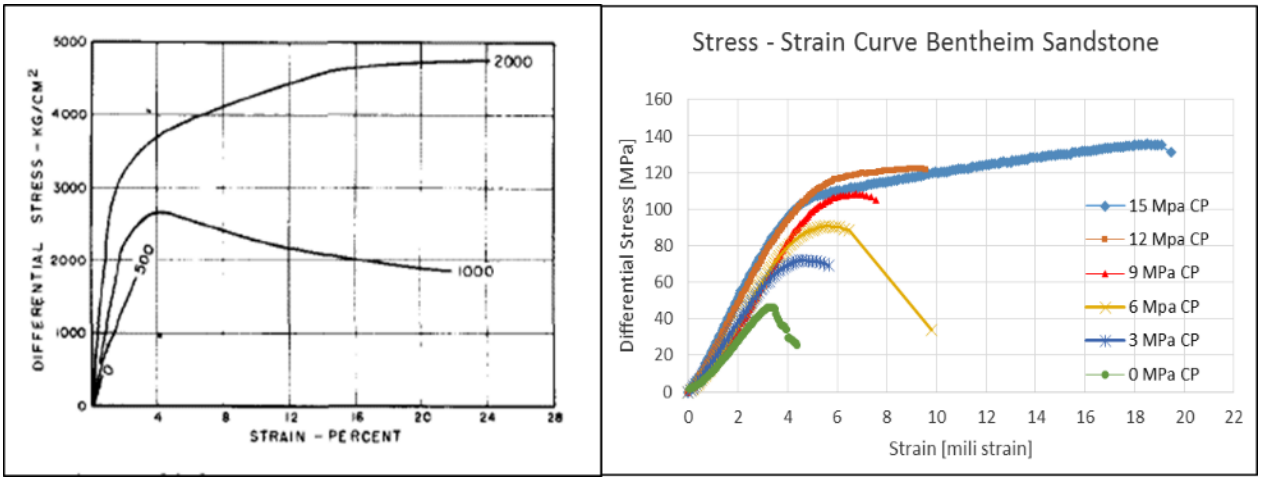

Figure 47. Ilustration of Differential stress – strain curve of Barns Sandstone (left)[27], and Bed Bentheim Sandstone (right)

Figure 47 depicts the plot of differential stress – strain from the experiments conducted by (Handin & Hager, 1957) to Barns Sandstone (left), while the right figure shows the same kind of plot from the Bad Bentheim sandstone experiments conducted in this research. This figure validates the hypothesis that

[26] Source: http://www.marmicarrara.it/uk/marble/bianco-cararra-c-lorano.asp
[27] Source of the pic: (Handin & Hager, 1957)

increasing the confining pressure will lead to increasing Young's modulus. The steeper the curve indicates the higher the Young's modulus. While for the Indiana LS, the curve in Figure 27 (left), shows that the Young's modulus does not always increase with the increasing confining pressure, which is contradictory to the hypothesis. It might be related to the Indiana limestone's property which is a very porous rock, and a lot of deformation can be happen without failing the rock, even in the elastic regime the material behaves more ductile as the confining pressure is increased, this makes the Young's modulus could be lower.

According to (Fossen, 2010) and (Handin & Hager, 1957), the increasing confining pressure increases the ductility of the material, which leads to longer ductile behavior and higher strength, makes the material more difficult to fail. This hypothesis is confirmed by the results of this experiment that was conducted on cylinders Bad Bentheim sandstone and Indiana LS.

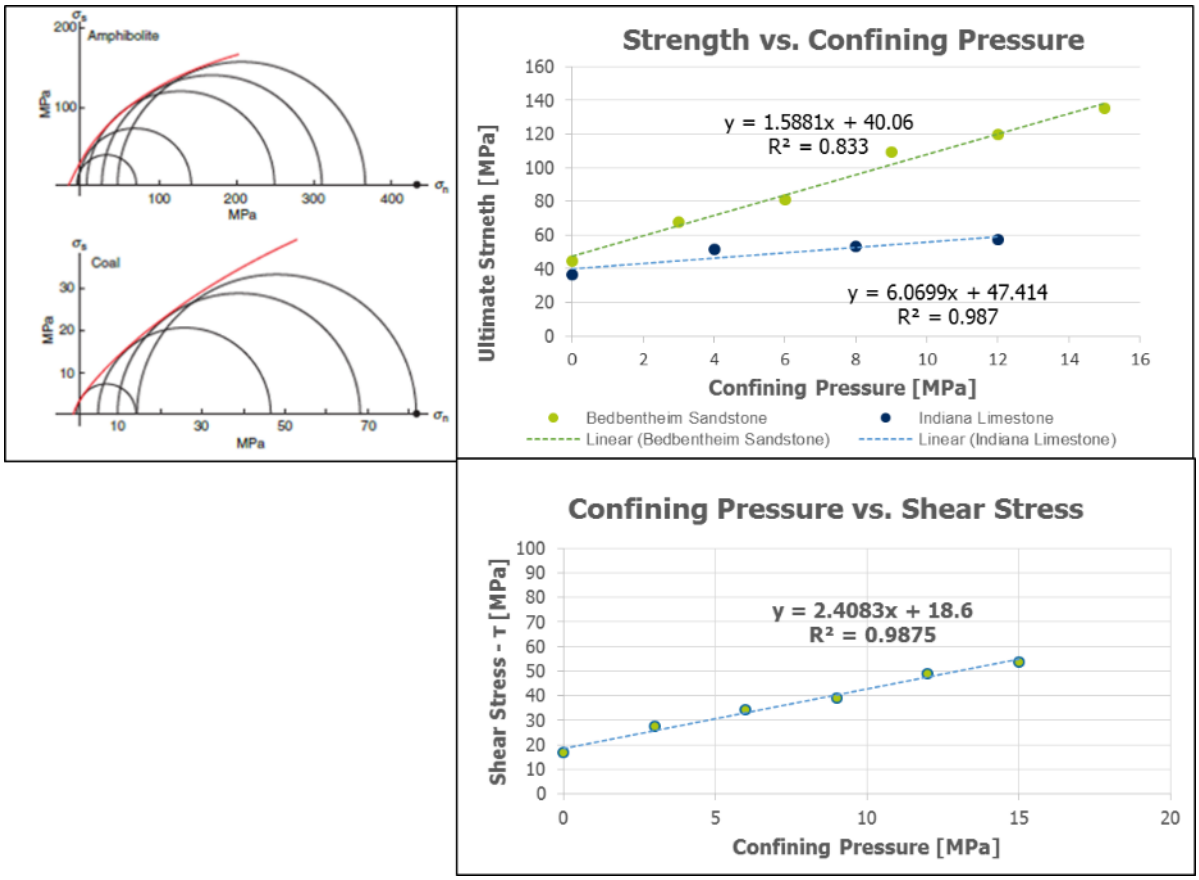

Figure 48. The results of Experiments by Fossen (2010) (left), and the result of this thesis (right).

Figure 48 on the left side shows the triaxial test results of (Fossen, 2010). It implies that the higher the confining pressure, the stronger the rock becomes (note that the red line is the failure envelope). On the right side is the result of bed bentheim sandstone and Indiana limestone experiments of this thesis. It also depicts that as the confining pressure is increasing the strenght and shear stress also increase. The high value of coefficient determinations suggests that the equations of the trend line can provide an estimation of ultimate strength from the determined confining pressure, especially for the BB Sandstone.

4.2. WMF Characteristic

In this section, the result of experiments from WMF characteristic will be discussed and compared with other promising shales to investigate the prospectively of WMF shales.

4.2.1.1 Petrophysics - Porosity and matrix density measurements

(Lie-A-Fat, 2014) showed that the matrix density in the upper section is more clustered compared to the upper part. The more scattered data in the lower WS part, might be related to the fact suggested by (Houben, et al., 2015, under review) which stated that the lower part of WMF is more layered and rich in laminations compared to the upper part. But giving more data from different section height, the comprehensive data in this thesis shows that the distribution of the matrix density does not differ a lot between upper and lower part of WS, even though the lower part spreads more than the upper part. It shows different characteristics can be observed when more data are collected to cover the WMF section. Please see Figure 49 for illustration.

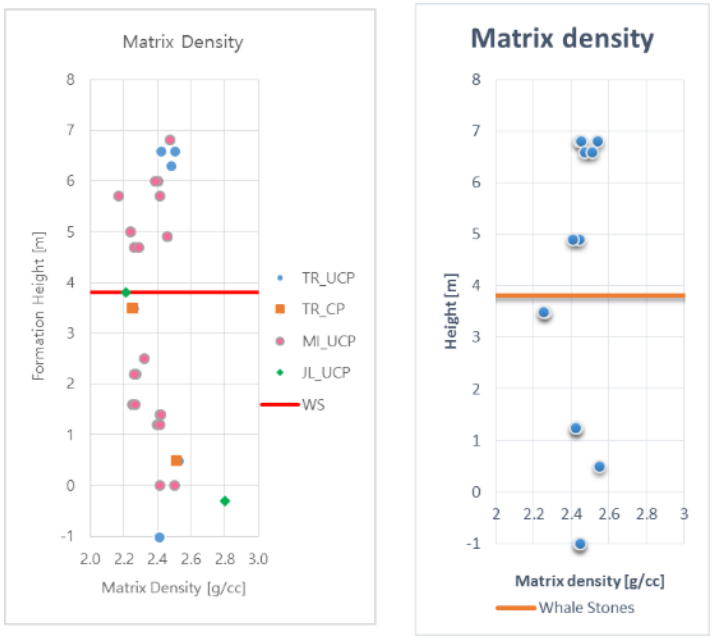

Figure 49. Matrix density from this research (left)[28], and from Fat (2014) result (right)

As mentioned in section 3.2.1, there is similar trend between matrix densities and S-wave velocities. Figure 50 shows that in general there is positive relationship between the two parameters. The low coefficient of determination (R^2) restricts the use of the linear relationship equation to predict the value of shear wave velocity based on the known matrix density.

[28] Source data: Thomas Ravenstein (blue and orange), J.L. Fat (green), Mutia Primarini (pink)

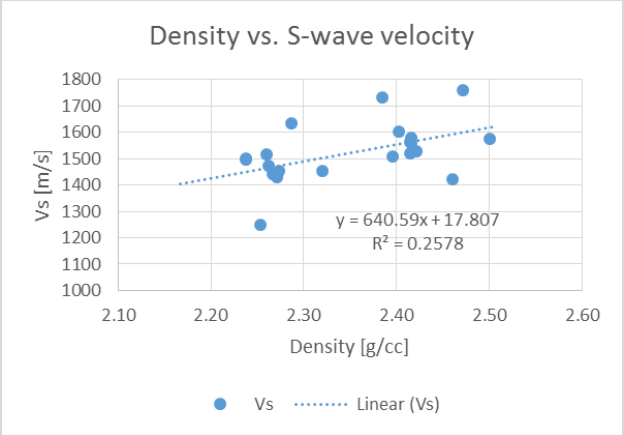

Figure 50. Cross-plot matrix density vs. S-wave velocity

To be able to identify the potential of WMF, the results of porosity and matrix density are compared to other shales as depicted in Figure 51

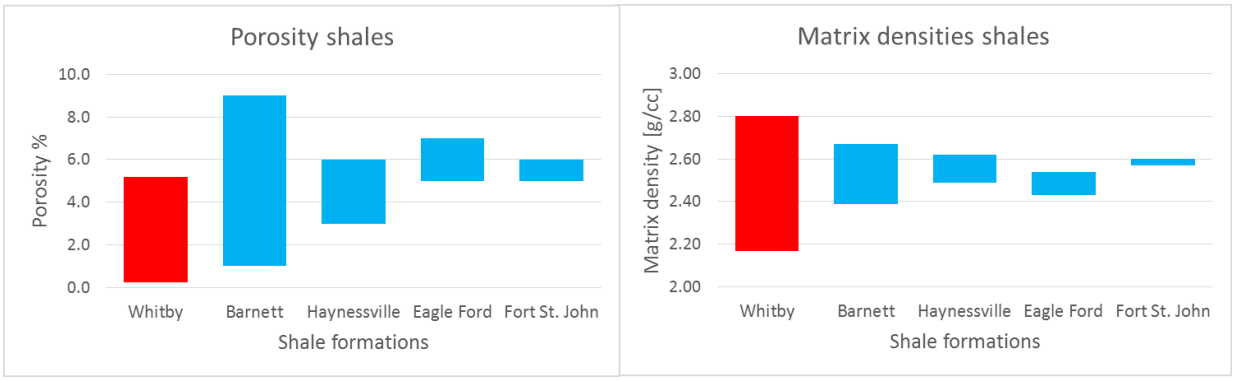

Figure 51. Porosity and matrix density of WMF compared to other shale.[29]

Figure 51 shows that the porosity range of WMF is in the lower side compared to the other shale formations. This might imply that the porosities of WMF are less promising. However, it is still in comparable to other shales. For the matrix density, the range is wider than other shale, it shows how high the variation and heterogeneity within the WMF section. This might suggest that the mineral composition also varies within the formation. Heterogeneity in reservoir is giving big impact to the fracture response (Maxwell & Norton, 2012), and yet it will complicate the hydraulic fracturing design, as it will be difficult to predict where and how the fracture will propagate.

4.2.2 Mineralogy – XRF Analysis

Mineralogy data becomes an important factor for shale tight gas production, where stimulation is required (Curtis, 2002). The mineralogy data of WMF are compared to proven shale like Barnett Shale displayed in ternary diagram in Figure 52 and Figure 53. Both figures show that Barnett shale has a big spread of mineralogy contents (carbonate, clay, quartz, and other minerals) compared to WMF. (Altamar & Marfurt, 2014) did a mineralogy analysis on Barnett shale formation using log data, and the results show that zones with high quartz and calcite content are more brittle than the regions with high

[29] Other shale information are from (Sone & Zoback, 2013)

clay contents. WMF mineralogy shows high content of clays and low contents of quartz and calcite compared to Barnett shale, indicating that it is less brittle, which could imply that the WMF in general are not favorable for hydraulic fracturing.

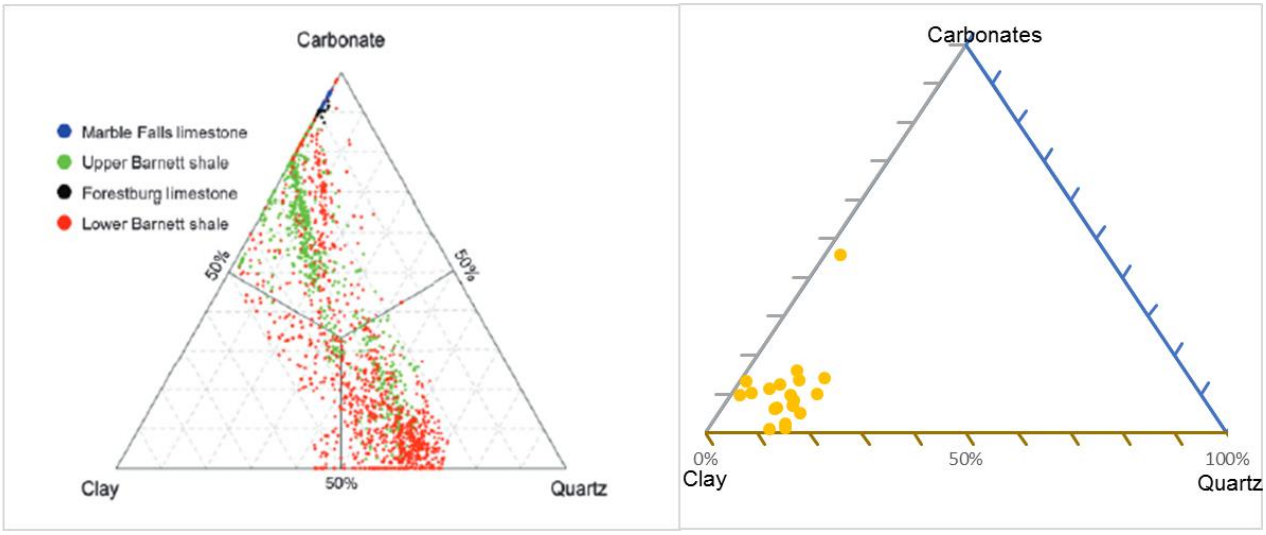

Figure 52. Ternary mineralogy distribution plot for clay, carbonate, and quartz for Barnett Shales, Rorestburg LS, and Marble Falls LS (Left)[30], and WMF (Right).

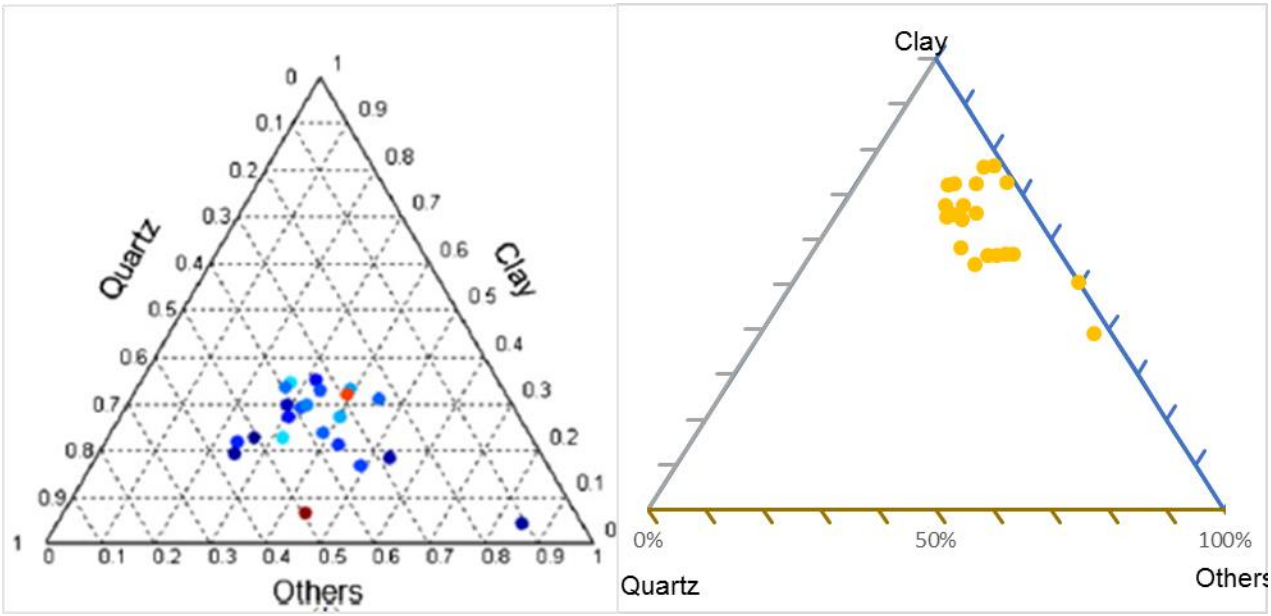

Figure 53. Ternary mineralogy distribution plot for clay, quartz, and other minerals for Barnett Shales (Left)[31], and WMF (Right).

[30] The plot is taken from (Altamar & Marfurt, 2014)
[31] The plot on the left is taken from (Zhiqi, et al., 2013)

4.2.3 Elastic Moduli

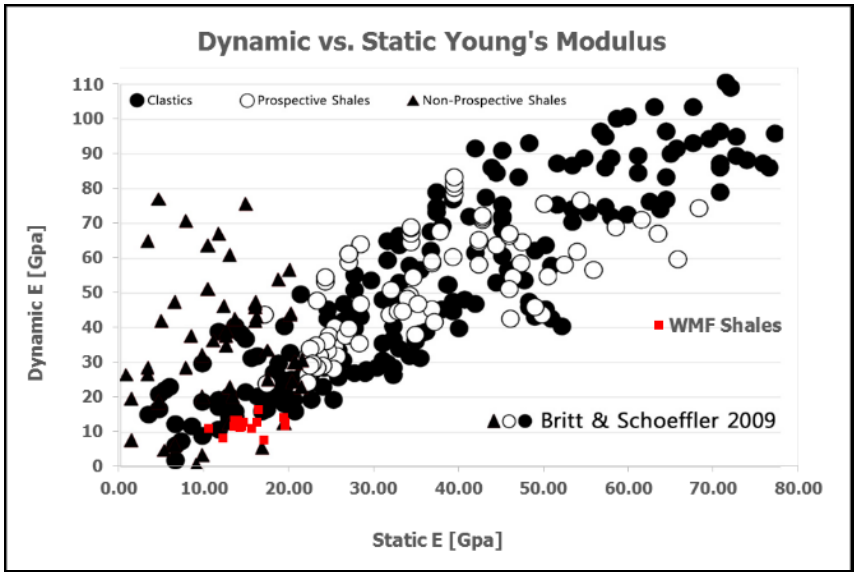

Figure 54. Dynamic vs. Static E of this study compared to (Britt & Schoeffler, 2009)

In Figure 54, the dynamic versus static Young's modulus data from this research are compared to data taken by (Britt & Schoeffler, 2009). His data points contained measurements from American shales of Mid-Continent South Texas and the Haynesville shales formation found in East-Texas and Northern Louisiana, and clastic rocks.

Figure 54 depicts that the WMF shale data corresponds with the clastic data. (Britt & Schoeffler, 2009) mentioned that the prospective shales have the tendency to fit in the dynamic-to-static clastic correlations of Young's modulus, which suggest that the WMF data might be categorize as prospective shale. However, all of the WMF data only fit in the beginning of the plot, the low value of E (both static and dynamic) stops them to further follow the trend of prospective shales. As most of the prospective shales have E value bigger than 20 GPa, while most of the WMF have E value less than 20 GPa, this makes the prospectively of WMF is still questionable related to the Young's modulus.

4.2.4 Brittlenes Index

(Rickman, et al., 2008; Zhiqi, et al., 2013) analyzed the data of Barnett shale and they came up with a theory that shales with higher Young's modulus and lower Poisson's ratio tend to be more brittle. In Figure 55, the results of (Rickman, et al., 2008) are compared with the result of this study.

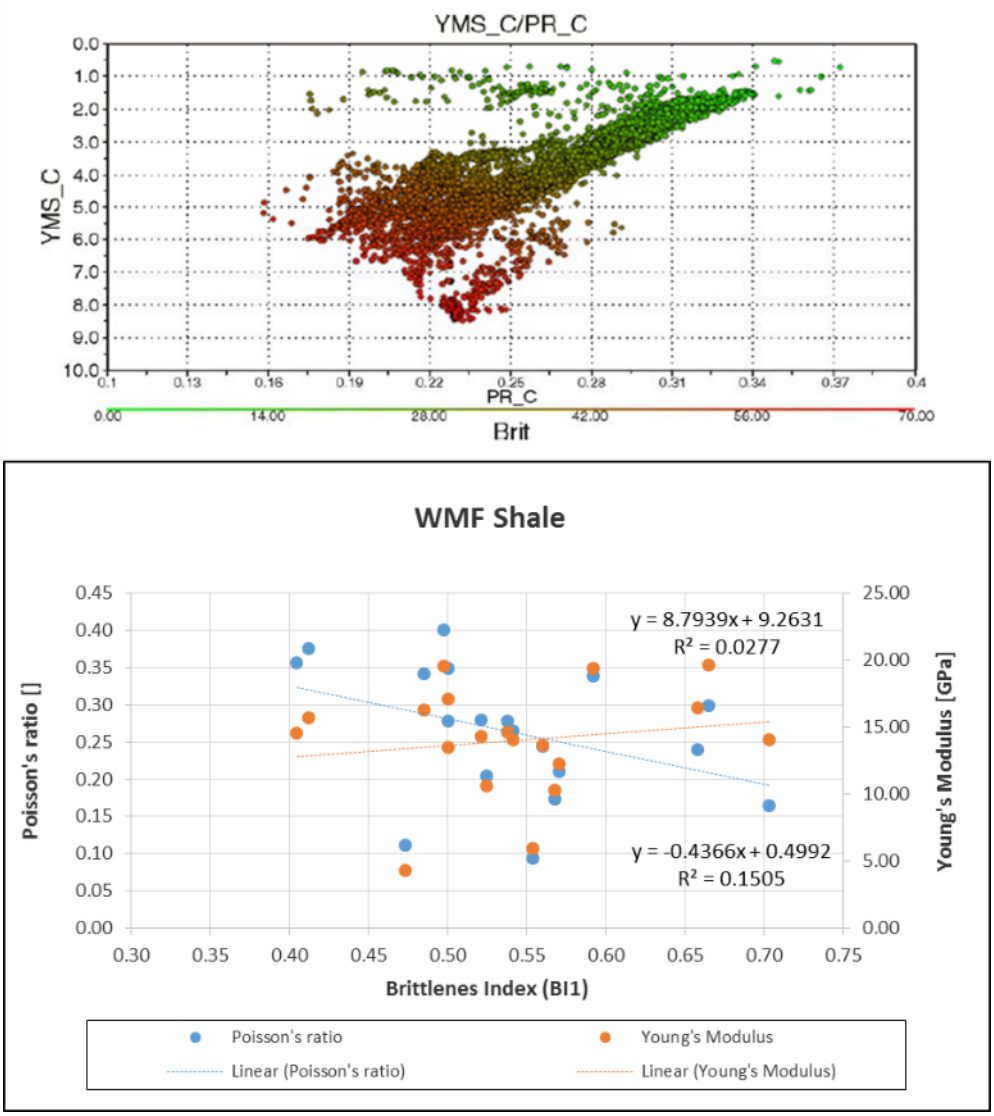

Figure 55. The relationship between elastic moduli and brittleness index (BI_1) of (Rickman, et al., 2008) (above), and this study[32] (below).

Figure 55 (upper part) depicts the positive correlation between brittleness index (BI_1) and Young's modulus, and negative correlation between Poisson's ratio and BI_1. The same trend is slightly found from this study, as depicted in Figure 55 (lower part). The very low coefficient of determination (R^2), 0.028 for Young's modulus and 0.15 for Poisson's ratio, shows that these relationships are not very representative or hold for the scattered data from WMF. From this explanation, one might suggest that WMF could be potential as it does follow the trend of Barnett shale brittleness index. BI_1 is relative to each data set, and the difference of BI_1 values between WMF and Barnett shale is mainly because of the different limit of E and v that has been used for the calculation as depicted in Table 10.

[32] The dataset for this study included 4 data points from (Ravenstein, 2014)

Table 10. The limits of E and v from this study and (Rickman, et al., 2008), with the output range of BI_1.

Study	Method	E (min - max)	v (min - max)	BI.1 min - max)
		Gpa	[]	[]
Rickman et al. (2008)	Log	0.5 - 8.5	0.15 - 0.38	0.00 - 0.70
This study	Unconfined test	4.3 - 19.66	0.09 - 0.40	0.40 - 0.70

In order to compare WMF's BI to other shale's BI, the BI must have the same limit. Therefore, it would be difficult for BI_1, as BI_1 is subjective to only that formation (different weight along the sample population). It is different with BI_2 and BI_3 which are not only within the height of interest. They are more universal, as they take into consideration the mineralogy and the strain (have same point of view/ comparable with other samples). Hence BI_2 and BI_3 are more comparable to other shales. Unfortunately, we have not found any data of BI_2 and BI_3 from other shales to be compared with the results of this thesis. (Yang, et al., 2013) analyzed the brittleness indices of Barnett shale included BI_2 and BI_3, but the experiments were done under the confining pressure of 10 to 60 MPa, which are different with the conditions of this study.

4.2.5 Fraccability Index

To place WMF in a bigger picture, the FI result from this study will be compared with result from another study.

(Jin, et al., 2014) evaluated the fraccability of shale reservoirs using Barnett shale log data. He used three different BIs and 2 different FIs in his study. But only one brittleness index was a match with the brittleness index used in this paper, BI_1. Thus, the combination of BI_1 with fracture toughness ($FI_{1.1}$) and BI_1 with Young's modulus ($FI_{2.1}$) in this study are used to calculate the FI. This FI was then compared with FI from Jin's study. Figure 56 and Figure 57 shows the comparison of these fraccability indices.

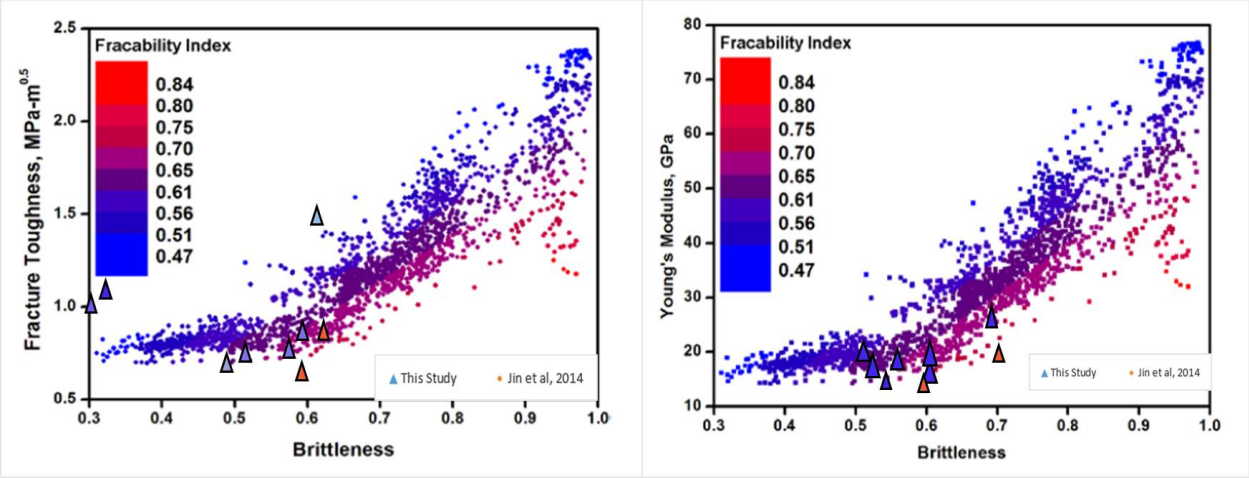

Figure 56. $FI_{1.1}$ from this study plotted on a cross-plot with data set from Barnett Shale (left), and $FI_{1.2}$ plotted with data from Barnett Shale (right) (modified from Jin et al.2014).

In Figure 56 the $FI_{1.1}$ and $FI_{1.2}$ from this study are plotted in the Barnett shale cross plot, the figure shows that Barnett shale and WMF shales has relatively the same trend of fraccability indices. In Figure 57 this phenomenon will be described further.

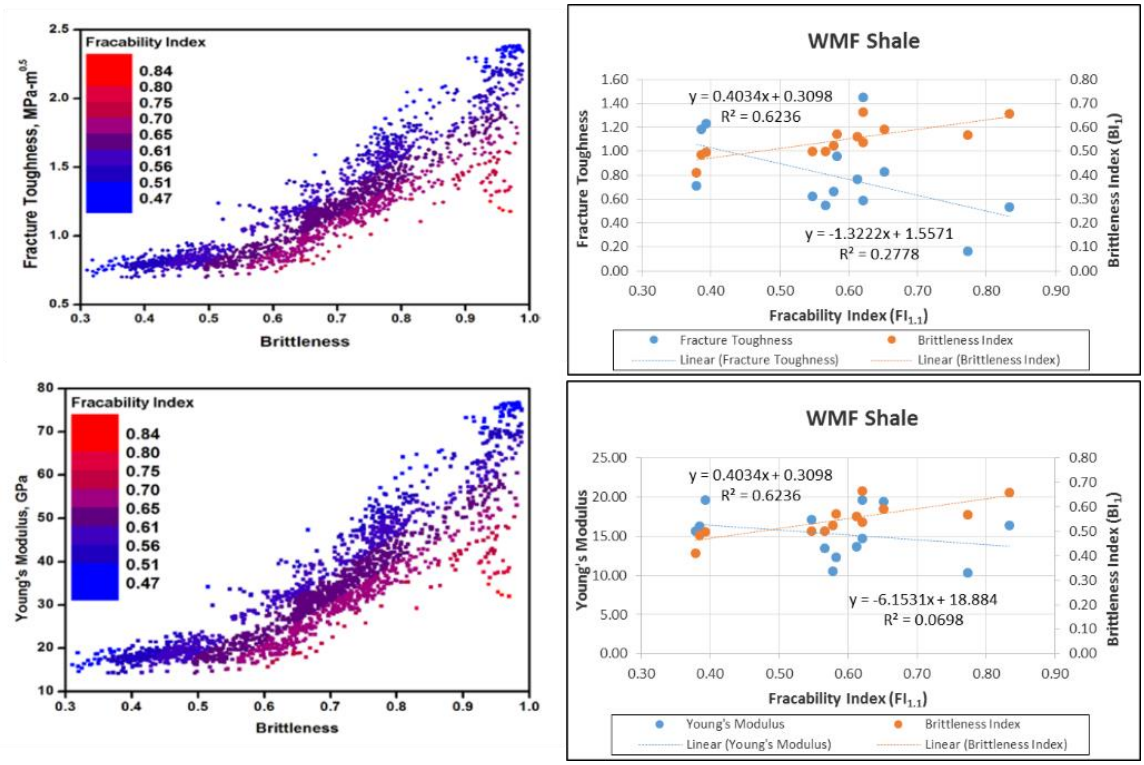

Figure 57. Comparison of Relationship between Fracture toughness and BI for $FI_{1.1}$ according to (Jin, et al., 2014) (upper left), and this study (upper right). And Comparison of Relationship between Young's Modulus and brittleness for $FI_{2.1}$ according to (Jin, et al., 2014) (lower left), and this study (lower right)

For $FI_{1.1}$ as shown in the upper plot of Figure 57, the result of (Jin, et al., 2014) study depicted that in form of Brittleness, the fraccability increases as the brittleness is increasing, and the lower the fracture toughness leads to the higher fraccability index. WMF shale plot on the upper right side shows the same correlation between fraccability index, brittleness index, and fracture toughness. The lower part of Figure 57 shows the same comparison, but for $FI_{2.1}$. WMF shale cross-plot shows that as the Young's modulus increases, the fraccability index decreases; and as the brittleness index increases, the fraccability index also increases. Considering that both FI using the same BI in the calculation (BI_1), the different parameters are Young's modulus and fracture toughness. The same trend between fracture toughness and Young's modulus in Figure 57 indicates that these two parameters can substitute each other when calculating the fraccability index. It also shows that formation with lower Young's modulus/fracture toughness will have a higher fraccability index which is favorable for hydraulic fracturing.

The parameter limit used for fraccability calculation in this study and (Jin, et al., 2014) study are depicted in Table 11, completed with their result of fraccability indices.

Table 11. Used limit parameters and the result of fraccability Index from this study and (Jin, et al., 2014) study.

Study	Method	E (min - max)	v (min - max)	BI.1 (min - max)	KIC (min - max)	FI 1.1 (min - max)	FI 2.1 (min - max)
		Gpa	[]	[]	[Mpa/(m^0.5)]	[]	[]
Jin et al.(2014)	Log	12.0 - 78.0		0.30 - 1.00	0.70 - 2.40	0.47 - 0.84	0.47 - 0.84
This study	Unconfined test	4.3 - 19.66	0.09 - 0.40	0.40 - 0.70	0.17 - 2.2	0.38 - 0.83	0.14 - 0.70

The value of fraccability indices from (Jin, et al., 2014) is not comparable to the FI from this study because the discrepancy between these results is caused by the different limit used in the studies. (Ravenstein, 2014) did sensitivity analysis on the parameter limits (E_{min}, E_{max}, v_{min}, v_{max}, $K_{IC\,min}$, $K_{IC\,max}$) for $FI_{1.1}$ and found out that by changing the parameter limit, the results will shift significantly.

4.2.6 The Potential of WMF and The Most Promising Horizon

The discussed result of WMF characteristic will be combined in this section in order to get an overview of the overall characteristics of WMF shale from this study. Based on these results, the most potential horizon for future gas exploration within WMF is determined. To get more representative data for the WMF, this study involved minimum 13 data points from different height for each characteristic. Additional data from previous related experiments (Lie-A-Fat, 2014; Ravenstein, 2014), were processed further to be added to the plot to reduce the uncertainty in the interpolations between these points.

(Britt & Schoeffler, 2009) mentioned that a prospective shale in general: (1) is made up of mostly silica and carbonate, with a few clay contains; (2) tends to be brittle and follows the clastic correlation of the dynamic to static young's modulus; (3) behaves isotropic in a core scale (not many laminations evident; (4) has Young's modulus bigger than 20.68 GPa; (5) has mineralogy composition that contains of not more than 40% clay. Referring to Figure 38, WMF shale also follows the clastic correlation of the dynamic and static Young's modulus. But unlike the prospective shale, WMF is highly anisotropic with seismic anisotropy up to around 30% and a lot lamination/ layering in the core scale. WMF shale in this study also has clay contents around 62%, which deviate from the prospective shale, and the Young's modulus ranges between 4.31 and 19.66 GPa, putting WMF in the lower range of the prospective shale. Prospective shale is expected to have a cumulative total organic content (TOC-FT) >30, gas content of 40 scf/ton, and a thickness > 30ft (Rickman, et al., 2008). But due to the unavailability of TOC data from this study, we cannot investigate the propectivity of WMF using his method.

Related to the prospectivity of the WMF shale, Table 12 gave an overview of the MWF characteristics investigated in this research, and compared it with the criteria value of the Prospective Shale.

Table 12.WMF shale prospectivity compared to other prospective shale. Postive (+) means the WMF is prospective according to the parameter, and negative (-) is not.

Literature	Parameter	WMF	Prospective Shale	Conclusion
(Britt and Schoeffer, 2009)	Young's modulus	4.31 - 19.66 Gpa	> 20 Gpa	-
	Trend Dinamic- Static YM	Follow clastic trend	Follow clastic trend	+
	Layering	not many in a core scale	A lot of laminations	-
	Anisotropy	Anysotropy up to 30%	Behave isotropic in core scale	-
	Clay Content	39 - 72%	< 40%	-
(Bruner & Smosna, 2011)	Quartz Content	2.95 - 16.5 %	10% - 60%	+
(Rickman et.al, 2008)	TOC-FT	N/A	>30	N/A
	Gas Content	N/A	40 scf/ton	N/A
	Thickness	>30ft	>30 ft	+
(Sone & Zoback, 2013)	Porosity	0.3% - 5.2 %	1% - 9%	+
	Density	2.17 - 2.8 g/cc	2.38 - 2.68 g/cc	-

From Table 12 we cannot draw a solid conclusion about the prospectivity of WMF. Some of the characteristics show that WMF is promising, and some others show otherwise. Thus, it is still in doubt whether WMF is promising for future shale gas exploration or not. But one thing for sure, WMF is not equivalent to the Barnett or Lafayette shale.

Figure 58 depicts the determined results of this study, along with the height section, to see if there is any trend toward WS, or any relation with the height. Based on the data trend, the height section is divided into 4 parts, to make it easier for the analysis to determine the most promising zone (Figure 59).

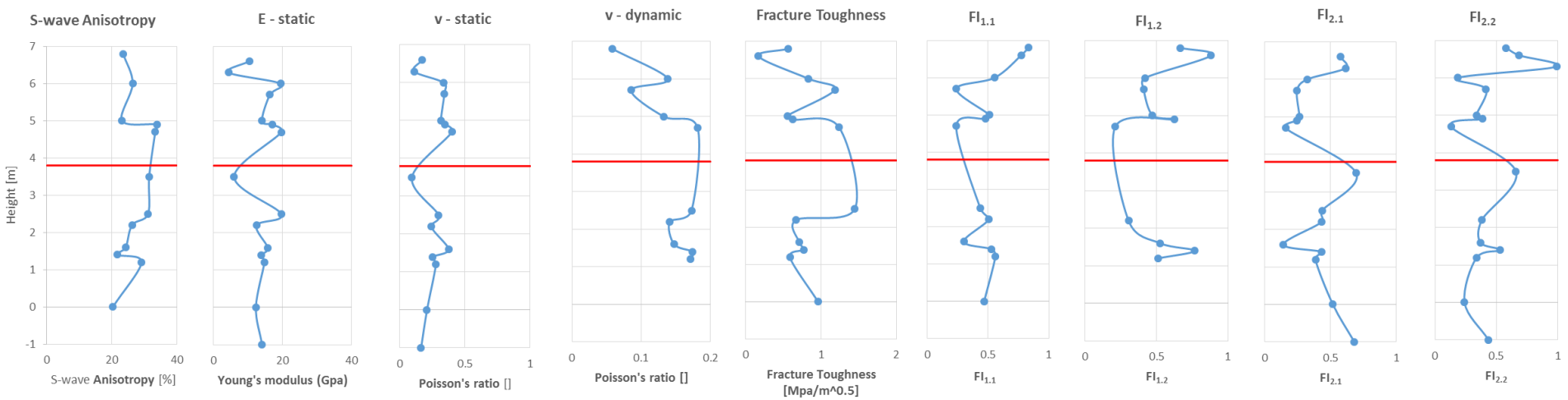

Figure 58. Some determined characteristics with trend towards the WS (red line)[33]

As fracture toughness increases, the fraccability indices (FI1.1 and FI1.2) are predicted to decreases, and as Young's modulus decreases toward the WS, the fraccability indices ($FI_{2.1}$ and $FI_{2.2}$) are expected to decrease as well. Figure 58 satisfies this expectation. For the fracture toughness, as Young's modulus decreases, fracture toughness should be decrease as well. This trend is visible in Figure 58, except for the section height between 3 – 4 m, this might be caused by the lack of data point in the fracture toughness. A clear explanation on the correlations between all of the characteristic are still questionable.

[33] Some values are modified from (Ravenstein, 2014; Lie-A-Fat, 2014)

In Figure 59, some characteristics to determine the most potential horizon for hydraulic fracturing and future gas reservoir are plotted.

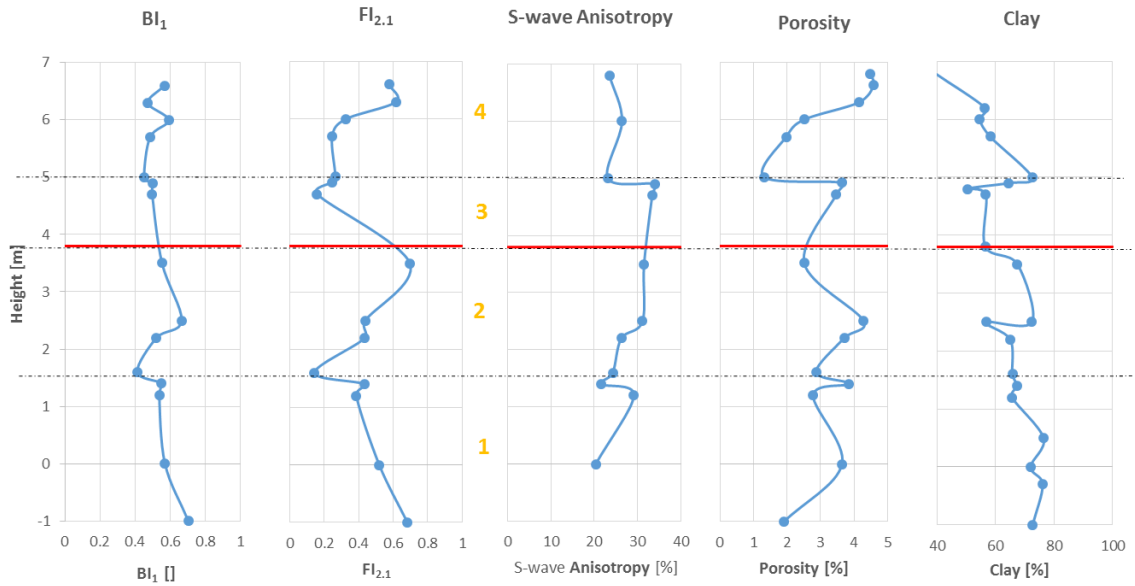

Figure 59. Determined characteristics to evaluate the potential horizon within WMF

As previously mentioned, all of the BI and FI show the same trend in general, thus only one brittleness index and one fraccability index are presented in Figure 59. The BI and FI with the most data points covered the height section between WMF are chosen. None of the zone, from 1 to 4, seems to be favorable for all the characteristics. Lower part of zone 1 is more favorable if we look at the high brittleness index and high fraccability index in that zone. S-wave anisotropy also shows lower value in that zone. But the porosity shows a small value as well, which makes the conclusion become vague. From the porosity point of view, the most favorable section will be the upper part of zone 4, which fortunately has fairly good value of BI and FI, even though not the highest compared to other zones. The S-wave anisotropy and clay contents also show small value in the upper part zone 4. (Ravenstein, 2014) mentioned that the most promising horizon for hydraulic fracturing are the most lower part and upper parts of the WMF. His results correspond with the results of this study. If we incorporate the pyrite contents, zone 3 and the upper part of zone 2 which has highest average pyrite contents might also be favorable, as suggested by (Zijp, et al., 2014) that mentioned about the positive correlation between pyrite contents and TOC.

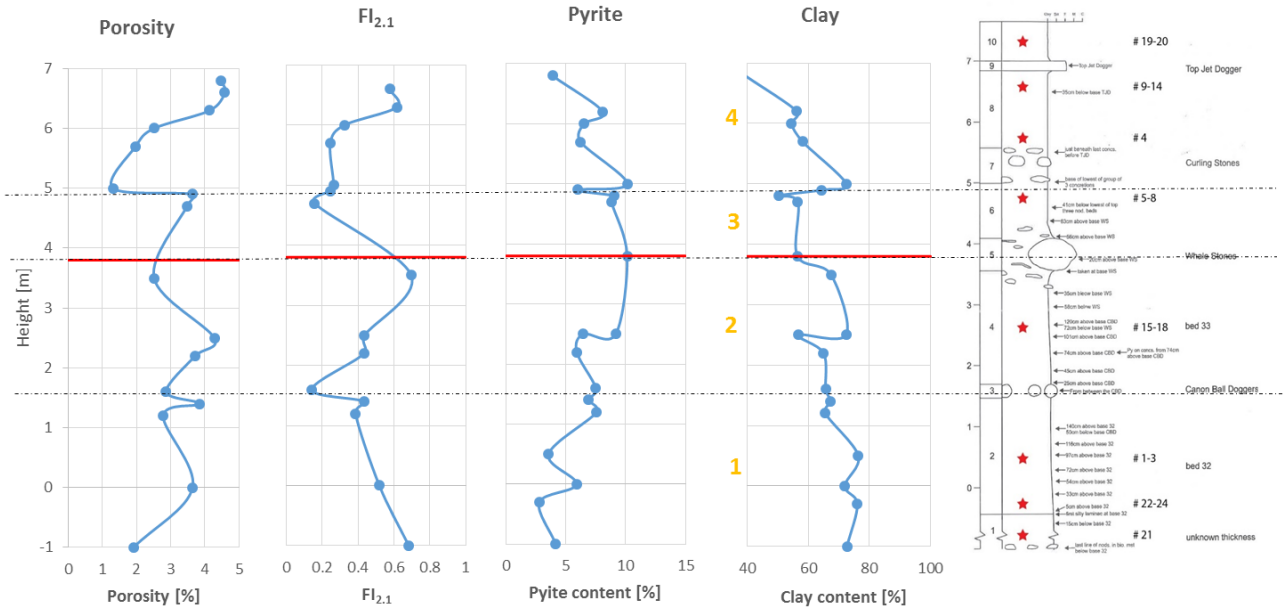

Figure 60. WMF Zone section based on the results of this study compared to stratigraphic column of WMF by Linde van Laerhoven's (TNO)[34]

Figure 60 shows the zone section of WMF based on the results of this study, as in Figure 59, but this one is compared to the stratigraphic column made by Linde van Laerhoven (TNO). It shows that the zonation is almost the same. The first boundary lays in the Canon Ball Doggers, the second is at the Whale Stones, and the third one is slightly below the Curling Stones.

(Yang, et al., 2013) mentioned about the role of ductile formation as a fracture barrier in the hydraulic fracturing treatment. Looking at the BI and FI values, the border between zone 1 and zone 2 could acts as a barrier on the hydraulic fracturing treatment, which prevents the fracture to grow vertically.

[34] The graph on the most right is modified from Linde van Laerhoven (TNO)

4.3. Brittleness Indices Analysis

To check the relationship between different brittleness indices and the elastic modulus, cross-plots are generated in Figure 61 and Figure 62.

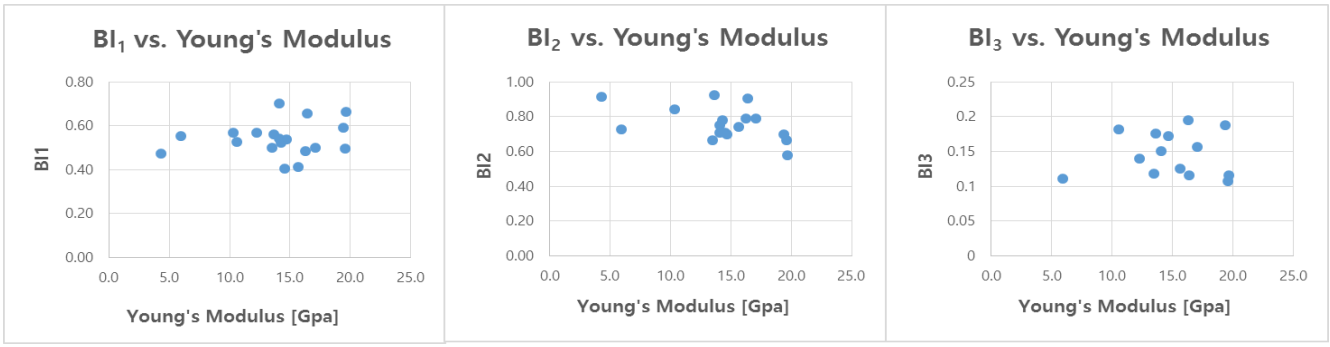

Figure 61. Brittlenes Indices vs. Young's modulus

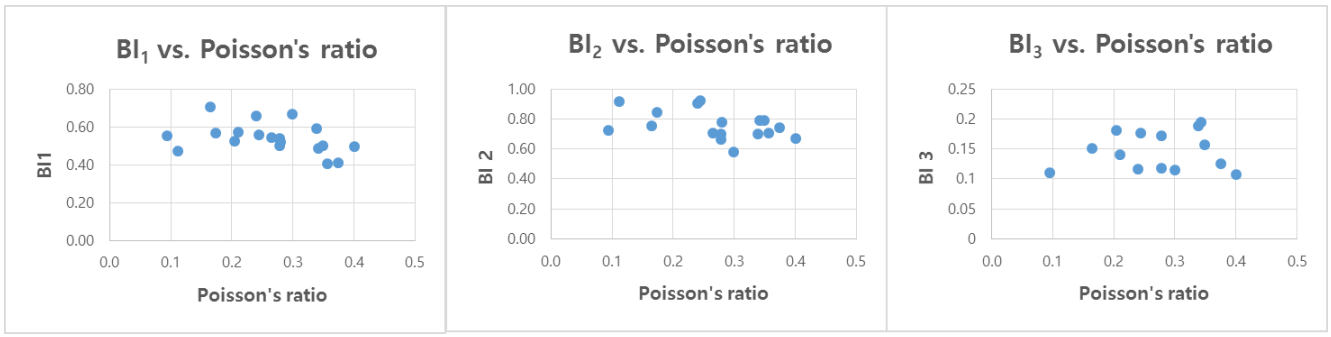

Figure 62. Brittleness Indices vs. Poisson's ratio

It is expected that BI_1 will correlate to Young's modulus and Poisson's ratio, compared to the other BI, as BI_1 was derived from the averaging value of elastic modulus. But this experiment results show that all brittleness indices have weak correlation with the elastic moduli. There is a weak trend between BI_2 and the elastic moduli, indicates that rock with higher Young's modulus and higher Poisson's ratio tends to bear more elastic strain before failure. BI_3 has a weak correlation with the Young's modulus and Poisson's ratio, which indicates that these Brittleness Indices do not correlate with the elastic properties of the rock.

(Yang, et al., 2013) mentioned that the rock strength was considered as one of the indicators of rock's brittleness. To check the validity of his statement toward this research, cross-plots between Brittleness Indices and rock strength are made in Figure 63.

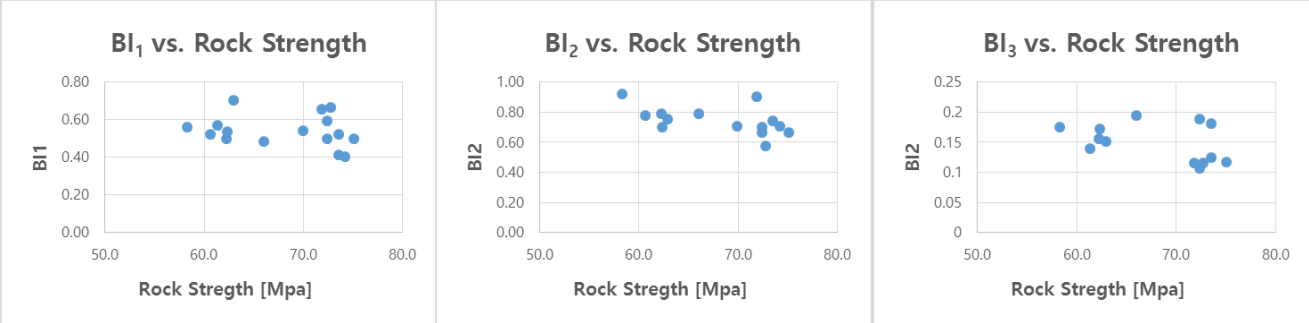

Figure 63. Brittleness indices vs. Rock strength

Surprisingly, the brittleness indices calculated in this research do not show strong correlation with the rock strength. It is expected that BI_1 will correlate with the rock strength, since in general rock strength follows the same trend as elastic moduli, as depicted in Figure 27 and postulated by (Yang, et al., 2013). In this study as the correlation between elastic moduli and BI_1 is weak, the similar correlation also applies for the elastic moduli and rock strength.

BI_3 relates BI and mineralogy, based on the observations that associate the best producing wells within Bernett shale with higher quartz content (Jarvie, et al., 2007). From Figure 64, the relationship between different brittleness indices and clay content can be observed.

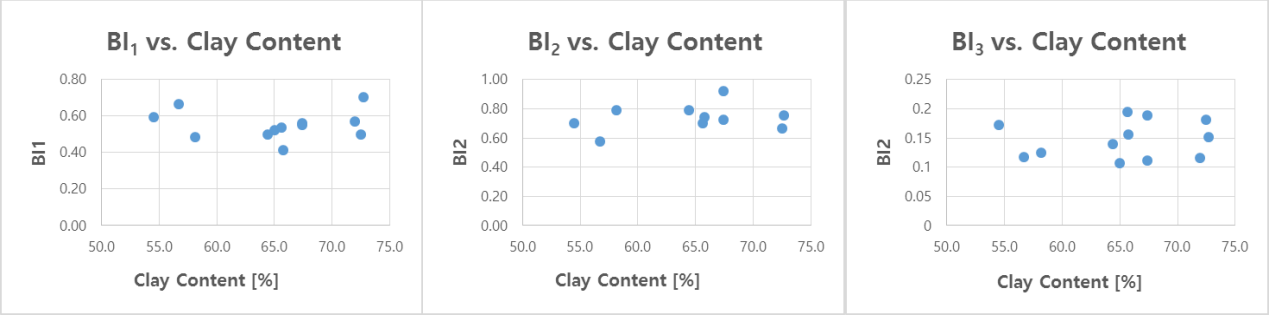

Figure 64.Brittleness indices vs. Clay Content

Minerals such as quartz are very brittle, while clay is more ductile. So it is expected that there will be correlation between clay content and BI, especially for BI_3, as it is calculated based on the quartz and clay content. However, brittleness indices calculated in this study do not show strong relationship with the clay content. Even for BI_3, sample with higher clay content can have the same brittleness index as the sample with lower clay content. This is due to the ratio of quartz, clay, and calcite of those samples. For example, a sample could have higher clay content, but the ratio of Q: (Q+C+Cl)[35] is still higher than those with lower clay content, thus it would still have higher BI.

Each brittleness index in this study are narrow in variation, they seems to be clustered and separate from each other. BI_1 range from 0.21 – 0.85, BI_2 range from 0.58 to 0.92, and BI_3 varies from 0.11 to 0.19. Thus, it is difficult to make a decent cross-plot which shows the relation between brittleness index and rock properties.

[35] $BI_3 = \frac{Q}{Q+C+Cl}$ (Jarvie, et al., 2007)

To investigate the consistency between one BI to another BI, cross-plots are generated in Figure 65.

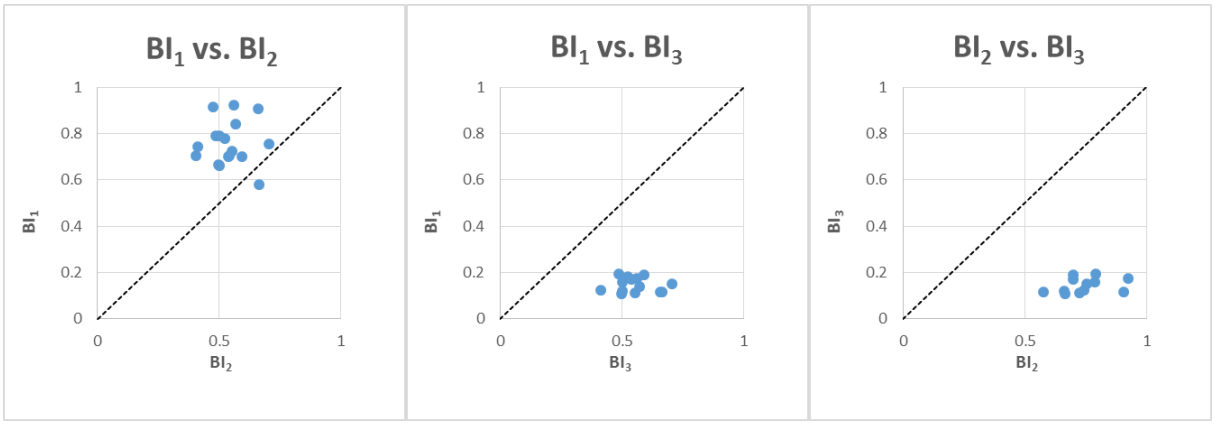

Figure 65. Comparison between various brittleness indices calculated in this study

The comparison between brittleness indices calculated in this study shows that even the BIs are determined from the same sample (same laboratory data), they do not yield a consistent brittle behavior. (Yang, et al., 2013) studied on comparing various brittleness indices in organic-rich shale, concluded that in general they do not follow a consistent trend.

Brittleness indices calculated in this study have different values and ranges. They also show different correlation with the rock properties, for example BI_1 shows correlation with the elastic moduli, but this is not applied for BI_2. Different characteristics from a rock are represented by these brittleness indices. For example BI_1 defines brittleness as combination of elastic moduli information, and BI_3 represents the quartz content of a rock. Because of this differences and interpretation of brittleness index, it cannot be relied as a single factor to predict the potential of hydraulic fracturing initiation and propagation in shale. Other factors such as the presence of natural fracture, *in situ* stress condition, mineralogy composition, and elastic moduli, together also give influence on the hydraulic fracturing performances (Yang, et al., 2013).

4.4. Static vs. Dynamic Elastic Moduli

Numerous experiments show that dynamic Young's modulus are greater than the static (Machinsky, 2003; Martinez, et al., 2011). This is due to the viscoelastic effect and the strain in dynamic that is lower than static. (Britt & Schoeffler, 2009) conducted experiments with some American shales of Mid-continent, South Texas and the Haynesville Shale formation, and (Ciccotti & Mulargia, 2004) did experiments in typical seismogenic rock. Both of the studies also included some data points where the dynamic elastic moduli are lower than static moduli, as depicted in this study.

The lower static moduli is possibly related to the heterogeneity and the anisotropy of shales, as WMF shales have high anisotropy and heterogeneity within its section. This makes the characteristics different with other rocks, especially the homogeneous isotropic rock like sandstone and limestone. (Ravenstein, 2014) experimented with WMF in different layer direction, and found out that the fracture mostly forms along the layer (parallel to the bedding). He also found out that the Poisson's ratio is larger in horizontal bedding. This research used the samples of WMF which has horizontal bedding, thus it has the tendency

to have a bigger $\varepsilon_{horizontal}$ than the $\varepsilon_{vertical}$. In the dynamic moduli, the ratio between $\varepsilon_{horizontal}$ and $\varepsilon_{vertical}$ is smaller as there is no stress applied to the sample. This might become the reason for the result of higher static Poisson's ratio than the dynamic- in this research.

4.5. Mineralogy Analysis

The mineralogy results in Section 3.2.2 show that WMF has high heterogeneity which will add more complexity and less favorable for hydraulic fracturing. Another revelation is that the high clay content of WMF (50-70%). (Houben, et al., 2015, under review) utilized XRD, XRF, and SEM (Scanning Electron Microscopy) measurements to analyze the WMF clay contents and the results show of 50-70% clay (using XRD-XRF method), and > 50% clay using SEM method. These results are consistent with the results of this study.

(Sone & Zoback, 2013) studied the static and dynamic elastic properties in Barnett, Haynesville, Eagle Ford, and Fort St, John Shales, and found out that the static Young's modulus decreases with clay content. The study also reveals that clay volume has positive correlation with the porosity as the pore volume mainly reside within the solid organics and/ or between the platy clay minerals in these shale gas rocks. To check whether these conditions hold for the WMF, cross-plots are generated in Figure 66.

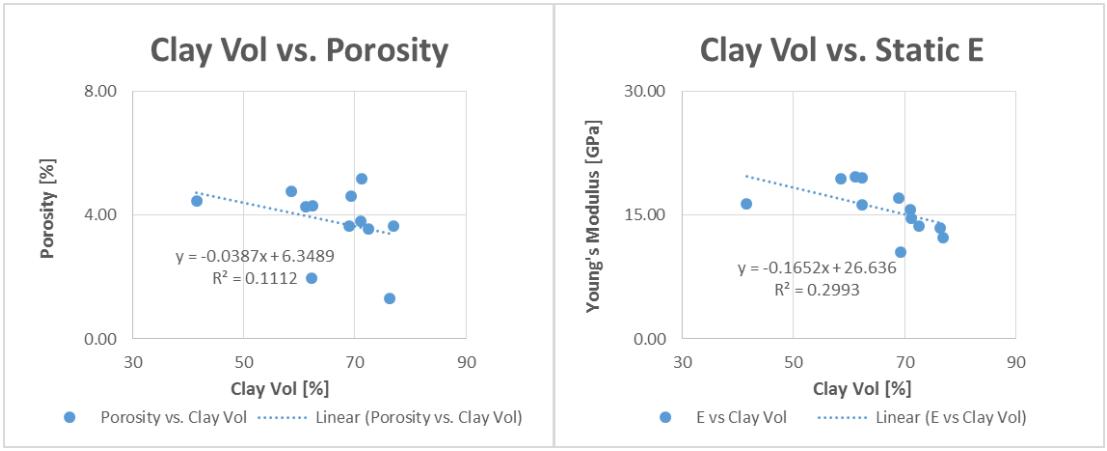

Figure 66. Cross-plot showing Clay Vol. vs. Porosity (Left), and Clay Vol. vs. Static Young's Modulus (Right).

Figure 66 confirms that, on the one hand, there is a negative correlation between clay volume and static Young's modulus (Right). On the other hand, the negative correlation between clay volume and porosity (Left) does not align with the result from (Sone & Zoback, 2013; Marion, et al., 1992) which stated that there is a positive correlation between clay volume and porosity. The negative relationship between clay volume and porosity indicates that the pore volume in WMF might not exist between the platy clay minerals. The very high laminations of WMF might have possibly caused this phenomenon.

To determine whether there is relationship between P-wave velocity and clay content, these two parameters are plotted against one another in Figure 67.

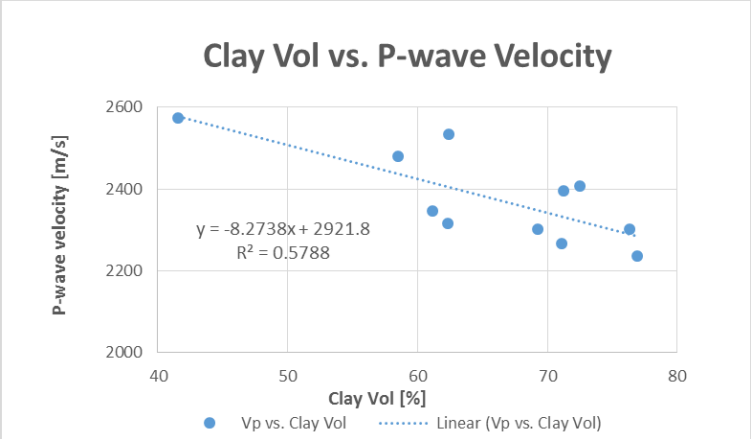

Figure 67. Cross-plot showing clay volume vs. P-wave Velocity

The P-wave velocity determined in this study decreases as clay volume increases. The low R^2 makes the relationship between these two parameters is not assumed to be representative, but in general one would know that there is negative correlation between clay volume and compressional velocity. (Marion, et al., 1992) measured velocity and porosity at various confining pressures and various sand-clay mixtures, and the result also showed that the clay content increases and the P-wave velocity decreases.

4.6. Fracture Characterization

The relation between geomechanic and the output from quantitative interpretation of WMF fracture will be presented and discussed further in this section.

The main observation from Figure 38 is that the Fracture length (L) has a positive correlation with the – width (w) and – aperture (d). As mentioned before, this conclusion did not match the results from (Olson, 2003) which stated that the aperture will have a scale of power 0.5 to the length ($D_{max} = x.L^{0.5}$), while this study shows a result of power 0.66. (Klimczak, et al., 2010) analyzed fractures in various outcrops and found out that the power law exponents vary between 0.2191 and 0.6195, which more or less correspond with the result of this study. (Ravenstein, 2014) did the same experiments in the same formations with this study. His result depicts a power law of 0.27. This discrepancy could be triggered by the fact that he used samples with various layer orientation, and applied the pressure several times in the same samples, while this study only uses sample that has horizontal layer, and each of the samples is only subjected to pressure once, until the rock fails or experiences fractures. Apart from it, this study also covers wider section height than his study.

The results of different studies are depicted in Figure 68.

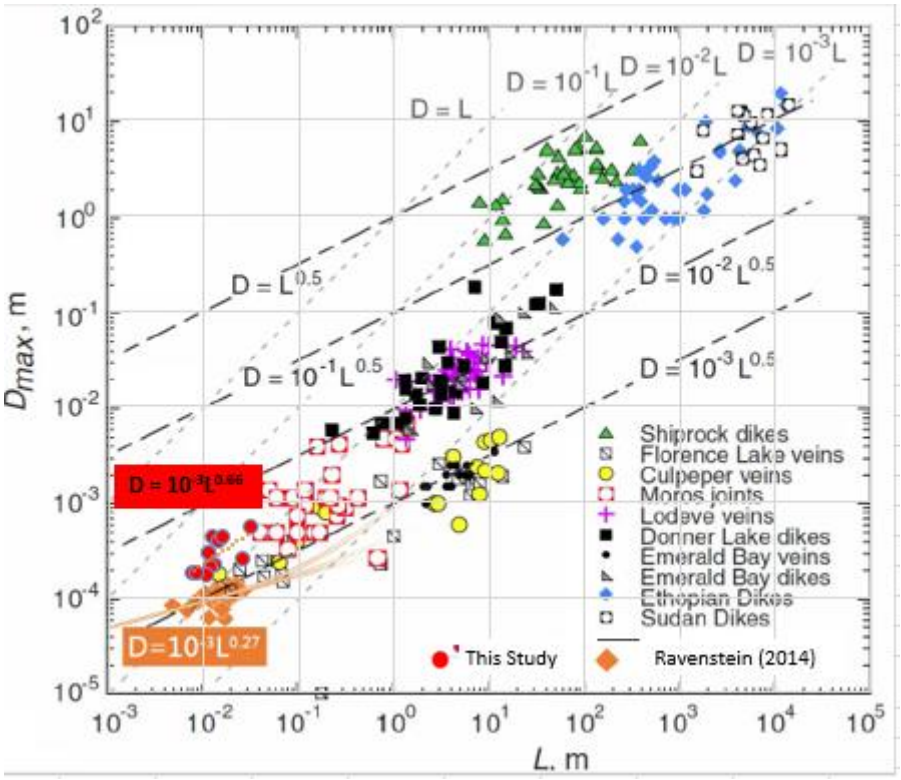

Figure 68. Cross-plot of the Length vs. Aperture from this study, (Ravenstein, 2014), and (Klimczak, et al., 2010)[36]

Figure 68 depicts that the results of this research fall in the lower side of the other dataset observed by (Klimczak, et al., 2010). It can be argued that the relationship of D_{max} – L behaves differently when the fractures are artificially created and have the aperture and length less than 1 mm and 10 cm respectively. As can be observed from the figure, using the same samples of WMF can lead to different result. This suggests that more data set with larger aperture and length needs to be tested to see whether this correlation is valid or not.

Other interesting thing to be discussed is about the relationship between the quantification (fracture length and aperture) and the geomechanical (strength and Young's modulus) – result. Figure 41 shows the relationship between strength, Young's modulus, and total fracture length. It depicts that the stronger the rock and the higher the Young's modulus, the longer the total fracture length created in a sample. If we combine with Figure 69 on the left side, a conclusion can be drawn that the higher the E of the samples, the more stress is required to create the first fracture, and the fractures created will be longer in total, while the aperture will become smaller. The energy (strength) dissipation was utilized to propagate the fracture and to create more length instead of increasing the aperture.

[36] The plot is modified from (Ravenstein, 2014)

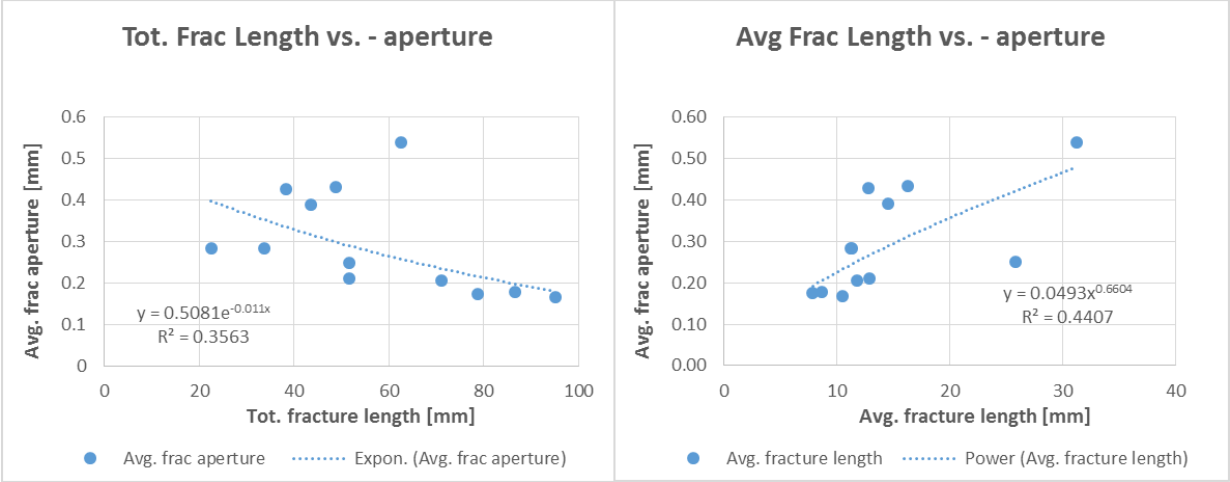

Figure 69. Cross-plot Tot. frac length vs. Avg. aperture (left), and Avg. fracture length vs. Avg. Aperture (right).

To have an idea of this relationship per sample, we used the total fracture length, but not the total aperture. If we imagine a canal, the length is in total, but the wide is average width. There is one point that seems to be the outliner in both graphs in Figure 69. This point belongs to sample 36A. Sample 36A seems to have few long fractures, > 30 mm, and wider aperture, >0.54 mm, but in total it has fracture length of 63 mm, shorter than other samples who have shorter average fracture length. It gives indication that this sample has less number of fractures. This argument is supported with the quantification result as showed in Figure 37.

The presence of long interconnected fracture is very important in tough gas reservoir. (Warpinski, et al., 2009) mentioned that interconnected fracture network of moderate conductivity with a relatively small spacing between fractures is required to obtain reasonable recovery factor in tight gas reservoir. Result of this study shows that the longest fractures are created in the upper part (above WS), referring to Appendix E.3.

To determine if there is a correlation between porosity and aperture, and porosity and length, these 3 parameters are plotted in Figure 70.

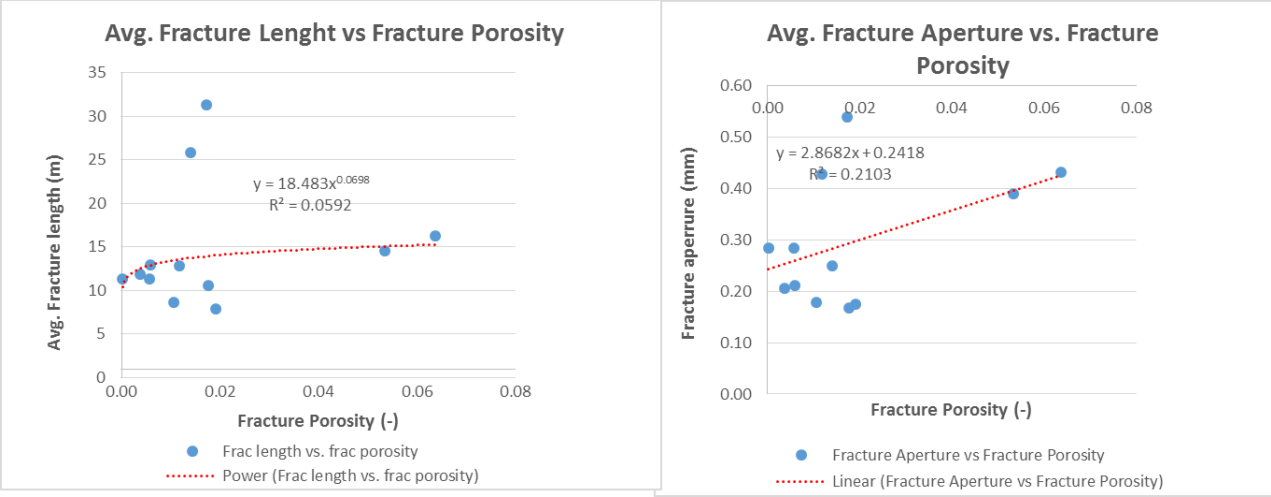

Figure 70. Cross-plots of Avg. fracture length vs. Fracture porosity (left), and Avg. fracture aperture vs. Fracture porosity (right)

Figure 70 on the left side shows that the porosity increases as the avg. fracture length increases. However, the very low coefficient of determination (R^2) and the scarcity of the dataset, suggested that the relationship between these two parameters is not assumed to be representative. At the other end, the figure on the right shows that with the increasing fracture aperture, the fracture porosity also increases. Looking at the coefficient of determination, the correlation between fracture aperture vs fracture porosity fit better than Avg. fracture length vs. fracture porosity, with the value of 0.2 compared to 0.06 respectively. The trend is also more visible. (Ravenstein, 2014) also suggested that compared to average fracture length, aperture plays more dominant role in determining the trend of porosity.

4.7. Fracture Toughness

In this section the result of fracture toughness as the combined result of quantitative fracture characteristic and geomechanical properties will be discussed further.

Figure 42 depicts the fracture toughness along the WMF height section, and indicates that the Young's modulus is the dominant factor controlling the fracture toughness. To investigate the validity of this statement, a cross plot between Young's modulus (E) and fracture toughness (K_{IC}) is created in Figure 71, together with the other factors controlling the fracture toughness, namely Average fracture length (L), average aperture (d_{max}), and Poisson's ratio (v).

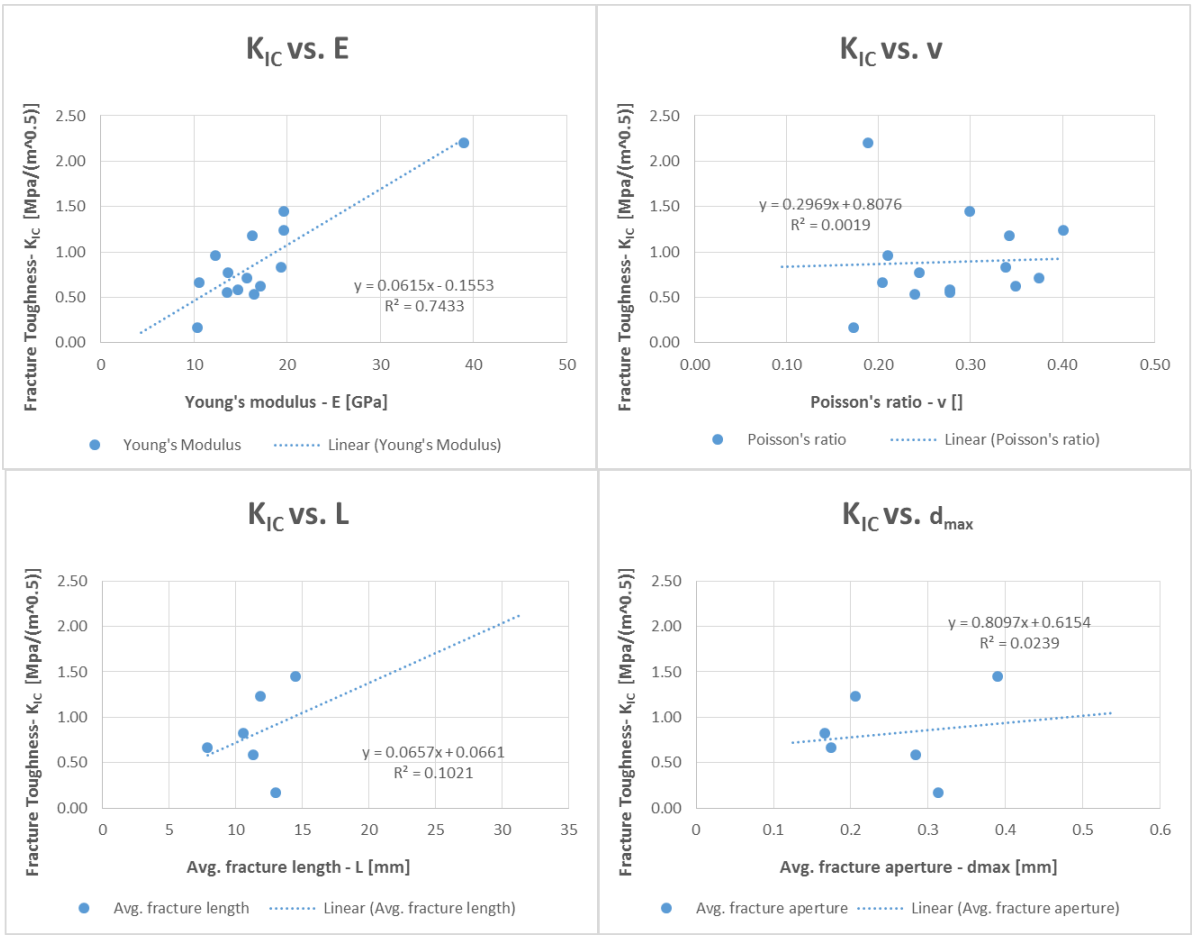

Figure 71. Cross - plots between Fracture toughness and all factors that controlling fracture toughness.

In Figure 71, all factors controlling the K_{IC} are plotted against the K_{IC}, and the results show that the Young's modulus has higher coefficient of determination (R^2) compared to other factors. Based on this linear relationship, one might give an estimation of fracture toughness's from the known Young's modulus value. This also suggests that Young's modulus is the dominant factor controlling the K_{IC}, which corresponds with the previous data analysis in Chapter 3.2.4

4.8. Porosity, Anisotropy, and Velocity

In Section 3.2.1, the velocity results are presented but it is not explained whether there are correlations between velocity and other petrophysical parameter or not. (Lie-A-Fat, 2014) showed that there was a positive correlation between the porosity and velocity, with relatively low R^2 (0.03 and 0.1 for Vp and Vs respectively) and argued that this relationship should be enhanced with more data points. To prove her argument, this thesis uses more data points. The results are shown in Figure 72.

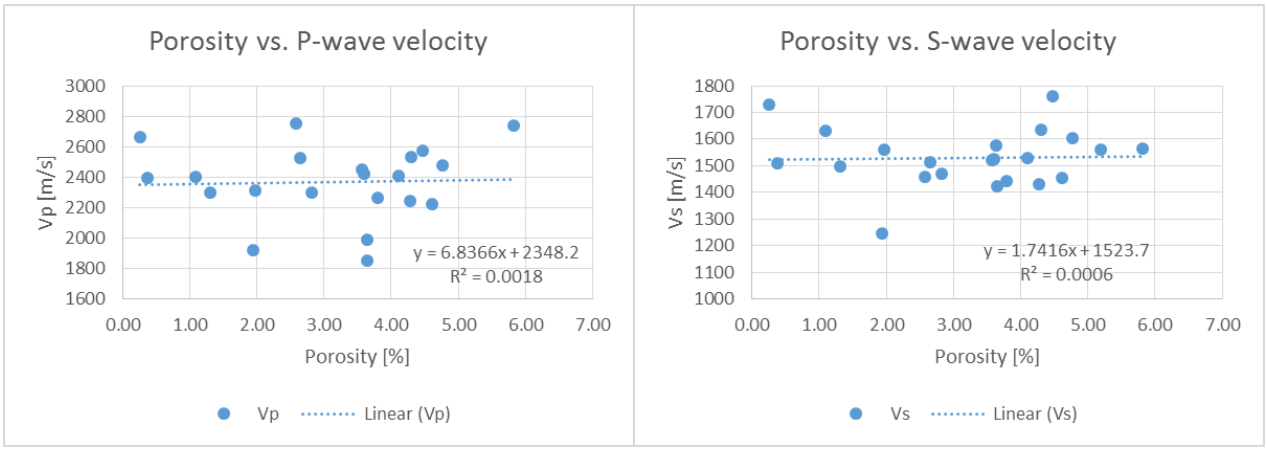

Figure 72. Cross-plot showing porosity vs. velocity[37]

Figure 72 shows that the positive correlation does not improve by adding the data points. The figure implies that velocity is slightly independent to the porosity. The discrepancy of this results might be because of the different limit on the porosity and Vp, Vs between the two researches.

The velocity anisotropy of WMF from this research shows that it does not correlate with the height (refer to Figure 33). This is interesting as some literatures stated that there is a correlation between height, stress, and velocity anisotropy, like what explained by (Jones & Christensen, 1981) that velocity anisotropy increased with burial depth, and this is related to the increasing density and stress (Sayers, 1999).

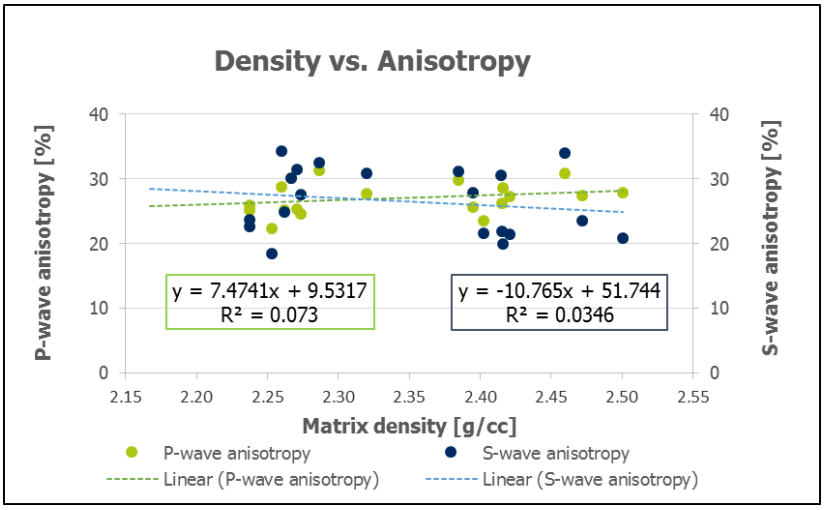

Figure 73. Density vs. Anisotropy

Figure 73 depicts that density is independent to anisotropy, especially for the S-wave, and it does not correspond with the depth. WMF shales anisotropy measurements in (Lie-A-Fat, 2014) confirmed that the WMF anisotropy decreases with increasing stress. Assuming that those analysis were correct, this suggests that the cause of anisotropy for WMF is not the burial depth which related to the increases of stress, but the laminated structure and the presence of fracture and microcracks. However, some

[37] 4 points in the plot are taken from Fat (2014) data sample.

distortions need to be anticipated to analyze this anisotropy as the very fine layers of shale may significantly affect the seismic wave propagation and contribute to the distortion of seismic image.

5 Conclusions and Recommendations

In Section 5.1, conclusions will be drawn in sequence as per the reviewed topic to answer the research questions. Then recommendations based on the progress and results of this thesis are presented in Section 5.2.

5.1 Conclusion

The first research question "*Could the factors that controlling the occurrence of fracture mode I, and mode II be determined based on the geomechanical, petrophysical, and fracture analysis? And if so, what are the dominant factors?*" are answered by (1) Doing unconfined and confined pressure experiments and analyzing the results; (2) Conducted petrophysical analysis by measuring the porosity and density, and; (3) Perform the fracture analysis by measuring the fracture angle. Based on the experiments followed by an analysis, the answer for this questions are summarized below:

- Based on the geomechanical, petrophysical, and fracture analysis, the occurrence of fracture mode I and mode II is independent to the confining pressure in Indiana limestone and Bad Bentheim sandstone.
- For 8 different lithologies used in this thesis, the strength of the rock, which related to its porosity, is the dominant factor controlling the occurrence of fracture mode I and mode II, based on the geomechanical experiments and petrophysical analysis.
- Brittleness index has a negative correlation with the fracture angle.
- Low strength rocks like BB sandstone (46.65 MPa) and Indiana LS (36.5 MPa) show fractures angle between 10 - 35 º with respect to the maximum principal stress (fracture mode II). On the contrary, stronger rocks like Belgium LS and Granite (125 and 128 MPa respectively) have slightly vertical fracture's plane, 6º angle to the vertical σ_1, which display fracture mode 1.

However some further investigations with higher confining pressure is recommended for the stronger rock, those with fracture mode I occur at the beginning at zero confining pressure.

The second research question "*What are the characteristics of the WMF that can be obtained from the geomechanical, and acoustic experiments, microstructural, petrophysical, and micro-CT fracture analysis*?" are answered by doing a series of experiments and analysis. From petrophysical analysis, the porosities and densities are obtained. From the geomechanical analysis the Young's modulus and Poisson's ratio are attained. The microstructural are done by doing XRF analysis on the powdered sample, and further process it using BASICA software, the results are the mineralogy including clay, pyrite, and quartz content. From the acoustic experiments, the velocity, seismic anisotropy, and dynamic elastic module are obtained. The micro-CT fracture analysis help to identify the properties of the fractures and quantify it. With the result of geomechanical, mineralogy, and quantification using micro-CT scanner analysis, some brittleness indices and fraccability indices are acquired. Based on the results and discussions followed, the research questions are answered as per below summaries:

- From the petrophysical analysis on WMF, the densities and porosities are varying between 2.17 g/cc and 2.8 g/cc, and between 0.26% and 5.19% respectively.

- From the acoustic experiments done in WMF, the seismic anisotropies is obtained up to 34%. This value is considered as high anisotropy and align with result of (Lie-A-Fat, 2014).
- From the geomechanical experiments, Young's modulus of WMF mostly fall below 20 GPa (4.31 – 19.6 GPa), and the Poisson's ratio value are between 0.20 – 0.40. This value falls in the low range compared to other (productive) shale.
- The dynamic-to-static correlations of WMF Young's modulus followed the trend of clastic rocks according to (Britt & Schoeffler, 2009).
- WMF mineralogy extracted from the XRF results show 39 -72% of clay, 2.9 – 16.50% of quarts, 1 – 46% of carbonate, 3.9 – 10% of pyrite. Confirms with the result of (Lie-A-Fat, 2014).
- From the fracture characterization using micro CT-scanner in WMF, it is known that the higher the ultimate strength and E, the longer the total fracture length. While the aperture will become smaller.
- Compared to the average fracture length, aperture plays a dominant role in determining the trend of porosity.
- In determining the fracture toughness, the Young's modulus plays a dominant role compared to other parameters.
- From geomechanical experiments, fracture quantification, and mineralogy analysis, three brittleness indices and six fraccability indices of WMF are determined in this research. Each brittleness index in this study represents different rock characteristic, and as it is defined in different ways, the trend are not consistent even though the data are coming from the same samples.

The last research questions *"Could the empirically determined characteristics of WMF be used to evaluate the potential for future gas exploration in PSF, and what are the most potential horizons within the WMF?"* is answered by comparing the characteristics of WMF to the proven production shale as defined by (Britt & Schoeffler, 2009; Bruner & Smosna, 2011; Rickman, et al., 2008; Sone & Zoback, 2013). The petrophysical results suggest that WMF is less promising compared to the proven American shales. The Young's modulus obtained from geomechanical experiments are lower compared to the prospective shales according to (Britt & Schoeffler, 2009), which makes WMF less promising. The trend of static – dynamic Young's modulus of WMF suggested that WMF can be categorized as prospective shale according to (Britt & Schoeffler, 2009), but this conclusion is weak because the trend lays in the lowest possible prospective shales. The high clay content and low quartz content of WMF compared to other prospective shales indicates that the WMF is less potential.

Eventually The WMF is divided into four sections based on the parameters trend, and none of the sections is supported by all parameters to be favorable. Looking at the brittleness index, fraccability index, and anisotropy, zone 1 looks promising. But due to the low porosity this conclusion is questionable. Another option is zone 4, which has highest porosity value, low clay content, and relatively moderate value of brittleness index and fraccability indices. The result of anisotropy in this section is also low compare to other sections. Furthermore the Young's modulus in zone 4 is close to the range of prospective shales as defined by (Britt & Schoeffler, 2009). The fact that the longest fractures are created in this section supported this conclusion. Looking at the Pyrite content which presumably related to the TOC value (Zijp, et al., 2014), zone 3, and upper part of zone 2 are more favorable than

the other zones. But as this study does not include any data of TOC to confirm the relationship, the choice for zone 3 and upper part of zone 2 is eliminated.

The low value of BI and FI value in the border between zone 1 and zone 2 indicates that this area is a ductile formation. As an implication, the formation could act as a barrier on the hydraulic fracturing treatment, which prevent the fracture to growth vertically (Yang, et al., 2013).

5.2 Recommendations

1. To further investigate and validate the relationship between fracture angle and confining pressure as presented by (Ramsey & Checter, 2004), a series of experiments with higher confining pressure might be worth to be done in the future. This is suggested for the stronger rock like granite and Belgium limestone. From this experiments hopefully a continuous changing from fracture mode I to mode II can be observed.
2. The microstructural analysis (XRF) were only done to the WMF shale, for the purpose of determining the characteristic and define the most promising horizons. To investigate the correlation between mineralogy with the fracture angle, the XRF might also be done to the other rock types.
3. Most of the result are lack of data points in between 3-4 m height. It might be worth to collect sample from to fill up the gap to get more extensive and elaborate results of WMF characteristics.
4. For new samples that might be collected in the future, it will be better option to store the sample in a fridge to prevent the sample from further dryout/ weathering. A lot of samples found are already break and split, especially in the layering process. It created difficulties in preparing the samples. Furthermore it caused distorted result on the velocity and fracture analysis results.
5. The XRD analysis in this research could not be performed due to the limitation of the scorecard used by 3ME department for the XRD analysis. Their scorecard do not include some clay minerals. For future study it might be worth to find a lab that can do XRD analysis for different clay mineral, eg.: Corelab. This way the results will be more accurate, and some assumption can be eliminated.
6. To confirm which of the brittleness index that best represent the fraccability of a formation, further investigations about the fracture networks, and other fracture characteristics (porosity, length, width) in relation with the geomechanical properties and mineralogy data need to be conducted. These investigations should be performed in a various reservoir rocks, which has been proven as a good producer until the one that is categorized as a dry formation. This way a brittleness index which best represents the fraccability and the prospectivity of a formation in general can be choosen or even newly formulated.
7. A flow test experiments can be incorporated in order to obtain information about the permeability and further investigate about the relation between certain fracture characteristics and the productivity.

References

Alejano, R., Perucho, A., Ollala, C. & Jimenez, R., 2014. *Rock Engineering and Rock Mechanics: Structures in and on Rock Masses.* London: CRC Press by Taylor and Francis Group.

Altamar, R. P. & Marfurt, K., 2014. Mineraloy-based brittleness prediction from seismic data: Application to the Barnett Shale. *Interpretation,* pp. 255-271.

Aydin, A., 2000. "Fractures, faults, and hydrocarbon entrapment, migration and flow.. *Marine and Petroleum Geology,* pp. 17(7), 797-814..

Bai, B., Elgmati, M., Zhang, H. & Wei, M., 2013. Rock Characterization of Fayetteville shale gas plays. *Fuel Vol.105*, pp. 645-652.

Barnhoorn, A., Cox, S. F., Robinson, D. J. & Senden, T., 2010. Stress-and fluid-driven failure during fracture array growth: Implications for coupled deformation and fluid flow in the crust. *Geology, 38(9),* pp. 779-782.

Bernard, S. et al., 2013. FIB-SEM and TEM Investigations of an Organic-rich Shale Maturation Series from the Lower Toarcian Posidonia Shale, Germany: Nanoscale Pore System and Fluid-rock Interactions. Electron Microscopy of Shale Hydrocarbon Reservoirs. *AAPG Memoir 102,* p. 53.

Bertotti, G., 2014. *Mode I - Mode II,* s.l.: s.n.

Bertotti, G., Primarini, M., Barnhoorn, A. & Bisdom, K., 2015, under review. *The transition from mode I to mode II fracturing in the field and experiments,* Delft: s.n.

Bertotti, G., Primarini, M., Barnhoorn, A. & Bisdom, K., 2015, under review. *The transition from mode I to mode II fracturing in the field and experiments,* Delft: s.n.

Bouw, S. & Lutgert, J., 2012. *Shale Plays in The Netherlands.* s.l., s.n.

Brace, W., 1964. Brittle fracture of rocks. In: *State of Stress in the Earth's Crust.* New York: American Elsevier, pp. 111-180.

Britt, L. K. & Schoeffler, J., 2009. *The Geomechanics Of A Shale Play: What Makes A Shale Prospective.* s.l., Society of Petroleum Engineers.

Bruner, K. R. & Smosna, R., 2011. *A Comparative Study of the Mississippian Bernett Shale, Fort Worth Basin, and Devonian Marcellus Shale, Appalachian Basin.,* s.l.: U.S. Department of Energy.

Bruner, K. & Smosna, R., 2011. *A Comparative Study of the Mississippian Barnett Shale, Fort Worth Basin, and Devonian Marcellus Shale, Appalachian Basin,* s.l.: US Department of Energy.

Chester, F. M. & Logan, J. M., 1986. Implications for mechanical properties of brittle faults from observations of the Punchbowl fault zone, California.. *Pure and Applied Geophysics,* pp. 124(1-2), 79-106..

Ciccotti, M. & Mulargia, F., 2004. Difference between static and dynamic alstic moduli of a typical seismogenic rock. *Journal of Geophysics,* pp. 474-477.

Coates, D. & Parsons, R., 1966. Experimental criteria for classification of rock substances. *International Journal of Rock Mechanics and Mining Sciences & Geomechanics,* pp. 181-189.

Curtis, J., 2002. Fractured shale-gas systems. *AAPG Bulletin,* Volume 86, pp. 1921 - 1938.

Du, C. et al., 2009. *A workflow for integrated Barnett Shale gas reservoir modeling and simulation.* s.l., Society of Petroleum Engineers.

E.King, G., 2010. *Thirty Years of Gas Shale Fracturing: What Have We Learned?.* Florence, s.n.

Energie Beheer Nederland B.V, 2014. *Focus on Dutch Oil and Gas 2014,* s.l.: s.n.

Engelder, T., 1999. Transitional-tensile fracture propagation: a status report. *Journal of Structural Geology 21,* pp. 1049-1055.

Fossen, H., 2010. *Structural Geology.* Bergen: Cambridge University Press.

Godderij, R. et al., 2014. *A Conceptual Shale Gas Field Development Plan for the Lower Jurassic Posidonia Shale in The Netherlands.* s.l., s.n.

Grigs, D. & Handin, J., 1960. Rock Deformation (A Symposium). *The Geological Society of America Memoir 79,* pp. 346-365.

Hancock, P., 1985. Brittle microtectonic: principles and practice.. *Journal of Structural Geology,* pp. 437 - 457.

Handing, D. G. & John, 1960. Rock Deformation (A Symposium). In: *The Geological Society of America, Memoir 79.* s.l.:s.n., pp. 347-364.

Handin, J., 1969. On the Coulomb-Mohr Failure Criterion. *Journal of Geophysical Research,* 74(22).

Handin, J. & Hager, R. J., 1957. Experimental Deformation of sedimentary rocks under confining pressure: Tests at room temperature on dry samples. *Bulletin of the American Assciation of Petroleum Geologists.*

Handin, J. & Hager, R. V. J., 1958. Experimental Deformation of Sedimentary Rocks Under Confining Pressure: Tests at High Temperature. *Bulletin of the American Association of Petroleum Geologists*, December, pp. 2892-29334.

Handin, J., Hager, R. V. J., Friedman, M. & Feather, J. N., 1963. Experimental Deformation of Sedimentary Rocks Under Confining Pressure: Pore Pressure Test. *Bulletin of the American Association of Petroleum Geologists*, May.

Hawkes, I. & Mellor, M., 1970. Uniaxial testing in rock mechanics laboratories. *Engineering Geology,* 4(3), pp. 179-285.

Hendrikx, R., 2015. *Axios Report WMF Sample Mutia Ifada,* Delft: X-ray diffraction facilities, Maetrials Science and Engineering TU Delft, Faculty of 3mE.

Holt, R., Fjaer, E., Nes, O. & Alassi, H., 2011. *A shaly look at brittleness.* Dan Francisco, CA, ARMA.

Houben, M. et al., 2015, under review. Microstructural characteristics of the Whytby Mudstone Formation (UK). *Marine and Petroleum Geology.*

Houben, M. E. et al., 2014. *Microstructural Investigation of the Whitby Mudstone (UK) As an Analog for Posidonia Shale (NL).* s.l., s.n.

Jarvie, D., Hill, J., Ruble, T. & Pollastro, R., 2007. Unconventional shale-gas system: The Mississippian Barnett Shale of North-Central Texas as one model for thermogenic shale-gas assessment. *AAPG,* 91(doi: 10.1306/12190606068), pp. 475-499.

Jin, X., Shah, S. N., Rogiers, J.-C. & Zhang, B., 2014. *Fraccability Evaluation in Shale Reservoirs - An Integrated Petrophysics and Geomechanics Approach.* Woodlands, Texas, SPE.

Johnston, J. E. & Christensen, N. I., 1995. Seismic anisotropy of shales. *Journal of Geophysical Research,* pp. 5991-6003.

Jones, L. E. & Christensen, N. I., 1981. Ultrasonic velocities in Cretaceous shales from Wiiliston Basin. *Journal of Geophysics ,* Volume 46 No 3, pp. 288-297.

Jorand, C., Chemenda, A. & Petit, J.-P., 2012. Formation of parallel joints sets and shear band/fracture networks physical models. *Tectonophysics,* Volume 581, pp. 84-92.

Ketcham, R. & Hanna, R., 2014. Beam hardening correction for X-ray computed tomography of heterogeneous natural materials. *Journal of Computers and Geosciences,* Volume 67, pp. 49-61.

Klimczak, C., Schultz, R., Parashar, R. & Reeves, D., 2010. Cubic law with aperture - length correlation: implications for network scale fluid flow. *Hydrogeology Journal.*

Leem, J. et al., 2014. *Geomechanics in Optimal Multi-Stage Hydraulic Fracturing Design for Resource Shale and Tight Reservoirs.* Dubai, EAGE.

Leem, J. et al., 2014. *Geomechanics in Optimal Multi-Stage Hydraulic Fracturing Design for Resource Shale and Tight Reservoirs..* s.l., EAGE.

Lie-A-Fat, J., 2014. *Microstructural, Petrphysical and Anisotropy Analysis of a Posidonia Shale Analogue, Msc. Thesis,* Delft: TU Delft.

Machinsky, E., 2003. *Difference between static and dynamic elastic moduli of rocks: Physical Causes.* Novosibirsk, s.n., pp. 953-959.

Marion, D., Nur, A., Yin, H. & Dam, D., 1992. Compressional velocity and porosity in sand - clay mixtures. *Geohysics Vol. 57 No. 4,* pp. 554 - 563.

Martinez, J., Benavente, D. & Garcia-Del-Cura, M., 2011. Comparison of static and dynamic elastic modulus in carbonate rocks. In: s.l.:Springer - Verlag, pp. 263 - 268.

Mashinsky, E., 2003. Differences Between Static and Dynamic Elastic Moduli of Rocks: Physical Causes. *Russian Geology and Geophysics,* pp. 916 - 922.

Maxwell, S. & Norton, M., 2012. *The Impact of Reservoir Heterogeneity on Hydraulic Fracture Geometry: Integration of Microseismic and.* Long Beach, California, s.n.

Meyer, B. R. & Bazan, L. W., 2011. *A Discrete Fracture Network Model for Hydraulically Induced Fractures-Theory Parametric and Case Studies.* s.l., Society of Petroleum Engineers..

Muller, O. & Pollard, D., 1977. The stress state near Spanish Peaks, Colorado determinded from a dike pattern.. *Journal of Pure and Applied Geophysics 115,* pp. 69-86.

Myrvang, A., 2001. *Bergmekanikk,* Trondheim: Institutt for geology og bergteknikk, NTNU.

Nakashima, S., Hasegawa, D., Kishida, K. & Yasuhara, H., 2010. *Measurements of Fracture Aperture in Granite Core Using Microfocus X-Ray CT.* Salt Lake City, ARMA.

Nolte, P. L. J., Myer, L. R., Cook, N. G. & Witherspoon, P. A., 1987. *Hydraulic and mechanical properties of natural fractures in low permeability rock.* s.l., s.n.

Olson, J. E., 2003. Sublinear scaling of fracture aperture versus lenght: An exception or the rule?. *Journal of Geophysical Research,* pp. Vol 108,NoB9, 2413, doi: 10.1029/2001JB000419,2003.

Passey, Q. R. et al., 2010. *From oil-prone source rock to as-producing shale reservoir–geologic and petrophysical characterization of unconventional shale-gas reservoirs.* Beijing, SPE.

Pearson, C., 1981. The relationship between microseismicity and high pore pressures during hydraulic stimulation experiments in low permeability granitic rocks. *Journal of Geophysical Research: Solid Earth (1978–2012), 86(B9), 7855-7864.*

Pyrak-Nolte, L. J. M. L. R. C. N. G. &. W. P. A., 1987. *Hydraulic and mechanical properties of natural fractures in low permeability rock.* s.l., s.n.

R. Rickman, M. M. E. P. B. G. D. K., 2008. *A practical use of shale petrophysics for stimulation design optimization: all shale plays are not clones of Barnett Shale.* s.l., s.n., pp. 840-850.

Ramsey, J. M. & Checter, F. M., 2004. Hybrid fracture and the transition from extension fracture to shear fracture. *Letters to Nature,* Volume 428, pp. 63-66.

Rao, Q. et al., 2003. Shear fracture (Mode II) of brittle rock. *International Journal of Rock Mechanics and Mining Sciences,* p. 355–375.

Ravenstein, T., 2014. *Fraccability determination of a Posidonia Shale Formation analogue through geomechanical experiments and micro-CT fracture propagation analysis,* Delft: Tu Delft.

Ren, L., Zhao, J. & Hu, Y., 2014. *Hydraulic Fracture Extending into Network in Shale: Reviewing Influence Factors and Their Mechanism,* Chengdu: s.n.

Renshaw, C. E., 1996. Influence of subcritical fracture growth on the connectivity of fracture networks.. *Water Resources Research,* pp. 32(6), 1519-1530..

Rickman, R. et al., 2008. *A practical use of shale petrophysics for stimulation design optimization: all shale plays are not clones of Barnett Shale.* s.l., s.n., pp. 840-850.

Sayers, C., 1999. Stress-dependent seismic anisotropy of shales. *Journal of Geophysics,* 64(doi: 10. 1190/1. 1444535), pp. 93-98.

Schavemaker, Y. A. Z. M. t. H. J. N. S. &. T. V. J., 2013. *Multidisciplinary Approach for Detailed Characterization of Shale Gas Reservoirs: A Netherlands Showcase..* Brasil, s.n.

Secor, D. T., 1965. Role of fluid pressure in jointing. *American Journal of Science,* 263(8), pp. 633-646.

Singhal, B. & Gupta, R., 2010. Applied Hidrogeology of Fractured Rocks, Second Edition. In: s.l.:Springer Science & Business Media, p. 25.

Sone, H. & Zoback, M., 2013. Mechanical Properties of shale-gas reservoir rocks - Part 1: Static and dynamic elastic properties and anisotropy. *Journal of Geophysics, Vol.78,* pp. D381-D393.

Suppe, J., 1985. *Principles of Structural Geology.* New Jersey: Prentice-Hall, Englewood Cliffs.

TerHeege, J. H., Zijp, M., DeBruin, G. & Buijze, L., 2014. *Upfront Predictions of Hydraulic Fracturing and Gas Production in underexplored shale gas basins: Example of the Posidonia Shale Formation in the Netherlands.* Minneapolis, American Rock Mechanics Association..

Walsh, J., 1965. The Effect of Cracks in Rocks on Poisson's Ratio. *Journal of Geophysical Research.*

Wang, F. & Gale, J., 2009. Screening criteria for shale-gas systems. *Gulf Coast Association of Geological Societies Transaction*, pp. 779-793.

Warpinski, N. et al., 2009. Stimulating Unconventional Reservoirs: Maximizing Network Growth While Optimizing Fracture Conductivity. *Journal of Canadian Petroleum Technology,* 48(http://dx.doi.org/10.2118/114173-PA).

Waters, G., Lewis, R. & Bentley, D., 2011. *The Effect of Mechanical Properties Anisotropy in The Generation of Hydraulic Fractures in Organic Shales.* s.l., SPE.

Weng, X. et al., 2011. Modeling of hydraulic-fracture-network propagation in a naturally fractured formation. *SPE Production & Operations*, pp. 26(04), 368-380.

Wong, T., 2007. Jurassic. Geology of the Netherlands. In: s.l.:s.n., pp. 107-125.

Yang, Y., Sone, H., Hows, A. & Zoback, M., 2013. Comparison of Brittleness Indices in Organic-rich Shale Formations. *American Rock Mechanics Association.*

Zhang, X. & Jeffrey, R., 2013. *Development of Fracture Networks Through Hydraulic Fracture Growth in Naturally Fractured Reservoirs.* s.l., s.n.

Zhiqi, G. et al., 2013. A Shale rock physics model for analysis of brittlenessindex, mineralog, and porosity in the Barnett Shale. *Journal of Geophysics and Engineering.*

Zhubayev, A. & Barnhoorn, A., 2013. *Seismic Anisotropy of Posidonia Shale,* Delft: TU Delft.

Zhubayev, A., Houben, M., Smeulders, D. & Barnhoorn, A., 2014. *Geomechanical and anisotropic acoustic properties of Lower Jurassic Posidonia shales from Whitby (UK).* Wina, s.n.

Zijp, M. et al., 2013. *Multidisciplinary Approach for Detailed Characterization of Shale Gas Reservoirs: A Netherlands Showcase..* Brasil, SPE.

Zijp, M. et al., 2014. *New Insights from Jurassic Shale Characterization: Strenghten Subsurface Data With Outcrop Analogues.* Vienna, SPE.

Ziony, J., 1966. *Analysis of systematic jointing in part of the Monument Upward, southwestern Utah, Phd Thesis.,* Los Angeles: University of California at Los Angeles.

Appendix

A. Porosity and Matrix Density Measurements

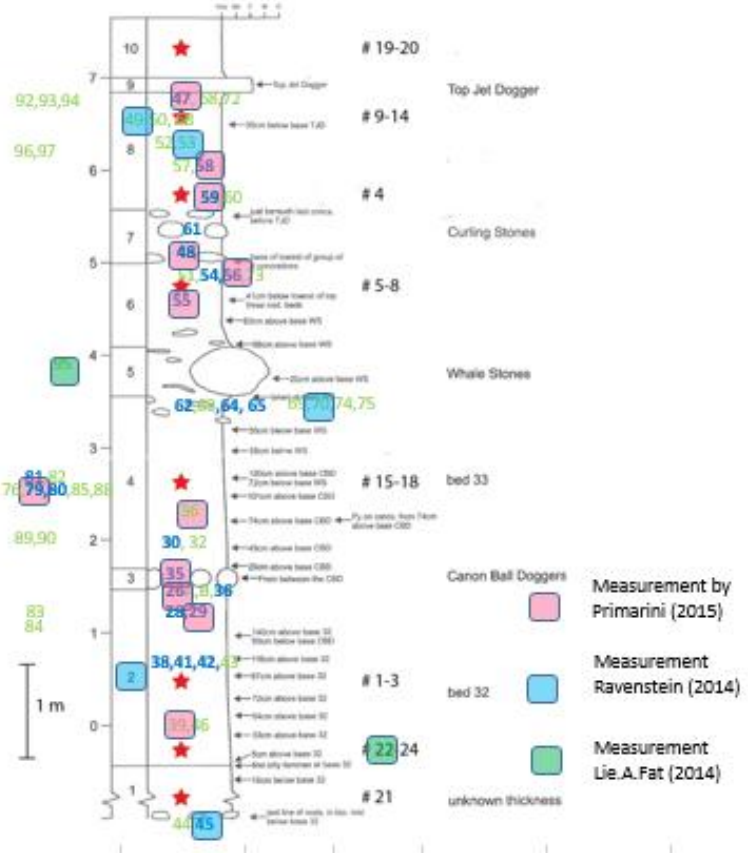

Figure 74. Samples used for matrix density and porosity measurements

Table 13. Result of Porosity and density measurements

Sample no.	Fm. Height [m]	Matrix Density [g/cc]	Porosity [-]
26a	1.4	2.42	3.57
26b	1.4	2.42	4.11
29a	1.2	2.40	0.38
29b	1.2	2.41	5.19
35a	1.6	2.25	1.94
35b	1.6	2.27	3.79
36a	2.2	2.27	4.61
36b	2.2	2.26	2.82
39a	0	2.50	3.64
39b	0	2.42	
47	6.8	2.47	4.47
48.a	5	2.24	
48.b	5	2.24	1.31
55a	4.7	2.26	2.65
55b	4.7	2.29	4.30
56	4.9	2.46	3.64
58a	6	2.40	4.76
58b	6	2.39	0.26
59a	5.7	2.17	
59b	5.7	2.42	1.97
79a	2.5	2.32	
79b	2.5	2.27	4.28

B. Geomechanic

B.1. Calibration for Simple Triaxial Test Chamber

In order to get the elastic properties of the sample, by applying certain confining pressure, the simple triaxial test was done using the pressure chamber, as can be seen in Figure 75. Picture (Left) and Sketch Drawing (Right) of Experimental set-up using simple triaxial cell. The sample was put inside the chamber, with the iron placed on top of the sample, and there was a piston on top of the chamber which would transfer the compression force from the pressure bench to the sample.

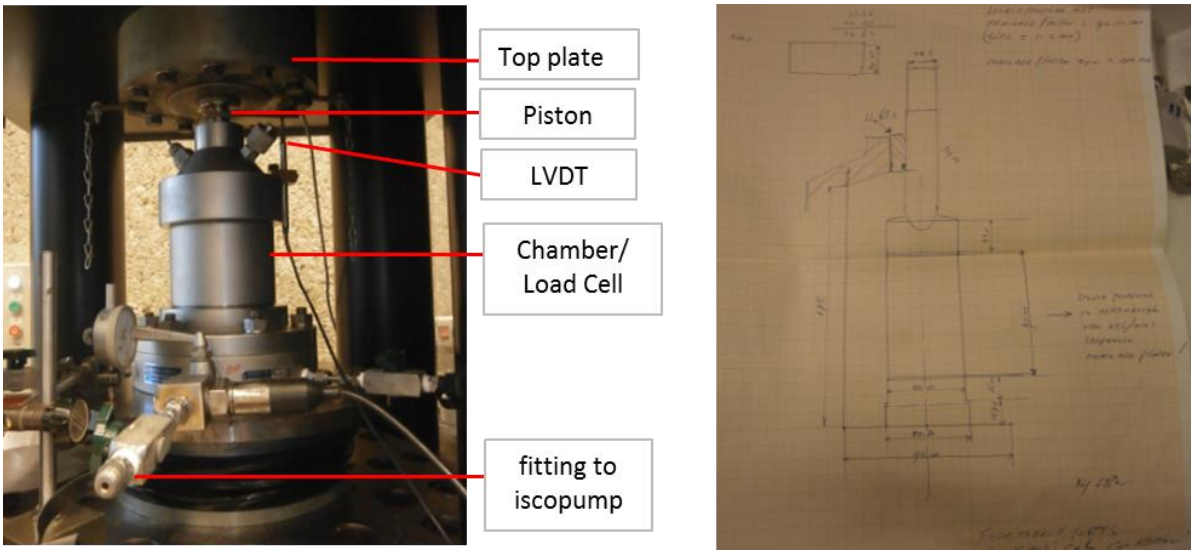

Figure 75. Picture (Left) and Sketch Drawing (Right) of Experimental set-up using simple triaxial cell

The experiments were done by water pressurized the chamber until the desired confining pressure using ISCO pump. The pressure acted in all direction. After it, the deformation test was done by applying the compression force to the piston. This force initially would act against the confining pressure, and looked for the right contact with the sample, this is called deviator stress. Thus the measured stress and strain given by the hoek 3 cell (data acquisition program) was not the sample properties, instead it was the whole system set-up properties. Calibration need to be done for the Triaxial Test chamber, to get the correction factor that can be applied in order to get the true sample properties.

Calibration was done by placing the iron steel cylinder with the height of 80 mm and diameter of 40 mm into the chamber. Iron steel was used to calibrate the apparatus, since the Young's Modulus is known from the literature as 210 GPa[38]. By knowing the E (Young's Modulus) and the stress, the strain can be calculated (eq. 1)

$$\mathcal{E}_{\text{vertical}} = \frac{\Delta L}{L}$$

$$\mathcal{E} = \sigma_{\text{differential}}/E \qquad (1)$$

Thus for each differential stress measured, the value of correction for strain can be calculated by substracting the measured - strain by the iron steel - strain. (eq. 3)

$$\mathcal{E}\ measured = \mathcal{E}\ iron + \mathcal{E}\ apparatus\ (correction) \qquad (2)$$

$$\mathcal{E}\ correction = \mathcal{E}\ measured - \mathcal{E}\ iron \qquad (3)$$

The differential stress that being used to calculate the strain and also to be plotted in the differential stress – strain graph is calculated using equation 4.

$$\sigma_{\text{diffentaial}} = F_{\text{differential}}/A_{\text{sample}} \quad , \qquad (4)$$

$$F_{\text{differential}} = F_{\text{measured}} - F_{\text{correction}}, \qquad (5)$$

[38] (source: http://www.engineeringtoolbox.com/young-modulus-d_417.html)

F correction is the force against the confining pressure.

$F_{correction} = \sigma_{(CP)} \times A_{piston}$ (6)

Step for Calibration

1. We did calibration using steel in two different confining pressures (CP) of 6 MPa and 15 MPa. Both of them showed that the differential stress-strain slope of the system is the same. The slope of the iron also overlay each other (Figure 76). So it was decided to use only one data to get the calibration or correction factor. The strain value of the iron steel was calculated.

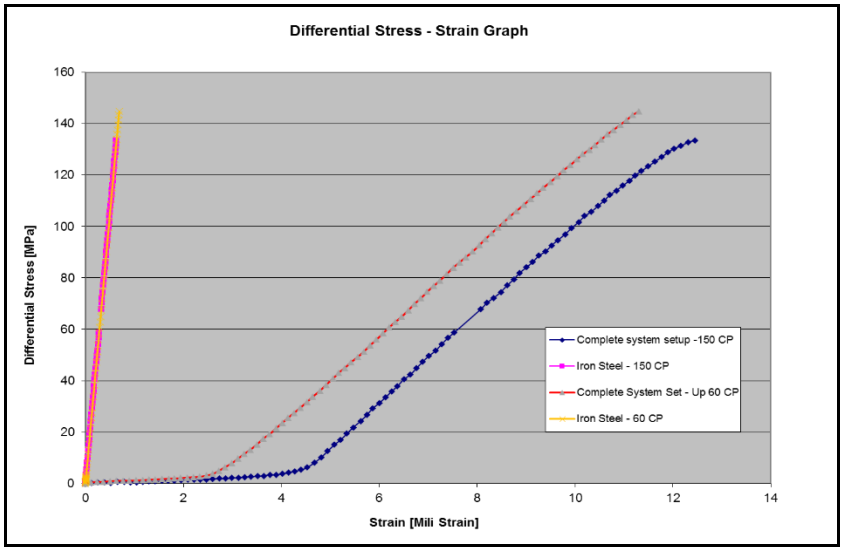

Figure 76. Differential Stress – Strain Graph of Iron and the System set-up for 60 (6 MPa) and 150 CP (15 MPa)

2. To get the correction equation the data from experiment in 6 MPa CP was used. First we needed to remove the data in the first slope, as it is including the deviator stress (stress that was occured not to deform the sample but as a reaction of the piston to get the best contact with the sample). It was identified by the big changing in strain with the small differential stress (see Figure 77 left for illustration). The correction strain was calculated using equation. 3.

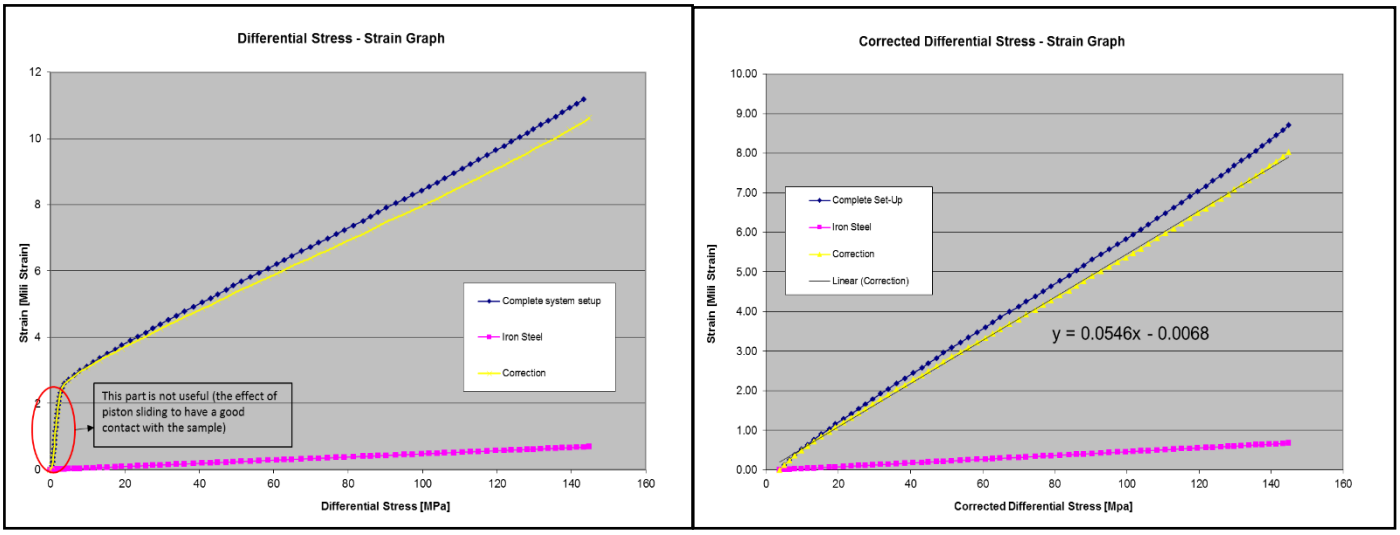

Figure 77. Differential Stress - Strain Graph for Iron, System set-up, and correction factor. (Strain as the y-axis). The red circle indicating the part that need to be removed (left side), and Corrected Differential Stress - Strain Graph for Iron, to get the correction factor (right side).

3. Set the first strain when the chart is changing steep to zero, and subtract all the strain data with the corresponding value of strain that had been used to set the first data to zero. Using this new chart, linear trend line was made for the corrected differential stress – strain correction graph to get the equation for the correction (see figure 3, right side, for the illustration)
The equation for correction is **y = 0.0564 x – 0.0068** (eq.7)
Where y is the strain, and x is the stress (corrected differential stress).

Applying the Calibration Equation

To apply the calibration, the experiments data sample (in this case Sandstone) has to be started from zero strain. Erase the data point when the graph is giving a lot of strain with small differential stress (it is because the piston is looking for a contact point), and set the first strain after it as zero. The rest of the strain data then needs to be subtracted with the corresponding value of strain that had been used to set the first data to zero.

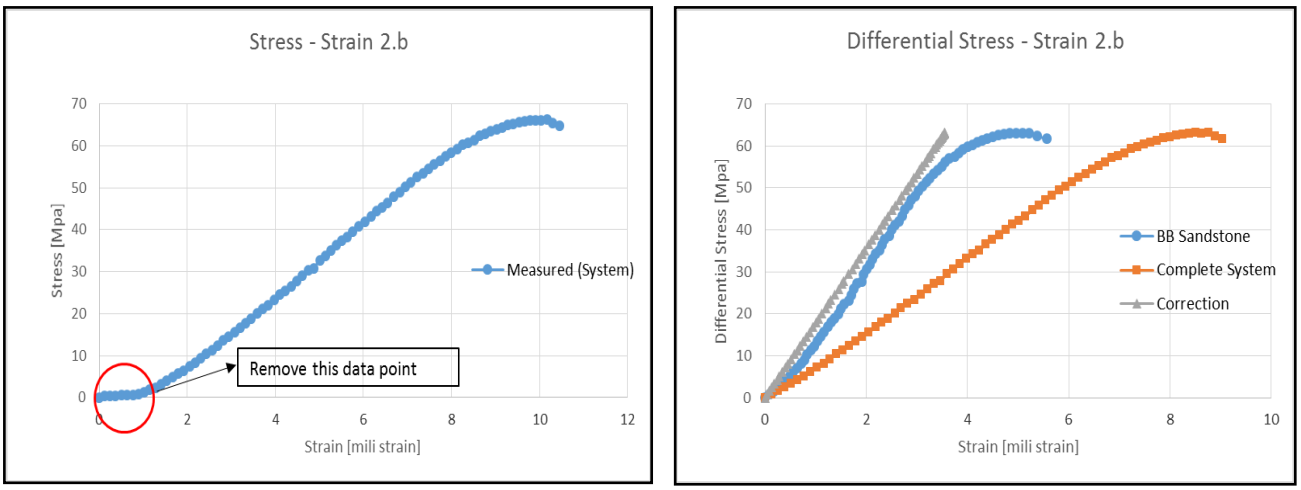

Figure 78. Measured Stress- Strain of the sample sample (left), and Differential Stress – Strain of Bentheim Sandstone plot for CP = 3 MPa (right).

After removing the first un-useful data point, the correction equation **(eq.7)** gotten from the iron experiments is applied to the data set to get the correction data and corrected strain, based on the given stresses. From the corrected strain and stress, then we can construct the plot and get the true value of Young's modulus of the sample. Figure 78. Measured Stress- Strain of the sample sample (left), and Differential Stress – Strain of Bentheim Sandstone plot for CP = 3 MPa (right)., right, illustrates the plot of differential stress – strain for sandstone, with its correction.

Table 14. Example of Data Set (With the Correction process)

Measured Force	Differential Force	Measured Strain	Corrected Measured Strain	Measured Stress	Differential Stress	Corrected Stress	Corrected Stress_2	Correction for Strain	Corrected Strain
[kN]	[kN]	[*10^-3]	[*10^-3]	[Mpa]	[Mpa]	[Mpa]	[Mpa]	[*10^-3]	[*10^-3]
5.905	4.37	1.41	0.00	4.77	3.53	3.17	0.00	0.00	0.00
6.925	5.39	1.53	0.13	5.59	4.36	3.99	0.82	0.04	0.09
7.9	6.37	1.66	0.26	6.38	5.14	4.78	1.61	0.08	0.17
8.97	7.44	1.79	0.39	7.25	6.01	5.65	2.48	0.13	0.26
9.975	8.44	1.92	0.52	8.06	6.82	6.46	3.29	0.18	0.34
11.275	9.74	2.05	0.65	9.11	7.87	7.51	4.34	0.24	0.41

B.2. Calibration for Unconfined Pressure Experiments - Shale

To accommodate the height requirements of the pressure bench for unconfined pressure test (UCS) apparatus, some aluminum sample were inserted between the shale sample and the pressure bench. See Figure 79 for illustration. As the software UCSiket[39] gives the total value of aluminum and shale strain (ε_{AL+SH}), some steps are done to get the strain value of shale.

[39] Data acquisition software for unconfined pressure test, measuring vertical and horizontal strain

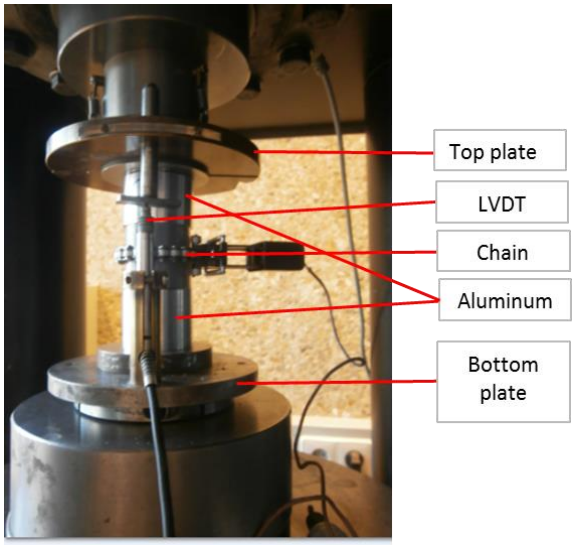

Figure 79. Experimental set-up for shale unconfined pressure test (UCS).

From the material supplier it is known that the aluminum has E= 69 GPa. Knowing the stress applied (σ, from data acquisition) and the E of the Aluminium (E_{Al}), strain of aluminium (ε_{AL}) can be calculated as per below:

$$\varepsilon_{AL} = \sigma / E_{Al} \qquad (8)$$

Once the ε_{AL} is known, the strain of shale (ε_{SH}) can be obtained from:

$$\varepsilon_{SH} = \varepsilon_{AL+SH} - \varepsilon_{AL} \qquad (9)$$

After getting all the data, a plot can be created as in Figure 80 :

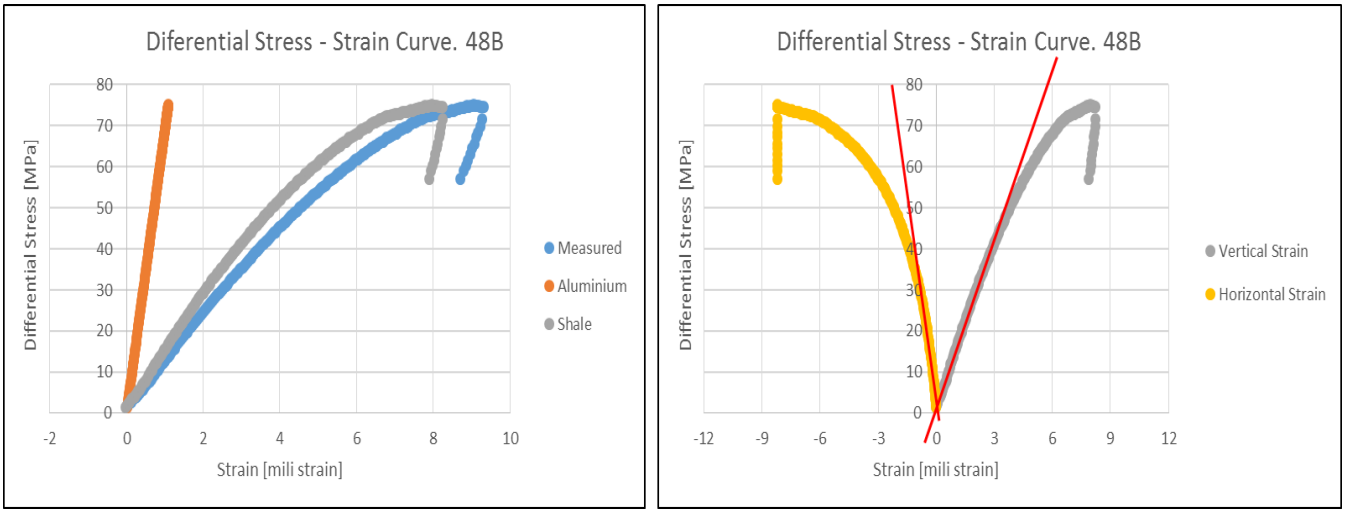

Figure 80.Differential Stress – strain plot for Aluminum, shale, and measured system (left), and the Plot for shale with vertical and horizontal strain (right).

B.3. Figure of Sandstone Samples after confining pressure test

Figure 81. Example of BB Sandstone after the Confined pressure test (different number corresponds to different confining pressure)

C. Velocity and Seismic Anisotropy Measurements

Figure 82 shows the height section in which the velocity and anisotropy were conducted, and Table 15 summarizes the result from these experiments.

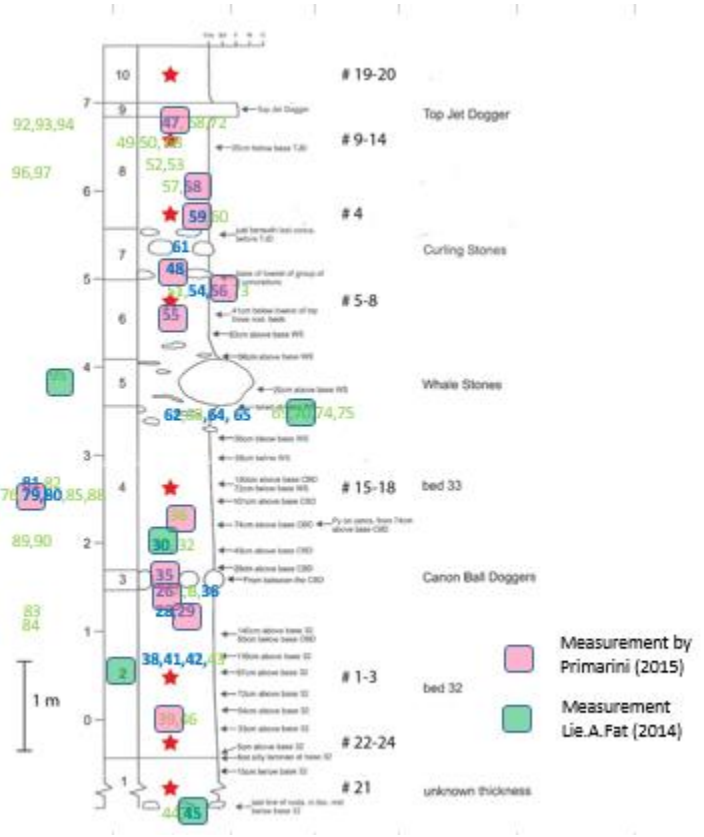

Figure 82. Samples with correspondence height used for the velocity and anisotropy measurements

Table 15. Velocities and Anisotropies Result of WMF Shale

	Normal to the bedding (V0)		Paralel to the bedding (V90)		Seismic Anisotropies	
Sample	Velocity P-wave [m/s]	Velocity S-wave [m/s]	Velocity P-wave [m/s]	Velocity S-wave [m/s]	P-wave Anisotropies [%]	S-wave Anisotropies [%]
26a	2453	1520	3327	1945	26.29	21.85
26b	2406	1530	3310	1949	27.31	21.53
29a	2396	1510	3221	2092	25.62	27.84
29b	N/A	1562	N/A	2248	N/A	30.53
35a	1922	1248	2477	1532	22.39	18.52
35b	2266	1442	3243	2062	30.12	30.06
36a	2225	1453	2954	2008	24.66	27.64
36b	2301	1471	3073	1959	25.12	24.88
39a	1992	1576	2760	1990	27.83	20.80
39b	2237	1580	3134	1972	28.61	19.90
47	2573	1762	3542	2304	27.38	23.53
48.a	2304	1500	3114	1939	26.00	22.64
48.b	2301	1498	3078	1963	25.24	23.69
55a	2527	1515	3547	2308	28.76	34.37
55b	2533	1634	3686	2420	31.29	32.46
56	1849	1422	2677	2155	30.93	34.00
58a	2481	1602	3247	2045	23.61	21.66
58b	2665	1731	3794	2515	29.77	31.19
59a	N/A	N/A	N/A	N/A	N/A	N/A
59b	2315	1559	N/A	N/A	N/A	N/A
79a	2346	1452	3247	2100	27.75	30.84
79b	2241	1431	3000	2090	25.30	31.53

D. XRF Analysis

Table 16. XRF results of sample 26, 29, 35, 36, 39, and 47.

#26		#29		#35		#36		#39		#47	
Compound	wt%	Compound	wt%	Compound	wt%	Compoun	wt%	Compoun	wt%	Compoun	wt%
SiO2	52.416	SiO2	51.253	SiO2	48.971	SiO2	53.165	SiO2	53.962	CaO	35.718
Al2O3	19.805	Al2O3	20.226	Al2O3	17.718	Al2O3	19.22	Al2O3	19.68	SiO2	30.376
SO3	10.248	SO3	10.526	SO3	11.517	SO3	8.927	Fe2O3	9.376	Al2O3	11.377
Fe2O3	9.675	Fe2O3	9.584	Fe2O3	9.966	Fe2O3	8.38	SO3	8.936	Fe2O3	9.398
K2O	2.572	K2O	2.2652	CaO	4.489	CaO	3.687	K2O	2.699	SO3	7.105
MgO	2.016	MgO	2.047	K2O	2.759	K2O	2.714	MgO	1.988	MgO	2.048
CaO	1.231	CaO	1.79	MgO	2.146	MgO	1.991	CaO	1.178	K2O	1.776
TiO2	0.921	TiO2	0.961	TiO2	0.806	TiO2	0.877	TiO2	0.982	TiO2	0.65
Na2O	0.423	Na2O	0.424	Na2O	0.558	Na2O	0.429	Na2O	0.606	P2O5	0.457
Cl	0.167	Cl	0.245	P2O5	0.518	P2O5	0.166	P2O5	0.168	Na2O	0.426
MnO	0.152	P2O5	0.123	Cl	0.132	Cl	0.096	Cl	0.107	SrO	0.188
P2O5	0.131	F	0.076	F	0.109	F	0.071	F	0.081	MnO	0.137
Fe2O3	0.068	CeO2	0.042	MnO	0.058	MnO	0.048	CeO2	0.043	Cl	0.129
Cr2O3	0.029	MnO	0.037	V2O5	0.056	BaO	0.043	MnO	0.033	F	0.069
CeO2	0.021	Cr2O3	0.024	ZnO	0.044	V2O5	0.04	NiO	0.029	V2O5	0.033
NiO	0.02	ZrO2	0.019	NiO	0.027	ZrO2	0.024	BaO	0.026	NiO	0.031
ZrO2	0.014	BaO	0.017	Cr2O3	0.022	CuO	0.022	ZrO2	0.025	Cr2O3	0.019
SrO	0.014	ZnO	0.017	BaO	0.021	Cr2O3	0.021	Cr2O3	0.019	ZnO	0.016
BaO	0.014	NiO	0.016	SrO	0.02	SrO	0.02	SrO	0.014	ZrO2	0.016
Rb2O	0.013	SrO	0.015	ZrO2	0.02	ZnO	0.016	ZnO	0.012	CuO	0.009
ZnO	0.012	Rb2O	0.013	CuO	0.016	NiO	0.015	Rb2O	0.012	Rb2O	0.009
CuO	0.01	CuO	0.011	Rb2O	0.013	Rb2O	0.014	CuO	0.01	PbO	0.007
PbO	0.008	PbO	0.009	Y2O3	0.009	PbO	0.006	PbO	0.008	Y2O3	0.005
Y2O3	0.004	Y2O3	0.004	Nb2O5	0.006	Y2O3	0.005	Y2O3	0.004		
Nb2O5	0.002	Nb2O5	0.003			Nb2O5	0.003	Nb2O5	0.003		

Table 17. XRF results of sample 48, 55, 56, 58, 59, and 79.

#48	
Compoun	wt%
SiO2	47.486
Al2O3	16.871
SO3	13.806
Fe2O3	10.841
CaO	4.295
K2O	2.668
MgO	2.002
TiO2	0.793
Na2O	0.586
P2O5	0.159
F	0.12
Cl	0.077
MnO	0.057
NiO	0.041
CeO2	0.034
V2O5	0.032
Cr2O3	0.024
ZrO2	0.021
SrO	0.018
ZnO	0.015
CuO	0.015
BaO	0.014
Rb2O	0.013
PbO	0.009
Y2O3	0.003
Nb2O5	0.002

#55	
Compoun	wt%
SiO2	43.298
SO3	13.929
Al2O3	13.816
Fe2O3	12.182
CaO	8.82
MgO	2.199
K2O	2.167
P2O5	1.445
TiO2	0.704
Na2O	0.592
Co3O4	0.267
F	0.128
Cl	0.077
MnO	0.072
ZnO	0.052
CeO2	0.041
NiO	0.041
V2O5	0.031
BaO	0.026
SrO	0.024
Cr2O3	0.024
ZrO2	0.022
CuO	0.014
Y2O3	0.011
Rb2O	0.01
PbO	0.007

#56	
Compoun	wt%
SiO2	50.84
Al2O3	19.474
Fe2O3	9.266
SO3	9.084
CaO	4.987
K2O	2.694
MgO	1.798
TiO2	0.908
Na2O	0.43
P2O5	0.14
Cl	0.125
F	0.068
MnO	0.035
BaO	0.022
SrO	0.021
ZrO2	0.02
Cr2O3	0.018
ZnO	0.015
Rb2O	0.015
NiO	0.014
PbO	0.01
CuO	0.008
Y2O3	0.004
Nb2O5	0.003

#58	
Compoun	wt%
SiO2	48.329
Al2O3	17.231
SO3	10.044
CaO	9.457
Fe2O3	9.021
K2O	2.413
MgO	1.79
TiO2	0.785
Na2O	0.308
P2O5	0.217
F	0.084
Cl	0.062
MnO	0.06
CeO2	0.036
SrO	0.033
NiO	0.027
ZrO2	0.02
BaO	0.019
Cr2O3	0.018
Rb2O	0.013
ZnO	0.011
CuO	0.008
PbO	0.008
Y2O3	0.003
Nb2O5	0.002

#59	
Compoun	wt%
SiO2	49.684
Al2O3	18.654
SO3	9.421
Fe2O3	9.201
CaO	6.664
K2O	2.809
MgO	2.01
TiO2	0.839
Na2O	0.271
P2O5	0.135
F	0.078
MnO	0.043
SrO	0.027
Cl	0.025
NiO	0.024
BaO	0.023
ZrO2	0.022
Cr2O3	0.018
ZnO	0.014
Rb2O	0.014
CuO	0.013
PbO	0.007
Y2O3	0.003
Nb2O5	0.003

#79	
Compoun	wt%
SiO2	44.713
Al2O3	16.821
CaO	11.318
SO3	10.382
Fe2O3	9.061
K2O	2.491
MgO	1.899
P2O5	1.526
TiO2	0.758
Na2O	0.455
F	0.116
Cl	0.092
ZrO2	0.071
MnO	0.051
SrO	0.049
ZnO	0.048
NiO	0.037
BaO	0.029
Cr2O3	0.026
Y2O3	0.024
CuO	0.013
Rb2O	0.012
PbO	0.009

Table 18. Mineral composition obtained from XRF results in software BASICA

Sample	Height	ILLITE	KAOLINITE	CHLORITE	MONTMORILLONITE	QUARZ	CALCITE	PYRITE	GOETHITE	OTHER
47	6.8	10.96	10.32	5.47	12.38	2.95	45.97	3.89	6.78	1.27
58	6	17.68	20.52	5.67	10.63	15.90	14.15	6.52	7.81	1.13
59	5.7	20.96	21.19	6.49	9.52	16.50	10.07	6.23	8.02	1.02
48	5	22.12	20.27	7.18	22.88	10.54	6.50	10.14	0.00	0.37
56	4.9	19.96	23.69	5.76	15.00	13.29	7.13	5.96	8.13	1.09
55	4.7	15.48	14.43	6.80	19.92	8.27	12.41	8.82	10.38	3.51
79	2.5	17.54	18.32	5.78	15.08	9.51	16.14	6.48	7.49	3.66
36	2.2	20.29	23.19	6.44	15.10	15.56	5.15	5.91	7.24	1.12
35	1.6	20.32	19.22	6.84	19.36	10.26	6.12	7.52	8.59	1.78
26	1.4	19.58	25.99	6.64	15.16	14.66	1.30	6.91	8.65	1.11
29	1.2	21.33	28.08	0.00	16.22	14.12	2.35	7.58	9.12	1.20
39	0	20.10	24.22	6.40	21.25	11.83	0.91	5.89	8.18	1.22

E. Fracture Characterization

E.1. Data Processing using Avizo®Fire 8.01

Avizo®Fire 8.01 was used to analyze the fractures in shale samples. CT-scan data per scanned sample is opened in the software, and had been gone through a consecutive process mentioned below[40].

1. Volume rendering → Volume edit
   To cut off the edges of the sample, top-bottom, and surrounding, to cope with the beam hardening effect.
2. Ortho Slice
   To check the edges. Can be done after each process.
3. Interactive threshold
   To threshold the sample (make sure all sample area is being threshold and take into account)
4. Label Analysis
   To measure the volume and surface area of the sample
   - Interpretation: 3D
   - Measures: Basic
     - Volume3d
     - Area3d
     - BaryCenterX
     - BaryCenterY
     - BaryCenterZ
     - Mean
     - Index
5. Median Filter
   - Iteration: 5
   - Interpretations: XY Planes
6. Interactive Top-Hat
   - Black Top-Hat
   - Neighborhood: 3D
   - Connectivity: 26
   - Kernel Size: 3
   - Preview: 2D
   - Input: Original Image
   - Threshold

Sample	Value	Sample	Value
36A	915 - 2746	26B	773 - 1421
39A	1133 - 7653	35B	3447 - 6895
47A	1007 - 2619	56	903 - 3434
48A	no fracture	58A	1494 - 8719
48B	542 - 1085	59B	1219 - 4635
55A	439 - 1428	79A	939 - 3487

[40] Modified from Thomas Ravenstein, 2014

29A 2738 - 7910

7. Despeckle
    - Interpretation XY Planes
    - Kernel Size X 5
    - Kernel Size Y 5
    - Threshold Factor 5
8. Remove Small Spots
    - Interpretation 3D
    - Size 2500
9. Closing
    - Interpretation 3D
    - Neighborhood 26
    - Size 20
10. Label Analysis
    - Interpretation 3D
    - Measures Thomas Group
        - Area3d
        - Volume3d
        - Lenght3d
        - Width3d
        - OrientationPhi
        - OrientationTheta
        - Index
11. Generate Surface

    This is done on the label
    - Smoothing type Unconstr. Smoothing
    - Smoothing Extent 5
    - Options Add Border
    - Border Adjust Coords
    - Min Edge Length 0
    - Smooth Material None
12. Surface View
    - Draw Style Shaded
    - Culling Mode No Culling
    - Colors Normal
13. Scale Bar
14. Local Axes
15. Bounding Box
16. Surface Thickness (This is done for each material)
17. Histogram (for each surface thickness)
    - Range 0 – (max 5)
    - Max Num Bins 256
18. Save label analysis* data, histogram data, and make screen shots of the surface view.

E.2. Images from CT-scanner

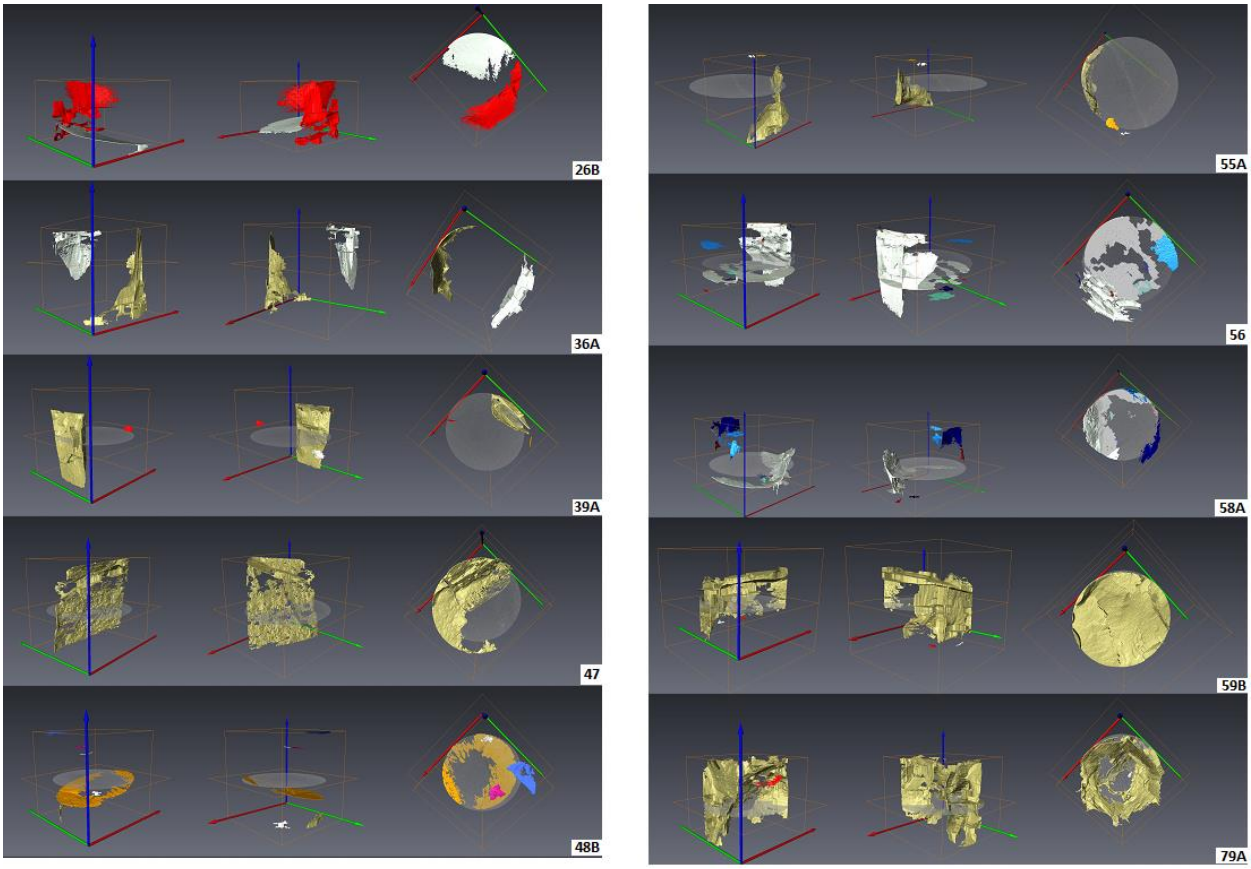

Figure 83 Image of all samples from CT scanner

E.3. Fracture Characterization Result

Table 19. Fracture Characteristic for each sample of WMF

Sample	Date	Voxel size	Core area	Core volume	Tot. frac length	Tot.frac area	Tot. frac vol	Tot. #fracs	Avg. frac area	Avg. frac vol	Avg. frac lenght	Avg. frac width	Avg. frac aperture	Frac Porosity
no.	[-]	Mm	mm2	mm3	mm	mm2	mm3	[-]	mm2	mm3	mm	mm	mm	[-]
26B	6_05_201	0.04x0.04x0.0400003	3586	16742	23	113	5	2	57	2	11.3	1.3	0.28	0.0003
29A	6_05_201	0.04x0.04x0.0400005	4709	26104	52	1324	156	4	331	39	12.9	4.2	0.21	0.0060
35B	7_05_201	0.04x0.04x0.0400004	3058	13132	79	2316	251	10	232	25	7.9	3.6	0.17	0.0191
36A	8_05_201	0.04x0.04x0.0400005	4462	23589	63	2335	409	2	1167	205	31.3	11.9	0.54	0.0173
39A	8_05_201	0.04x0.04x0.0400005	3872	18810	38	1174	223	3	391	74	12.8	3.8	0.43	0.0119
47	8_05_201	0.04x0.04x0.0400006	4952	27492	52	3142	389	2	1571	194	25.8	12.9	0.25	0.0141
48B	8_05_201	0.04x0.04x0.0400005	3594	16865	71	950	63	6	163	11	11.8	1.8	0.21	0.0037
55A	8_05_201	0.04x0.04x0.0400005	4174	15131	34	643	86	3	214	29	11.3	3.6	0.28	0.0057
56	9_05_201	0.04x0.04x0.0400006	5570	33573	95	3775	595	9	419	66	10.6	4.1	0.17	0.0180
58A	9_05_201	0.04x0.04x0.0400005	3061	13304	87	1182	141	10	118	14	8.7	2.8	0.18	0.0110
59B	9_05_201	0.04x0.04x0.0400005	3277	15168	44	3843	811	3	1281	270	14.5	7.8	0.39	0.0535
79A	9_05_201	0.04x0.04x0.0400005	3357	15824	49	4180	1008	3	1393	336	16.3	9.8	0.43	0.0637

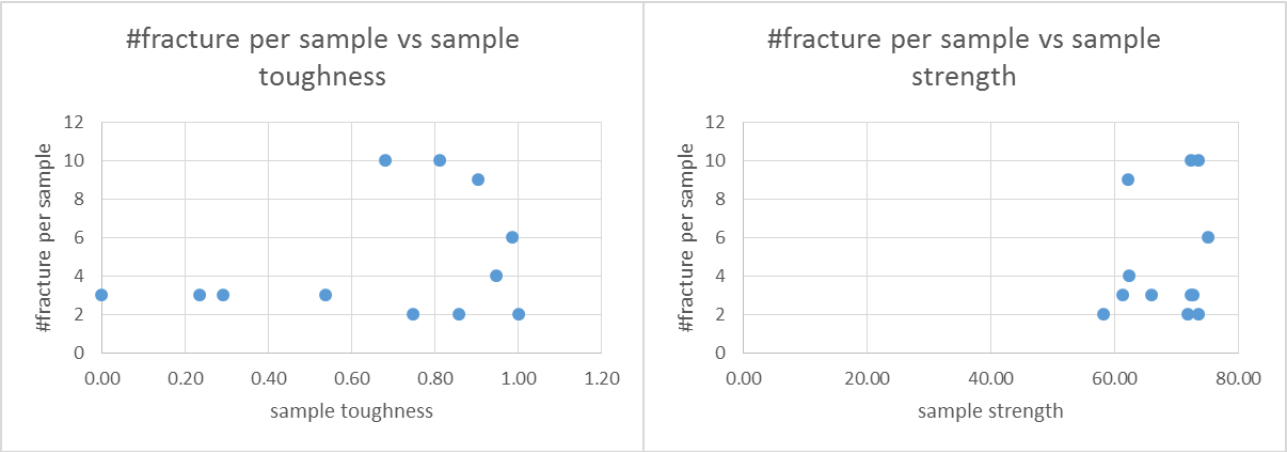

Figure 84. Plot of #fracture vs toughness per sample (left), and # fracture vs strength per sample (right)

Figure 84 shows that there is no correlation between amount of fracture and fracture strength, toughness.

Figure 85.Cross-plots showing the relationship between Avg. frac length vs –width, and – aperture (top), and the Avg. fracture width vs. – aperture

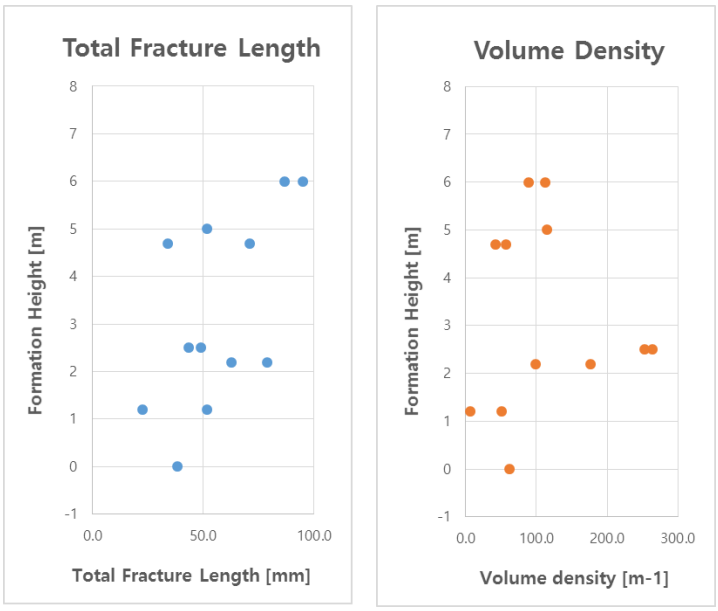

Figure 86. Total Fracture length vs height (left), and Volume density vs. height (right)